Minimum Power Requirements and Optimal Rotor Design for Conventional, Compound, and Coaxial Helicopters Using Higher Harmonic Control

by

Eli B. Giovanetti

Department of Mechanical Engineering and Materials Science
Duke University

Date: _____

Approved:

_____
Kenneth C. Hall, Supervisor

_____
Earl H. Dowell

_____
Laurens E. Howle

_____
Donald B. Bliss

_____
Thomas P. Witelski

Thesis submitted in partial fulfillment of the requirements for the degree of Master of Science in the Department of Mechanical Engineering and Materials Science in the Graduate School of Duke University
2013

Abstract

Minimum Power Requirements and Optimal Rotor Design for Conventional, Compound, and Coaxial Helicopters Using Higher Harmonic Control

by

Eli B. Giovanetti

Department of Mechanical Engineering and Materials Science
Duke University

Date: _____

Approved:

_____
Kenneth C. Hall, Supervisor

_____
Earl H. Dowell

_____
Laurens E. Howle

_____
Donald B. Bliss

_____
Thomas P. Witelski

An abstract of a dissertation submitted in partial fulfillment of the requirements for the degree of Master of Science in the Department of Mechanical Engineering and Materials Science
in the Graduate School of Duke University
2013

Abstract

This thesis presents a method for computing the optimal aerodynamic performance of conventional, compound, and coaxial rotor helicopters in trimmed forward flight with a limited set of design variables, including the blade's radial twist and chord distributions and conventional and higher harmonic blade pitch control. The optimal design problem, which is cast as a variational statement, minimizes the sum of the induced and viscous power required to develop a prescribed lift and/or thrust. The variational statement is discretized and solved efficiently using a vortex-lattice technique. We present two variants of the analysis. In the first, the sectional blade aerodynamics are modeled using a linear lift curve and a quadratic drag polar, and flow angles are assumed to be small. The result is a quadratic programming problem that yields a linear set of equations to solve for the unknown optimal design variables. In the second approach, the problem is cast as a constrained nonlinear optimization problem, which is solved using Newton iteration. This approach, which accounts for realistic lift and drag coefficients including the effects of stall and the attendant increase in drag at high angles of attack, is capable of optimizing the blade planform in addition to the radial twist distribution and conventional and higher harmonic blade pitch control. We show that for conventional rotors, coaxial counter-rotating rotors, and a wing-rotor compound, using radially varying twist and chord distributions and higher harmonic blade pitch control can produce significant reductions in required power, especially at high advance ratios.

Contents

List of Tables

List of Figures

List of Abbreviations and Symbols

Symbols

A	Rotor disk area, πR^2
$\mathbf{A}$	Matrix relating design variables $\boldsymbol{\Theta}$ to circulation $\boldsymbol{\Gamma}$
$\mathbf{A}_{\text{LL}}$	Matrix relating pitch angle at each panel $\boldsymbol{\theta}$ to the resulting circulation distribution $\boldsymbol{\Gamma}$ through linearized lifting line theory
A_n	nth Fourier coefficient of blade pitch
B_n	nth Fourier coefficient of blade pitch
B	Number of blades
$\mathbf{B}$	Matrix relating force $\mathbf{F}$ to circulation $\boldsymbol{\Gamma}$
$\mathbf{b}_i$	ith column of B
C_L	Lift coefficient, $L/\rho A\Omega^2 R^2$
C_P	Power coefficient, $P/\rho A\Omega^3 R^3$
c_d	Airfoil sectional drag coefficient
c	Blade chord
$\mathbf{c}$	Vector containing blade chord at each panel in the grid
$\mathbf{C}$	Chord inequality constraint vector
$\mathbf{c}_{\text{span}}$	Vector containing the blade chord along each lifting surface
c_{d0}	Coefficient in airfoil drag approximation
c_{d2}	Coefficient in airfoil drag approximation
c_ℓ	Airfoil sectional lift coefficient

$c_{\ell 0}$	Coefficient in airfoil drag approximation
$c_{\ell \alpha}$	Lift curve slope
$\bar{c}$	Constant used in step size control algorithm
γ^m	Constant used in step size control algorithm
$\mathbf{d}_k$	Vector containing the search direction at the k-th iteration
D	Damping factor used in iterative nonlinear lifting line analysis
$\mathbf{D}$	Matrix relating moment $\mathbf{M}$ to circulation $\mathbf{\Gamma}$
$\mathbf{d}_i$	ith column of D
E	Kinetic energy per period in wake
$\mathbf{E}$	Vector that gives the solidity σ when dotted with the vector of design variables, $\mathbf{\Theta}$
$\mathbf{E}_{\text{full}}$	Vector that gives the solidity σ when dotted with the chord distribution along each lifting surface, $\mathbf{c}_{span}$
$\mathbf{F}$	Time-averaged aerodynamic force vector
f	Number of design variables affecting pitch angle
g	Number of design variables affecting the chord distribution
$\mathbf{g}_k$	Vector containing the gradient of the cost function at the k-th iteration
h	Total number of design variables
$\mathbf{H}$	Hessian matrix
L	Vehicle lift
$\mathbf{L}$	Near field to far field mapping matrix
ℓ	Airfoil sectional lift
$\mathbf{K}$	Quadratic power matrix
$\mathbf{K}_v$	Linearized viscous power vector
K_{ij}	i,j-th element of $\mathbf{K}$
M	Number of panels used in vortex lattice grid

$\mathbf{M}$	Time-averaged aerodynamic moment vector, or local Mach number
N	Number of harmonics in higher harmonic control
n	Fourier coefficient index
$\mathbf{n}$	Unit vector normal to wake surface
P	Rotor power loss
$\mathbf{P}_c$	Vector relating a change in the chord design variables $\boldsymbol{\Theta}_c$ to a change in the viscous power loss P_v
$\mathbf{P}_\theta$	Vector relating a change in the pitch angle design variables $\boldsymbol{\Theta}_\theta$ to a change in the viscous power loss P_v
$\mathbf{P}_{\boldsymbol{\Theta}}$	Vector relating a change in the entire vector of design variables $\boldsymbol{\Theta}$ to a change in the viscous power loss P_v
$\mathbf{Q}$	Vector associated with linear portion of viscous power loss
R	Rotor radius
$\mathbf{R}$	Vector function describing the relationship between the circulation $\boldsymbol{\Gamma}$ and the design variables $\boldsymbol{\Theta}$
$\mathbf{R}_\Gamma$	Jacobian of $\mathbf{R}$ with respect to $\boldsymbol{\Gamma}$
$\mathbf{R}_\Theta$	Jacobian of $\mathbf{R}$ with respect to $\boldsymbol{\Theta}$
$\mathbf{R}_{\theta\text{Full}}$	Concatenation of $\mathbf{R}_\theta$ and $\mathbf{R}_c$
$\mathbf{R}_\theta$	Jacobian of $\mathbf{R}$ with respect to $\boldsymbol{\Theta}_\theta$
$\mathbf{R}_\text{c}$	Jacobian of $\mathbf{R}$ with respect to $\boldsymbol{\Theta}_c$
$\mathbf{r}$	Moment arm from vehicle center to lifting surface
$\mathbf{S}_\text{total}$	Matrix relating design variables $\boldsymbol{\Theta}$ to the pitch angle $\boldsymbol{\theta}$ and chord $\mathbf{c}$ at each panel in the grid
$\mathbf{S}_\theta$	Matrix relating design variables affecting pitch angle, $\boldsymbol{\Theta}_\theta$, to the pitch angle at each panel in the grid, $\boldsymbol{\theta}$
$\mathbf{S}_c$	Matrix relating design variables affecting chord, $\boldsymbol{\Theta}_c$, to the chord at each panel in the grid, $\mathbf{c}$
$\mathbf{S}_\text{cRadial}$	Matrix relating design variables affecting chord, $\boldsymbol{\Theta}_c$, to the chord along each lifting surface, $\mathbf{c}_{span}$

T	Temporal period of the wake
u	Relative fluid velocity perpendicular to span
V	Vehicle forward speed
$\mathbf{v}_{ij}$	Induced velocity at the ith lifting line segment due to the jth vortex ring element
$\mathcal{W}$	Wake sheet surface
W	Positive weighting value
$\mathbf{W}$	Influence coefficient matrix relating circulation $\boldsymbol{\Gamma}$ to induced wash $\mathbf{w}$
$\mathbf{w}$	Induced velocity in far wake
w_{ij}	Induced velocity at vortex i due to vortex j
$\mathbf{W}_\alpha$	Matrix relating circulation $\boldsymbol{\Gamma}$ to induced angle of attack α_{ind}
α_{shaft}	Rotor disk angle of attack
$\boldsymbol{\alpha}_{\text{ind}}$	Vector containing the induced angle of attack at each panel
$\boldsymbol{\alpha}_{\text{geo}}$	Vector containing the angle of attack at each panel due to the geometry of wake
$\boldsymbol{\alpha}_{\text{eff}}$	Vector containing the effective angle of attack at each panel
Γ	Circulation
$\boldsymbol{\Gamma}$	Vector circulation strengths at panels
$\boldsymbol{\Gamma}_0$	Vector of circulation strengths due to zero control inputs
ΔA_i	Area of ith vortex panel
δ_{ij}	Kronecker delta
δ	Variational operator
θ_0	Fixed blade twist distribution
θ	Vector containing the pitch angle due to the design variables at each panel
$\boldsymbol{\Theta}$	Vector of design variables

$\boldsymbol{\Theta}_\theta$	Vector of design variables affecting pitch angle
$\boldsymbol{\Theta}_c$	Vector of design variables affecting chord
κ	Lagrange multiplier for lift inequality constraint
$\boldsymbol{\lambda}$	Equality constraint Lagrange multiplier
$\boldsymbol{\lambda}_F$	Lagrange multiplier for force constraint
$\boldsymbol{\lambda}_M$	Lagrange multiplier for moment constraint
λ_σ	Lagrange multiplier for solidity constraint
$\boldsymbol{\lambda}_c$	Lagrange multiplier for chord constraint
μ	Advance ratio, $V/\Omega R$
$\boldsymbol{\xi}$	Kelvin linear impulse
Π	Power Lagrangian
ρ	Fluid density
σ	Rotor solidity, $Bc/\pi R$
σ_{TW}	Thrust weighted rotor solidity
σ_{TWM}	Modified thrust weighted rotor solidity
ϕ	Velocity potential function
ψ	Azimuthal angle
Ω	Rotor rotational speed
∇	Gradient operator
∇^2	Laplace operator

Subscripts

max	Maximum value
min	Minimum value
R	Prescribed value
v	Viscous

Abbreviations

QP	Quadratic programming
NLP	Nonlinear programming

Acknowledgements

This work was funded in part by a contract from Sikorsky Aircraft Corporation, whose support is gratefully acknowledged. The author would also like to acknowledge the Department of Defense and the American Society of Engineering Education for their financial support through the National Defense Science and Engineering Graduate (NDSEG) Fellowship.

1

Introduction

One of the technical challenges to fast forward flight in helicopters is the rapid rise in induced and viscous power with advance ratio, μ. While induced power for a fixed wing aircraft decreases monotonically with increasing speed, the induced power of a conventional helicopter rotor first decreases, then increases dramatically [14, 27]. This increase is due in part to the asymmetric wake structure of a conventional rotor, shown in Figure 1.1. The large gaps in the wake on the retreating side of the rotor necessitate regions of high circulation to maintain roll trim, resulting in a sub-optimal lift distribution and high induced power loss [14].

It has long been recognized that tailoring the lift distribution of a rotor can improve performance [40, 33, 4, 38]. Methods of tailoring the lift distribution include designing the blade twist and chord distributions and selecting the airfoils to be used along the span of a blade. In addition to these conventional rotor design features, the lift distribution can be tailored through the use of higher harmonic control, defined as the use of harmonic pitch inputs to the blade in addition to the traditional zero and one per rev control typically achieved with a swashplate. In practice, higher harmonic control can be implemented in a variety of ways, including individual blade control

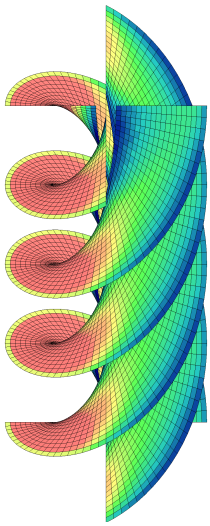

FIGURE 1.1: Wake of a conventional rotor in forward flight at an advance ratio of $\mu = 0.5$. Coloring indicates the circulation distribution for the minimum power trimmed solution [14].

(IBC), active pitch links, or trailing edge flaps (TEF) that can be actuated multiple times per revolution.

Historically, higher harmonic control has been studied for its applications to vibration or noise reduction. However, some studies have also investigated its use in rotor performance improvement on conventional (i.e., single) rotors. Both experimental and numerical analysis have shown that higher harmonic control offers some improvement at high advance ratios (typically between $\mu = 0.4 - 0.5$ for conventional rotors) in reducing both induced and profile power losses. Stewart [40], Payne [33], and Arcidiacono [4] considered the use of higher harmonic control to prevent the onset of blade stall on the retreating side and compressibility losses on the advancing side of a conventional rotor, thereby increasing the maximum practical advance ratio of the rotor. Moffitt and colleagues [25] [26] used a variational approach to optimize the twist of a conventional rotor in forward flight, using lifting line theory and small angle assumptions to model the rotor aerodynamics. They found that allowing for continuously varying azimuthal blade twist (effectively an infinite level of per rev

harmonic control) could result in significant reductions in both induced and profile power, reducing total power by up to 15% at an advance ratio of approximately $\mu = 0.35$. Hall *et al.* [17] used a variational approach to determine the minimum induced loss lift distribution, and determined that at an advance ratio of $\mu = 0.25$, typical rotors may have 10-15% more induced losses than the minimum induced loss solution, suggesting that there is room for performance improvement through higher harmonic control and improved rotor design. Cheng *et al.* [10] evaluated the use of 2/rev harmonic control to improve the performance of a four-bladed articulated rotor through decreases in profile losses. The authors found that a properly phased 2/rev input can decrease required power by about 16% at an advance ratio of $\mu = 0.32$, primarily through perturbing the angle of attack to change the distribution of the profile drag coefficient over the rotor disk. In a similar approach to the Reference [17] work, Rand *et al.* [36] used an iterative approach to find the optimal circulation distribution of a single rotor using a free-wake geometry, and found that reductions of no more than 10% of the induced power can be achieved under any passive or active blade rotor design for advance ratios less than $\mu = 0.25$.

Beginning in 2004, Ormiston [27, 28] developed a simplified rotor model to explore the fundamental behavior of rotor induced power at moderate to high advance ratios. Ormiston also studied the effect of higher harmonic control on rotor performance, and concluded that higher harmonic control offers promise for reducing induced power, especially at high advance ratios. Ormiston also found that using the correct level of blade twist reduces induced power, although the optimal twist distribution varies with advance ratio. Wachspress *et al.* [41] used a free-vortex wake model to analyze a conventional rotor with constant chord, linearly twisted blades and higher harmonic control. Both 2/rev and 3/rev control inputs with varying phases were analyzed to determine the phase shifts that would yield power decreases. Among the authors' findings were that a 3/rev pitch input can reduce induced power by 4% at an advance

ratio of $\mu = 0.2$. The authors also suggest that a more formal optimization routine that includes harmonic cyclic inputs and radial basis functions as design variables could offer improved insight compared to performing parametric studies that vary one variable at a time.

Experimental results have also demonstrated the promise of higher harmonic control in performance improvement. Shaw *et al.* [38] conducted wind-tunnel tests that demonstrated up to 6% reduction in power required on a Boeing CH-47D rotor at 135 kt using 2/rev swashplate control. Jacklin *et al.* [19, 20] performed wind tunnel tests on a full-scale BO-105 helicopter rotor using individual blade control, and found that a 2/rev input could achieve up to a 7% power reduction at high advance ratios ($\mu = 0.4 - 0.45$). However, the 2/rev input resulted in an increase in power at lower advance ratios.

Another active area of research aimed at improving high speed efficiency in helicopters is in the design of coaxial and compound helicopters. Coaxial and compound helicopters have long demonstrated promise in reducing power requirements in forward flight relative to a conventional rotor. A compound helicopter combines the hover capabilities of a helicopter with high speed flight capability through the use of a separate source of propulsive force in addition to the rotor. Frequently, a compound helicopter also uses a wing to provide additional lift at high flight speeds. Examples of compound helicopters include the Cheyenne helicopter (Figure 1.2), and, more recently, the Eurocopter X3 (Figure 1.3), which exceeded speeds of 255 knots in level, stabilized flight [32] and currently holds the world record for the fastest compound helicopter. A coaxial rotor is defined as a pair of counter-rotating rotors that spin about a common shaft axis. In the 1970s, the Sikorsky X-59 made use of a coaxial, rigid rotor in a system referred to as the Advancing Blade Concept (ABC). The ABC offloads the retreating blade at high speeds, achieving roll trim by balancing the moments transmitted to the hub by the opposing advancing side blades. This

FIGURE 1.2: Cheyenne helicopter, which uses a lifting wing to offload the rotor in forward flight [24].

FIGURE 1.3: Eurocopter X3 compound helicopter, which uses a lifting wing with two propellers for auxilliary propulsion [34].

arrangement results in each rotor carrying a lateral lift offset (LOS), where the majority of lift is generated on the advancing side of each rotor, resulting in a more efficient lift distribution. Although the X-59 never went into production, Sikorsky recently made use of the ABC with modern technologies in the design of the X2 Technology Demonstrator (X2 TD), shown in Figure 1.4. The X2 TD used a coaxial rotor system in combination with a pusher propeller to achieve speeds of 250 knots in level flight [11].

FIGURE 1.4: Sikorsky X2 technology demonstrator, which uses a coaxial rotor and a pusher propeller [35].

In Reference [5], Bagai describes the aerodynamic design of the X2 TD main rotor blades, which was driven by high speed flight requirements. The blades make use of modern airfoils, a non-uniform planform, and a nonlinear twist distribution to reduce profile losses of the rotor. Induced power losses were not considered in the analysis, although the author notes that "It is to be expected that induced losses make up a significant part of the power consumed by the rotor, and careful consideration of these losses need yet to be made." Also of interest, the author notes that 2/rev harmonic control may prove beneficial in improving the aerodynamic efficiency of the rotor. However, with the exception of the Reference [16] paper that serves as the foundation for this work, to date no studies have been conducted to evaluate the use of higher harmonic control in compound and coaxial configurations for rotor performance improvement.

In addition to the Reference [5] paper, a fair amount of recent research seeks to understand and improve the performance of compound and coaxial rotors. Johnson [21] used the comprehensive analysis code CAMRAD II to explore the calculated performance capability of coaxial rotors using lift offset (LOS) rigid rotors. Johnson performed parametric studies to determine the blade twist, chord, and sweep that yield the optimal balance of hover and cruise performance. The coaxial configuration analyzed also includes a small lifting wing and two propellers for additional thrust in forward flight. Johnson found that a lift offset of about 0.25 is effective in reducing the rotor induced power and profile power, yielding a rotor effective lift-to-drag ratio of about 10 at high speeds. Additionally, by comparing free wake and prescribed wake results, Johnson concluded that a free wake geometry is not required in the aerodynamic modeling of high advance ratios. References [22] and [37] continue this work, using CAMRAD II to determine the optimal configuration and sizing for specific mission requirements. Ormiston [31] used formal optimization techniques with a compact analytical model for induced power to determine the optimal rotor collective

pitch, angle of attack, and linear blade twist for several compound configurations, and concluded that a full compound using both a wing and auxilliary propulsion provides the best aerodynamic efficiency. Also of interest, Ormiston concluded that induced power significantly reduces the aerodynamic efficiency of compound rotorcraft, and is an important factor in distinguishing between high and low performance configurations.

Hall and Hall [14], building upon their Reference [17] work on the minimum induced loss lift distribution of helicopter rotors in forward flight, used a variational approach to compute the theoretical optimal aerodynamic performance of conventional and compound helicopters in trimmed flight. They found that compound and coaxial configurations can substantially reduce power loss by producing a more efficient wake structure and by reducing the induced power associated with roll trim. The optimal circulation distribution minimizes the sum of the induced and viscous power required to develop a prescribed lift and/or thrust, subject to constraints that the helicopter be trimmed in pitch and roll. The resulting analysis – which is the viscous helicopter analog of Goldstein's inviscid propeller theory [13] – gives rigorous upper bounds on the performance of conventional and compound helicopters and may be used to predict the rotor/wing loadings that produce optimal performance. This analysis does not consider the specific rotor design required to achieve the optimal circulation distribution; rather, it assumes a "rubber rotor" that can be articulated with unlimited degrees of freedom to achieve the optimal circulation distribution.

The Reference [14] results raise some very interesting questions. If one is limited to a finite number of design variables – for example, blade planform, blade twist, and collective and cyclic blade pitch control – then what is the optimal performance (minimum power) that can be achieved? Additionally, what design variables are required to achieve the optimum, and what performance improvements can be achieved using higher harmonic blade control in conventional, compound, and coaxial rotors?

This thesis presents two methods for determining the optimal rotor design for conventional and compound helicopter configurations using higher harmonic blade root control. The optimal rotor design minimizes the sum of the induced and viscous power losses while achieving a prescribed lift and maintaining roll and pitch trim. Results are presented for the analysis of a conventional rotor, coaxial rotor, and wing-rotor compound, shedding light on the minimum power of various rotor designs and the potential benefits of higher harmonic control and optimized blade design. The work presented here is an extension of the Reference [16] work by Hall and Giovanetti, which investigated the use of higher harmonic control in conventional and coaxial configurations.

Chapter 2 summarizes the optimal circulation problem (i.e., the rubber rotor analysis), which is cast as a variational statement that minimizes the sum of induced and viscous power required to develop a prescribed lift and/or thrust. The variational statement is discretized and solved using a vortex-lattice technique.

Chapter 3 describes two approaches to solving the optimal rotor design problem. The first method, referred to as the Quadratic Programming or QP approach, models the sectional blade aerodynamics using a linear lift curve, a quadratic drag polar, and assumes small induced angles of attack. Furthermore, the chord distribution is fixed, and is not included in the set of design variables. The result is a quadratic programming problem that yields a set of linear equations to solve for the unknown optimal design variables. The QP method provides an extremely efficient approach to calculating optimal rotor performance and design. The second method, referred to as the Nonlinear Programming or NLP approach, solves the fully nonlinear variational problem, which accounts for nonlinear lift curves, non-quadratic drag polars, large induced angles of attack, and includes blade chord as a design variable. An approach to solving the nonlinear problem via Newton iteration is described. Additionally, a second approach to solving the nonlinear problem using Mathematical Programming

via Augmented Lagrangians is described in Appendix A. The NLP method provides a more accurate approach to calculating optimal rotor performance and design, and has the added capability of optimizing the chord distribution. Chapter 3 also includes a comparison of results to Allen's computational fluid dynamics analysis [1] of the Caradonna-Tung rotor [9], demonstrating that the simplified analysis developed here agrees well with high fidelity CFD calculations.

Chapter 4 describes the optimal rotor design and performance of a conventional rotor. Results show that 2/rev and 3/rev harmonic control provide large power reductions at very high advance ratios ($\mu > 0.5$), while offering more modest power reductions at advance ratios below this. Additionally, results show that the use of an optimized blade twist and chord distribution provides large power reductions at all advance ratios; for example, at $\mu = 0.4$, use of an optimized twist distribution and planform yield a 37% reduction in total power compared to a uniform chord, zero twist blade. Also of interest, the optimal planform at $\mu = 0.4$, which is representative of high speed flight in modern helicopters, includes a highly non-uniform planform with higher solidity than the baseline rectangular blade. This blade design serves to dramatically reduce induced power and increase efficiency.

Chapter 5 describes results for a coaxial rotor design intended to approximate the X2 Technology Demonstrator parameters. At the design intent advance ratio of $\mu = 0.85$, use of 3/rev harmonic control provides a 16% reduction in total power over conventional 1/rev control. Also of interest, the optimal lift offset at this high speed is close to 0.5. When making use of a more restrictive lift offset, higher harmonic control provides significantly larger relative benefits. For example, 2/rev harmonic control yields a 47% reduction in power versus 1/rev at the design advance ratio with lift offset constrained to 0.3, the maximum value used on the X2 TD rotor. Analysis of a single point design shows that higher harmonic control is also effective in improving the performance of a given blade at off-design points, an encouraging result given the

practical limitation to use a fixed blade geometry across all flight conditions. Finally, results show that induced power losses play a large role in optimum rotor design and performance.

Chapter 6 gives results for a wing-rotor compound configuration approximating the Cheyenne helicopter. These results show that use of an optimal wing and rotor twist distribution and planform yields a 40% reduction in total power at $\mu = 0.8$ compared to an untwisted blade and wing with uniform chord distributions. Higher harmonic control offers more modest benefits when used in conjunction with the optimized planforms; however if the optimal high speed wing and rotor design are not used (perhaps due to hover or low speed requirements), higher harmonic control is effective at reducing power. Also of interest, use of an off-centered wing results in decreased power requirements relative to a centered wing of the same span. For example, for a wing with span equal to one rotor radius, placing the wing entirely on the retreating side of the rotor results in a 20% reduction in total power compared to a centered wing. This result suggests that an asymmetric wing could be used in forward flight to significantly improve vehicle performance.

Finally, Chapter 7 gives concluding remarks and includes a brief discussion of future work.

2

Aerodynamic Modeling of a Rotor

In this section, we briefly describe the aerodynamic models we use to calculate the forces and moments acting on helicopter rotors, and the resulting induced and viscous power losses. Additionally, we present a summarized version of the Reference [14] far field analysis that determines the optimal circulation for minimum power requirements, i.e. the rubber rotor solution. The modeling here assumes high aspect ratio rotor blades, so lifting line theory may be used to calculate induced washes. We assume light loading and/or high advance ratios, so a prescribed wake is appropriate. Finally, we assume that for the purpose of computing viscous forces (but not inviscid forces), the flow is quasi-steady. Thus, the sectional lift and drag can be described using steady two-dimensional lift and drag curves found from experiment or using a computational fluid dynamic analysis.

2.1 Forces and Moments

Following Hall and Hall [14], we calculate inviscid forces and moments (and also induced power) using a far-field approach. The forces and moments acting on the rotor(s) or rotor/wing system are a result of apparent linear and angular momentum

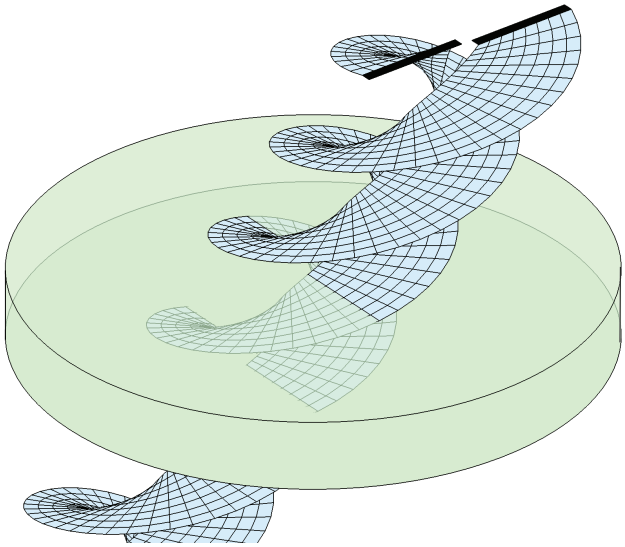

FIGURE 2.1: Schematic of prescribed wake showing one period of the far wake bounded by the Trefftz volume [14].

(i.e., Kelvin linear and angular impulses) deposited in the wake of the rotor. The Trefftz volume bounds one period of the flow field in the far wake, bounded between two infinite parallel planes roughly transverse to the flight direction as shown in Figure 2.1.

The far field flow is assumed to be inviscid, incompressible, and irrotational, except for the trailing and shed vorticity in the wake. Note that the assumption of incompressible flow requires only that the induced velocities in the wake be small compared to the speed of sound, an assumption consistent with the light loading model. (The flow *will* in general be compressible in the near field of the rotor.) Thus, the three-dimensional flow in the far wake is governed by Laplace's equation expressed in the fluid frame of reference,

$$\nabla^2 \phi = 0 \quad \text{where} \quad \mathbf{w} = \nabla \phi \tag{2.1}$$

where ϕ is the velocity potential and $\mathbf{w}$ is the induced wash.

The net aerodynamic forces acting on a rotor (or any system of rotors and wings) is equal and opposite to the rate at which the Kelvin linear impulse of the fluid

increases. The Kelvin impulse for one period of the wake can be expressed as an area integral, i.e.,

$$\boldsymbol{\xi} = -\rho \iint_{\mathcal{W}} \Gamma \mathbf{n} \, dA \tag{2.2}$$

where the integral is taken over one side of the wake denoted by $\mathcal{W}$, and $\mathbf{n}$ is the unit normal to the wake. Thus, the time-averaged force on the rotor is equal to

$$\mathbf{F} = -\frac{\boldsymbol{\xi}}{T} = \frac{\rho}{T} \iint_{\mathcal{W}} \Gamma \mathbf{n} \, dA \tag{2.3}$$

where T is the temporal period of the wake, usually equal to $2\pi/\Omega B$ because only one B-th of a turn of the wake is required to achieve periodicity.

Likewise, the time-averaged moment acting on the system is equal to

$$\mathbf{M} = \frac{\rho}{T} \iint_{\mathcal{W}} \Gamma \, \mathbf{r} \times \mathbf{n} \, dA \tag{2.4}$$

where $\mathbf{r}$ is the moment arm extending from the center of gravity of the aircraft to the element of wake area at the time the wake is generated.

2.2 Induced Power

The induced power losses due to lift and thrust of a conventional helicopter rotor, or rotor/wing/propeller system for a compound helicopter, arise from the deposition of kinetic energy into the wake. The kinetic energy contained in the Trefftz volume is given by

$$E = \iiint_{\mathcal{V}} \frac{1}{2} \rho \left| \mathbf{w} \right|^2 \, dV = \frac{\rho}{2} \iiint_{\mathcal{V}} \left| \nabla \phi \right|^2 \, dV \tag{2.5}$$

Application of the second form of Green's theorem, and making use of the periodicity of the wake in the far-field, the asymptotic decay rate of the wash in the direction transverse to the direction of flight, and the fact that the potential satisfies Laplace's

equation, one can show that the energy per period of the wake can be expressed as

$$E = -\frac{\rho}{2} \iint_{\mathcal{W}} \Gamma \mathbf{w} \cdot \mathbf{n} \, dA \tag{2.6}$$

Hence, the time-averaged induced power P_{i}, equal to the rate of kinetic energy production, is given by

$$P_{\mathrm{i}} = -\frac{\rho}{2T} \iint_{\mathcal{W}} \Gamma \mathbf{w} \cdot \mathbf{n} \, dA \tag{2.7}$$

Note that the induced wash $\mathbf{w}$ is linearly related to the circulation Γ through the Biot-Savart law. Thus, the induced power is quadratic in the circulation. Furthermore, the forces and moments generated by the rotor system are proportional to Γ, so the induced power will be quadratic in the forces and moments. Also of note, the induced power may take the form of induced rotor torque (shaft power) or induced drag. The current approach makes no distinction between these losses. Interestingly, the induced drag is sometimes not a drag at all, but rather an induced *thrust*.

2.3 Profile Power

To determine the profile power losses, we make the simplifying assumption that the aerodynamic surfaces have large aspect ratios, allowing us to model the sectional aerodynamic forces using quasi-steady sectional lift and drag coefficients as a function of local angle of attack.

As an example, Figure 2.2 shows the lift and drag computed for a NACA 0012 airfoil operating at a Reynolds number of 10,000,000 for the full range of angles of attack from -180 to $+180$ degrees [39]. Note that for small angles of attack ($-14^\circ < \alpha < +14^\circ$), the lift curve slope is linear and the drag is relatively small. For larger angles of attack, however, the airfoil is stalled, and the lift and drag can be quite large, and they behave in a fundamentally nonlinear fashion.

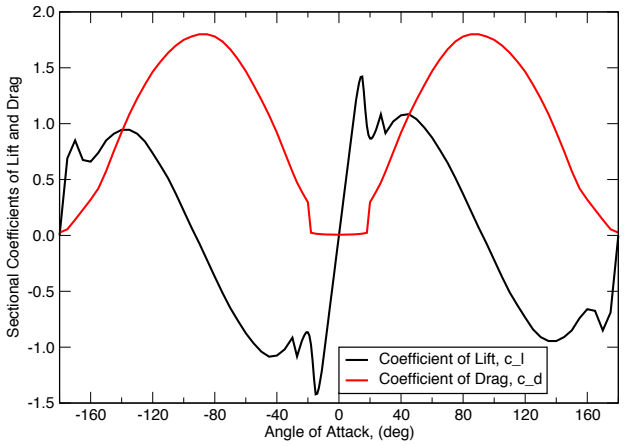

FIGURE 2.2: Computed sectional coefficients of lift and drag for a NACA 0012 airfoil operating at Re = 10,000,000 [39].

In general, the time averaged profile power P_{v} may be expressed as the work per cycle divided by the period, so that

$$P_{\mathrm{v}} = \frac{1}{T} \iint_{\mathcal{W}} \frac{1}{2} \rho u^2 c c_d \, dA \tag{2.8}$$

where u is the relative velocity of a given airfoil section normal to the span of the rotor.

We use one of two different drag models. For fully nonlinear calculations, we spline fit the complete lift and drag curves as a function of angle of attack and make use of Equation (2.8). However, in the quadratic programming approach to be discussed in the following section, we make the assumption of small angles of attack. For these pre-stall small angle of attack cases, it is useful to represent the drag in the form of a drag polar, $c_d = c_d(c_\ell)$. Figure 2.3 shows the computed drag polar for the NACA 0012 airfoil for small angles of attack. Also shown is a quadratic curve fit. We see that in this unstalled region, the coefficient of drag is very nearly quadratic in the coefficient of lift, so we may write

$$c_d \approx c_{d0} + c_{d2} \left(c_\ell - c_{\ell 0} \right)^2 \tag{2.9}$$

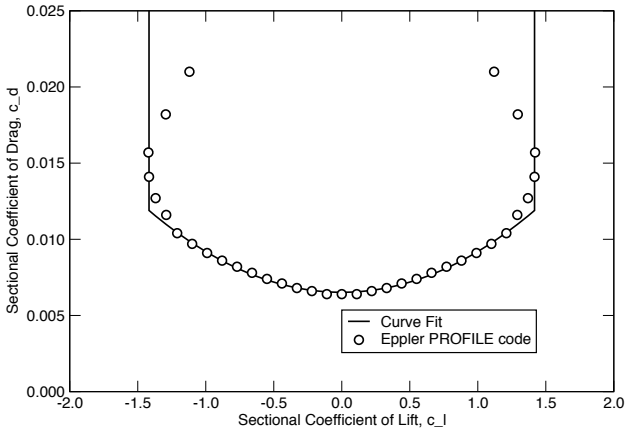

FIGURE 2.3: Computed sectional drag polar for a NACA 0012 airfoil operating at Re = 10,000,000 [39]. Also shown is quadratic curve fit to data in unstalled region.

for $c_{\ell\text{min}} \leq c_\ell \leq c_{\ell\text{max}}$. The curve fit shown uses the values $c_{d0} = 0.00651$, $c_{d2} = 0.00268$, $c_{\ell 0} = 0.0$, $c_{\ell\text{min}} = -1.421$, and $c_{\ell\text{max}} = +1.421$.

For the case of the quadratic drag polar, Equation (2.8) may be written as a quadratic function of the circulation. The coefficient of lift may be expressed in terms of the circulation as

$$c_\ell = \frac{\ell}{\frac{1}{2}\rho u^2 c} = \frac{2\Gamma}{uc} \tag{2.10}$$

Making use of the quadratic drag polar approximation, the viscous power is given by

$$P_{\text{v}} = \frac{\rho}{2T} \iint_{\mathcal{W}} \left\{ \left(\frac{4c_{d2}}{c} \right) (\Gamma - \Gamma_0)^2 + \left(u^2 c c_{d0} \right) \right\} \, dA \tag{2.11}$$

where Γ_0 is the circulation corresponding to a coefficient of lift equal to $c_{\ell 0}$. Note that in this form, the viscous power is quadratic in the circulation.

2.4 Optimal Rotor Performance

We first seek to find the unsteady circulation distribution that produces an optimal solution without regard to the control inputs required to achieve this circulation distribution. For a more detailed documentation of this approach, see References [14, 17, 42].

We define the optimum circulation distribution to be that which minimizes the sum of the induced and profile powers subject to lift and trim constraints. Making use of the calculus of variations, we adjoin the lift and moment trim constraints to the total power using Lagrange multipliers $\boldsymbol{\lambda}_M$ and $\boldsymbol{\lambda}_F$, respectively. The result is the Lagrangian power Π, that is,

$$\Pi = P_{\mathrm{i}} + P_{\mathrm{v}} + \boldsymbol{\lambda}_F \cdot (\mathbf{F} - \mathbf{F}_R) + \boldsymbol{\lambda}_M \cdot (\mathbf{M} - \mathbf{M}_R) \tag{2.12}$$

where $\mathbf{F}_R$ and $\mathbf{M}_R$ are the prescribed time-averaged aerodynamic force and moment vectors, respectively. Taking the variation of Equation (2.12) and setting the result to zero, and with the help of some vector identities, yields the generalized Betz criterion for the case of the fully nonlinear lift/drag curves, that is

$$\mathbf{w} \cdot \mathbf{n} = (\boldsymbol{\lambda}_F + \boldsymbol{\lambda}_M \times \mathbf{r}) \cdot \mathbf{n} + u \frac{c_{d_\alpha}}{c_{\ell_\alpha}} \tag{2.13}$$

Alternatively, for the case where viscous effects are modeled using the quadratic drag polar, we require that the circulation not be so large as to result in airfoil stall. Thus, we adjoin to Π this additional inequality constraint using the Lagrange multiplier κ, with the result

$$\Pi = P_{\mathrm{i}} + P_{\mathrm{v}} + \boldsymbol{\lambda}_F \cdot (\mathbf{F} - \mathbf{F}_R) + \boldsymbol{\lambda}_M \cdot (\mathbf{M} - \mathbf{M}_R) + \frac{\rho}{T} \iint_{\mathcal{W}} \kappa \left(\Gamma - \Gamma_{\max}\right) \, \mathrm{d}A \tag{2.14}$$

Note κ is nonzero only on regions of the wake where the circulation is large enough that the stall constraint is in effect. Again, taking the variation and setting the result to zero gives

$$\mathbf{w} \cdot \mathbf{n} = (\boldsymbol{\lambda}_F + \boldsymbol{\lambda}_M \times \mathbf{r}) \cdot \mathbf{n} + \frac{4 c_{d_2}}{c} \left(\Gamma - \Gamma_0\right) + \kappa \tag{2.15}$$

Equations (2.13) and (2.15) give the resultant normal wash on the far wake for an optimally loaded rotor for the fully nonlinear and quadratic drag polars, respectively. Each of these two equations may be thought of as a generalized Betz criterion

for optimality [14, 7]. For the fully nonlinear drag curve case, the term $u\, c_{d_\alpha}/c_{\ell_\alpha}$ is small, except when the lift curve slope goes to zero, that is, as the blade approaches stall. For the quadratic drag polar case, the term involving c_{d_2} has little effect on the optimum circulation, and in fact c_{d_0} does not appear at all. If the stall inequality constraint is not active at some radial and azimuthal location, then $\kappa = 0$ everywhere, and the last term has no effect. The effect of the terms $u\, c_{d_\alpha}/c_{\ell_\alpha}$ in Equation (2.13) and κ in Equation (2.15) is to reduce the optimal downwash in regions approaching stall. Furthermore, for both cases, while profile power certainly contributes significantly to the total power, if the rotor is not constrained by stall, then the optimum circulation distribution is (very nearly) found by minimizing induced losses – at least for a prescribed planform.

2.5 Vortex Lattice Model

In the previous sections, we outlined an analytical description of the minimum power solution for a rotor in forward flight. As a practical matter, to solve for the optimum, we must discretize the relevant equations. To calculate the optimal aerodynamic power and corresponding circulation distribution, we represent the wake trace using a lattice of vortex rings, which can model both trailing and shed vorticity in the wake. One period of the wake trace (the reference period) is divided into M quadrilateral elements (see Figure 2.4). The ith element is a quadrilateral vortex ring with filament strength Γ_i. Thus, the potential jump across the ith element is just Γ_i, and the time-averaged force and moment on the helicopter may be approximated by

$$\mathbf{F} = \frac{\rho}{T} \sum_{i=1}^{M} \mathbf{n}_i \, \Delta A_i \Gamma_i = \sum_{i=1}^{M} \mathbf{b}_i \Gamma_i = \mathbf{B}\, \boldsymbol{\Gamma} \tag{2.16}$$

$$\mathbf{M} = \frac{\rho}{T} \sum_{i=1}^{M} \mathbf{r}_i \times \mathbf{n}_i \, \Delta A_i \Gamma_i = \sum_{i=1}^{M} \mathbf{d}_i \Gamma_i = \mathbf{D}\, \boldsymbol{\Gamma} \tag{2.17}$$

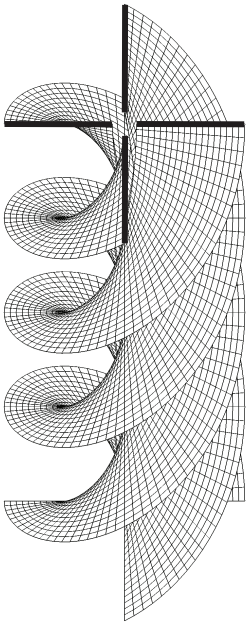

FIGURE 2.4: Wake due to one complete rotation of a four-bladed rotor in forward flight with advance ratio $\mu = 0.5$ as viewed from above. The wake is represented by quadrilateral vortex rings. Note that because of the periodicity in the problem, a four-bladed rotor can be modeled by just one quarter turn of the wake; a full turn is shown here for clarity.

Likewise, the total power loss is approximated by

$$\begin{aligned} P &= \frac{1}{2}\sum_{i=1}^{M}\sum_{j=1}^{M} K_{ij}\Gamma_i\Gamma_j - \sum_{i=1}^{M} Q_i\Gamma_i + P_{\mathrm{v}0} \\ &= \frac{1}{2}\boldsymbol{\Gamma}^T\mathbf{K}\,\boldsymbol{\Gamma} - \boldsymbol{\Gamma}^T\,\mathbf{Q} + P_{\mathrm{v}0} \end{aligned} \tag{2.18}$$

with

$$K_{ij} = -\frac{\rho}{T}\mathbf{w}_{ij}\cdot\mathbf{n}_i\,\Delta A_i + \delta_{ij}\frac{\rho}{T}\left[\frac{4c_{d2}}{c}\right]_i \Delta A_i \tag{2.19}$$

$$Q_i = 2\frac{\rho}{T}u_i\left[c_{\ell 0}c_{d2}\right]_i \Delta A_i \tag{2.20}$$

$$P_{\mathrm{v}0} = \frac{\rho}{2T}\sum_{i=1}^{M} u_i^2\left[c\left(c_{d0} + c_{d2}c_{\ell 0}^2\right)\right]_i \Delta A_i \tag{2.21}$$

making the discretized form of the Lagrangian power

$$\Pi = \frac{1}{2}\boldsymbol{\Gamma}^T\mathbf{K}\boldsymbol{\Gamma} - \boldsymbol{\Gamma}^T\mathbf{Q} + P_{v0} + \boldsymbol{\lambda}_F \cdot (\mathbf{B}\boldsymbol{\Gamma} - \mathbf{F}_R) + \boldsymbol{\lambda}_M \cdot (\mathbf{D}\boldsymbol{\Gamma} - \mathbf{M}_R) \tag{2.22}$$

Minimizing the power, which is quadratic in the circulation, subject to lift and trim constraints that are linear in circulation is a so-called quadratic programming problem. Using the calculus of variations, we find the solution is given by

$$\begin{bmatrix} \frac{1}{2}(\mathbf{K}+\mathbf{K}^T) & \mathbf{B}^T & \mathbf{D}^T \\ \mathbf{B} & \mathbf{0} & \mathbf{0} \\ \mathbf{D} & \mathbf{0} & \mathbf{0} \end{bmatrix} \begin{Bmatrix} \boldsymbol{\Gamma} \\ \boldsymbol{\lambda}_F \\ \boldsymbol{\lambda}_M \end{Bmatrix} = \begin{Bmatrix} \mathbf{Q} \\ \mathbf{F}_R \\ \mathbf{M}_R \end{Bmatrix} \tag{2.23}$$

Note Eq. (2.23) is linear, making it particularly easy to solve. However, the computed optimum circulation must be checked to determine whether any portion of the rotor blade has a circulation resulting in a coefficient of lift exceeding the stall limits. If so, one must introduce the stall inequality constraints making the problem nonlinear.

Equation (2.23) describes the minimum power solution for a rubber rotor, allowing one to solve directly for the optimal circulation distribution without regard to the blade control or planform required to achieve this distribution. For real aircraft, however, one will not be able to obtain the optimum rubber rotor circulation distribution because the number of inputs to the system is finite. In the next chapter, we consider the optimum performance of real rotors with a finite number of design variables and control inputs including fixed radial blade twist and chord distributions and conventional and higher harmonic blade control.

3

Optimal Rotor Control and Design

The previous chapter outlines a method to solve for the optimal circulation distribution of a helicopter rotor with no regard to the control inputs required to achieve this circulation distribution. This is referred to as the rubber rotor solution, and represents the optimal performance achievable if the rotor could be articulated with infinite degrees of freedom, providing a rigorous upper bound on the performance of a rotor.

In this chapter, two techniques are presented to solve for the optimal circulation distribution subject to the constraint that the circulation is realizable using a given set of design variables and control inputs. The first method, outlined in Section 3.2 is a quadratic programming (QP) approach. The QP formulation assumes small angles of attack, a linearized lift curve (i.e. no stall at high angles of attack), and a quadratic drag polar (as shown in Figure 2.3). Additionally, the QP approach is not capable of optimizing the blade chord as a design variable, although any arbitrary fixed chord distribution can be analyzed with this method. The second method, outlined in Section 3.4, is a Nonlinear Programming (NLP) approach. The full nonlinear formulation of the problem is solved with Newton iteration. Additionally, a second

approach to solving the nonlinear problem is described in Appendix A. This technique uses Mathematical Programming via Augmented Lagrangians using the Broyden-Fletcher-Goldfarb-Shanno (BFGS) gradient based variable metric method [8] to solve the successive unconstrained minimization problems.

3.1 Defining Design Variables

In the design of a rotor, one may select a fixed blade twist distribution $\theta_0(r)$, and also implement some limited set of harmonic blade pitch control inputs. For such a configuration, the blade twist as a function of radius r and azimuth ψ can be described as

$$\theta(r,\psi) = \theta_0(r) + A_0 + \sum_{n=1}^{N} A_n \cos(n\psi) + \sum_{n=1}^{N} B_n \sin(n\psi) \tag{3.1}$$

where A_n and B_n are the Fourier coefficients of the blade pitch and N is the number of harmonics in the higher harmonic control system. A conventional helicopter with collective and cyclic control corresponds to $N = 1$.

We denote the total vector of design variables by $\mathbf{\Theta}$. This vector is comprised of two distinct vectors

$$\mathbf{\Theta} = \left\{ \begin{array}{c} \mathbf{\Theta}_\theta \\ \mathbf{\Theta}_\mathrm{c} \end{array} \right\} \tag{3.2}$$

where $\mathbf{\Theta}_\theta$ contains the design variables that affect the pitch angle of the blade or wing, including the fixed radial twist and some form of azimuthal pitch control, such as a root pitch input or some other method such as the use of spanwise flaps. $\mathbf{\Theta}_\mathrm{c}$ then contains the design variables that affect the chord distribution. For a harmonic blade pitch control scheme as shown in Equation (3.1), the vector $\mathbf{\Theta}_\theta$ will be comprised of the Fourier coefficients of blade pitch A_0, A_n, and B_n, and $\theta_0(r)$ at a discrete set of radii. Alternatively $\theta_0(r)$ may be represented by a summation of shape functions

in the radial direction, in which case the coefficients of the shape functions would be members of $\mathbf{\Theta}_\theta$. Similarly, if the chord distribution is to be optimized, $\mathbf{\Theta}_\mathrm{c}$ will contain either the value of the chord at a discrete set of radii or the coefficients of the shape functions that describe the chord distribution. We define the number of elements in $\mathbf{\Theta}_\theta$ as f and the number of elements in $\mathbf{\Theta}_\mathrm{c}$ as g. We define the total number of design variables as h, which is of course equal to $f + g$.

The vector $\mathbf{\Theta}$ relates some limited set of design variables to the blade pitch and chord at every panel in the vortex lattice grid. We denote the pitch angle at each panel due to the design variables as the vector $\boldsymbol{\theta}$ and the chord at each panel as the vector $\mathbf{c}$. These vectors both have length M, where M is the number of panels in the vortex lattice grid. It will be useful in the following derivations to define a set of matrices that transform $\mathbf{\Theta}$ or some portion of $\mathbf{\Theta}$ into the values of twist and chord at each panel as follows:

$$\left\{ \begin{array}{c} \boldsymbol{\theta} \\ \mathbf{c} \end{array} \right\} = \mathbf{S}_\mathrm{total}\mathbf{\Theta} \tag{3.3}$$

$$\boldsymbol{\theta} = \mathbf{S}_\theta\mathbf{\Theta}_\theta \tag{3.4}$$

$$\mathbf{c} = \mathbf{S}_\mathrm{c}\mathbf{\Theta}_\mathrm{c} \tag{3.5}$$

Lastly, when implementing certain chord constraints it is advantageous to expand $\mathbf{\Theta}_c$ into a vector representing the chord at a single set of panels along the span of a blade, $\mathbf{c}_\mathrm{span}$. We define $\mathbf{S}_\mathrm{cRadial}$ such that

$$\mathbf{c}_\mathrm{span} = \mathbf{S}_\mathrm{cRadial}\mathbf{\Theta}_c \tag{3.6}$$

The entries of each of the $\mathbf{S}$ matrices will depend on the global or local shape functions used to represent blade twist and chord.

3.2 Quadratic Programming Approach

3.2.1 Motivation

To compute the forces, moments, and power on a rotor, we must find the circulation in terms of the design variables contained in $\boldsymbol{\Theta}$. In this study, we use a lifting-line approximation to compute the wash on the blades. Using our lightly loaded model, the induced wash is a linear function of the circulation. However, the resulting induced angles of attack on the rotor blade can be large, especially in and near the reverse flow region – large enough to require the use of a nonlinear lift curve – rendering the circulation a nonlinear function of the control inputs. The circulation is also a nonlinear function of the blade chord, so for problems involving chord optimization, these nonlinearities cause the power to be non-quadratic in the design variables, and the constraints to be nonlinear. An approach to solving this nonlinear optimization problem is discussed in Section 3.3.

In general, nonlinear constrained optimization problems are difficult and expensive to solve. In this section, we propose a very efficient small disturbance formulation of the optimization problem. To make the nonlinear optimization more tractable, we first approximate the angles of attack as small, the lift curve as linear, and the drag curve as quadratic. Additionally, we do not include chord variables in the vector of design variables to be optimized, meaning we only consider the vector of pitch angle inputs $\boldsymbol{\Theta}_\theta$ as optimization variables. Based on these assumptions, the power is quadratic in circulation and the problem can be solved using quadratic programming, similar to the approach to solving the rubber rotor optimization problem described in Section 2.5.

3.2.2 Method

To efficiently solve for the optimal controls, we use the Prandtl lifting-line approximation with a near-field vortex lattice model of the wake to relate the control inputs $\mathbf{\Theta}$ to the near field circulation $\mathbf{\Gamma}_{\text{NF}}$ and the wash on the blade $\mathbf{w}$. The induced wash at the blade is calculated using the the rigid wake model of quadrilaterals described in Section 2.5 and shown in Figure 2.4, with the exception that each radial line of panels only accounts for the influence of those panels that preceded them in time, i.e., the wake is semi-infinite, extending backwards in the direction opposite of flight. Through the use of the Biot-Savart law, we form the influence coefficient matrix $\mathbf{M}$ that relates the circulation in the wake to the normal component of induced wash at the blade. The linearized lifting line equation at the i^{th} station in the wake, assuming incompressible flow, can be written as

$$\frac{2\Gamma_{\text{NF}i}}{u_i c_i (c_{\ell\alpha})_i} + \alpha_{\text{ind}i} = \alpha_{\text{geo}_i} \tag{3.7}$$

where $c_{\ell\alpha}$ is the lift curve slope, c is the chord, α_{ind} is the induced angle of attack, and u is the relative fluid velocity perpindicular to the span of the blade.

To account for compressibility effects, the Prandtl-Glauert transformation is used to modify $c_{\ell\alpha}$ based on the local Mach number, M_i, resulting in the compressible version of Equation (3.7), that is,

$$\frac{2\Gamma_i \sqrt{1 - {M_i}^2}}{u_i c_i (c_{\ell\alpha})_i} + \alpha_{\text{ind}i} = \alpha_{\text{geo}_i} \tag{3.8}$$

The induced angle of attack α_{ind} is a function of the normal component of induced wash at the blade w_i and the local velocity u_i. We make use of the small angle approximation: $\tan(\alpha) \approx \alpha$, so that $\alpha_{\text{ind}i} \approx \frac{w_i}{u_i}$. Thus, in this approximation, the induced angle of attack is linear in the circulation. The induced angle of attack at

each panel in the discretized wake can then be related to the circulation $\mathbf{\Gamma}_{\mathrm{NF}}$ through the matrix $\mathbf{W}_{\alpha}$

$$\boldsymbol{\alpha}_{\mathrm{ind}} = \mathbf{W}_{\alpha}\mathbf{\Gamma}_{\mathrm{NF}} \tag{3.9}$$

with the entries of $\mathbf{W}_{\alpha}$ given by

$$W_{\alpha ij} = \frac{W_{ij}}{u_i} \tag{3.10}$$

Combining Equation (3.7) and the Equation (3.9) expression for α_{ind} gives

$$\mathbf{A}_{\mathrm{LL}}\mathbf{\Gamma}_{\mathrm{NF}} = \boldsymbol{\alpha}_{geo} \tag{3.11}$$

with the entries of $\mathbf{A}_{\mathrm{LL}}$ for the compressible case given by

$$A_{\mathrm{LL}ij} = \frac{2\delta_{ij}\sqrt{1-{M_i}^2}}{u_i c_i (c_{\ell\alpha})_i} + W_{\alpha ij} \tag{3.12}$$

where δ_{ij} is the Kronecker delta function. The circulation can be found from Equation (3.9) by inverting the matrix $\mathbf{A}_{\mathrm{LL}}$, yielding

$$\mathbf{\Gamma}_{\mathrm{NF}} = {\mathbf{A}_{\mathrm{LL}}}^{-1}\boldsymbol{\alpha}_{\mathrm{geo}} \tag{3.13}$$

The unknown quantity we wish to solve for is the vector of design variables, $\mathbf{\Theta}_{\theta}$. It is therefore advantageous to separate the angle $\boldsymbol{\alpha}_{\mathrm{geo}}$ into two components: an angle of attack resulting from the initial position of the blade with zero control inputs, called $\boldsymbol{\alpha}_0$, and an angle resulting from the control inputs pitching the blade by some amount, called $\boldsymbol{\theta}$. $\boldsymbol{\alpha}_{\mathrm{geo}}$ is then equal to the sum of these two angles, making Equation (3.13)

$$\mathbf{\Gamma}_{\mathrm{NF}} = {\mathbf{A}_{\mathrm{LL}}}^{-1}\boldsymbol{\alpha}_0 + {\mathbf{A}_{\mathrm{LL}}}^{-1}\boldsymbol{\theta} \tag{3.14}$$

We now use the $\mathbf{S}_{\theta}$ matrix to expand $\mathbf{\Theta}_{\theta}$, the vector of design variables, into the vector $\boldsymbol{\theta}$, which contains the pitch angle change due to the design variables at each panel in the grid. Substituting $\mathbf{S}_{\theta}\mathbf{\Theta}_{\theta}$ for $\boldsymbol{\theta}$ gives

$$\mathbf{\Gamma}_{\mathrm{NF}} = {\mathbf{A}_{\mathrm{LL}}}^{-1}\boldsymbol{\alpha}_0 + {\mathbf{A}_{\mathrm{LL}}}^{-1}\mathbf{S}_{\theta}\mathbf{\Theta}_{\theta} \tag{3.15}$$

Next, we relate the near field circulation to the far field circulation, and use the methods of Section 2 to calculate induced and viscous power, moments, and forces from the far field circulation. For the Prandtl lifting line approximation, this involves a trivial mapping of the bound circulation on the rotor blade to its corresponding position in the far wake, such that

$$\mathbf{\Gamma}_{\mathrm{FF}} = \mathbf{\Gamma}_{\mathrm{NF}} \tag{3.16}$$

For simplicity, we will denote $\mathbf{\Gamma}_0 = {\mathbf{A}_{\mathrm{LL}}}^{-1}\boldsymbol{\alpha}_0$ and $\mathbf{A} = {\mathbf{A}_{\mathrm{LL}}}^{-1}\mathbf{S}_\theta$, giving the following simplified equation for the far field circulation:

$$\mathbf{\Gamma}_{\mathrm{FF}} = \mathbf{A}\mathbf{\Theta}_\theta + \mathbf{\Gamma}_0 \tag{3.17}$$

The vector $\mathbf{\Gamma_0}$ is the circulation due to zero control inputs (an untwisted blade rotating with no pitch relative to the axis of rotation), and can therefore be determined by the geometry of the wake, which in turn is entirely determined by known variables such as the rotor disk angle of attack and the advance ratio of the vehicle. The only unknown is the small vector of design variables $\mathbf{\Theta}_\theta$. Substituting Equation (3.17) into Equation (2.22) gives the Lagrangian power in terms of the control inputs. Setting the variation of this equation to zero for small variations in the design variables and Lagrange multipliers gives the desired system of linear equations, that is,

$$\begin{bmatrix} \frac{1}{2}\mathbf{A^T}(\mathbf{K}+\mathbf{K^T})\mathbf{A} & \mathbf{A^T}\mathbf{B^T} & \mathbf{A^T}\mathbf{D^T} \\ \mathbf{BA} & \mathbf{0} & \mathbf{0} \\ \mathbf{DA} & \mathbf{0} & \mathbf{0} \end{bmatrix} \begin{Bmatrix} \mathbf{\Theta}_\theta \\ \boldsymbol{\lambda}_F \\ \boldsymbol{\lambda}_M \end{Bmatrix} = \begin{Bmatrix} \mathbf{A^T}(\mathbf{Q}-\mathbf{K\Gamma_0}) \\ \mathbf{F_R}-\mathbf{B\Gamma_0} \\ \mathbf{M_R}-\mathbf{D}\mathbf{\Gamma}_0 \end{Bmatrix} \tag{3.18}$$

Equation (3.18) is solved for the unknown design variables that minimize power for trimmed flight subject to the lift and moment constraints. Once the optimal design variables are known, the resulting circulation distribution is calculated using Equation (3.17). The minimum induced and viscous power losses are then calculated from the far field circulation distribution using Equations (2.16), (2.17), and (2.18).

The QP method, as we shall see, gives reasonably accurate results compared to a full nonlinear search algorithm, but at a fraction of the computational cost. For a single flight condition, the method requires just a few minutes of computational time using a single processor computer, and is thus useful for applications requiring the analysis of many flight conditions. Note that Equation (3.18) assumes small angles of attack, a linear lift curve slope, and a quadratic drag polar, and therefore does not account for the effects of stall at high angles of attack. In the QP formulation we can only solve for the vector $\boldsymbol{\Theta}_\theta$ that contains design variables that affect blade pitch angle (radial blade twist and root pitch inputs, for example). This method is not capable of solving for optimal chord design variables, although a non-uniform chord distribution can be analyzed with the QP approach by including a prescribed chord distribution in Equation (3.12).

Accounting for large angles of attack, nonlinear lift curves, non-quadratic drag polars, and including the chord distribution as a design variable to be optimized renders the problem nonlinear, and introduces additional inequality constraints. Two approaches to solving this nonlinear problem are outlined in the following section.

3.3 Nonlinear Optimization Overview

3.3.1 Motivation

The quadratic programming approach described in the preceding sections assumes a linear lift curve, meaning that stall at high angles of attack is not modeled. Of course, a real airfoil will exhibit stall at certain high angles of attack, as shown in Figure 2.2. Additionally, the previous analysis assumes a quadratic drag polar, which is only a valid assumption in the unstalled region. Inboard portions of a helicopter blade in forward flight experience high angles of attack on the retreating side of the rotor as they enter and exit the reverse flow region, and modeling these high angle of attack aerodynamics may be important for accurate power predictions.

In the optimal circulation model described in Section 2.4 and Reference [14], a constraint on the maximum and minimum coefficient of lift is implemented with Mathematical Programming via Augmented Lagrangians to account for realistic coefficients of lift and drag. However, when optimizing rotor geometric design variables rather than circulation, constraining the maximum and minimum coefficients of lift is not an effective approach. With limited design variables, it may be necessary to accept some blade stall to achieve the overall optimum solution. As a result, it is better to accurately model the high angle of attack aerodynamics rather than constrain the rotor design to avoid this region altogether. Finally, solving the full nonlinear optimization problem allows for the inclusion of chord design variables into the optimization, allowing the planform to be formally optimized.

3.3.2 Nonlinear Iterative Lifting Line Method

We first present a method to calculate the circulation from a given set of rotor design variables in a way that accounts for a nonlinear lift curve and a non-quadratic drag polar, i.e. one that is effective for arbitrary airfoils. We use the numerical nonlinear iterative lifting line method described in References [2] and [3]. This approach uses the vortex-lattice model of the wake described in Sections 2.5 and 3.2 to iteratively compute the circulation resulting from a given set of design variables. The method uses tabular airfoil data to account for the effects of high angles of attack on sectional lift and drag coefficients. The algorithm is:

1. Assume an elliptical circulation distribution along the span of the blade at all azimuthal points in the wake.

2. Calculate the induced angle of attack at each panel using this assumed circulation distribution. With a prescribed circulation, the normal component of

induced wash is given by

$$\mathbf{w} = \mathbf{W}\boldsymbol{\Gamma} \tag{3.19}$$

with $\mathbf{W}$ based on the near field vortex lattice model described in Sections 3.2 and 2.5. The induced angle of attack at the i^{th} panel, $\alpha_{\text{ind}i}$, can be calculated directly as $\alpha_{\text{ind}i} = \tan^{-1}(\frac{w_i}{u_i})$, as there is no need to linearize this term with the small angle approximation. This can make a significant difference in regions of the wake with large induced angles of attack, such as on the retreating side of the rotor where the velocity perpindicular to the span of the panel u is small relative to the induced wash w, making the small angle assumption a poor approximation of the induced angle of attack.

3. Calculate the effective angle of attack at each panel $\alpha_{\text{eff}i}$ using the induced angle of attack calculated in step 2, the angle of attack of the blade due to the geometry of the wake, α_{0i}, and the angle of attack at each station resulting from the design variables, θ_i. In total, the effective angle of attack is given by

$$\alpha_{\text{eff}i} = \alpha_{0i} + \theta_i - \alpha_{\text{ind}i} \tag{3.20}$$

4. Use tabular experimental or numerical data for a given airfoil to determine the appropriate sectional coefficient of lift, c_{l_i}, at each panel based on the effective angle of attack. This is implemented with a lookup table of the Reference [39] airfoil data interpolated using cubic splines. To account for compressibility, the value of c_{l_i} is modified by the Prandtl-Glauert transform,

$$c_{l_{\text{compressible}}} = \frac{c_{l_{\text{incompressible}}}}{\sqrt{1 - M^2}} \tag{3.21}$$

C-81 airfoil data tables, which give the coefficient of lift as a function of effective angle of attack and Mach number, can also be used as the look-up table,

eliminating the need to perform the Prantl-Glauert transform and providing more accurate estimates of compressible effects.

5. Calculate the circulation at each panel based on the value of the sectional lift coefficient using

$$\overline{\Gamma_i} = \frac{1}{2} u_i c_i c_{li} \tag{3.22}$$

6. Update the previous guess of the circulation distribution, $\mathbf{\Gamma}^{n-1}$, using the values $\overline{\mathbf{\Gamma}}$ obtained in step 5 with the following formula

$$\mathbf{\Gamma}^n = \mathbf{\Gamma}^{n-1} + D(\overline{\mathbf{\Gamma}} - \mathbf{\Gamma}^{n-1}) \tag{3.23}$$

   where D is a damping factor used to prevent the iteration from becoming unstable. In general, this iteration must be heavily damped, with values of D ranging from 0.05 - 0.1.

7. Compare the $\mathbf{\Gamma}^n$ and $\mathbf{\Gamma}^{n-1}$ distributions to determine if convergence has been reached. If the iteration has not converged, return to step 2, using $\mathbf{\Gamma}^{n+1}$ as the initial guess at circulation.

The iteration typically reaches convergence within 100-1000 iterations, depending on the damping used, the number of panels in the grid, the initial guess at circulation, and the controls being evaluated. When performing an optimization that incrementally updates the control vector, such as the Newton iteration described in Section 3.4, it is advantageous to use the previous vector of design variable's circulation distribution as the initial guess at circulation in Step 1 to speed up convergence.

Although this iterative method requires a high number of iterations, it requires only a single matrix-vector multiplication per iteration, while all other operations involve updating values within a single vector. As a result, even for grids with a large

number of panels, this method converges in a very short amount of computational time, typically under one or two seconds on a single processor machine.

Once the circulation distribution is known, the forces, moments, and induced power losses are calculated using the far wake approach approach described in Sections 2.1 and 2.2. Because the effective angle of attack is known at each panel following the iteration, sectional drag coefficients can be found found using a lookup table interpolated with cubic splines. The viscous power loss is then calculated using a discretized version of Equation (2.8).

3.4 Newton Iteration

3.4.1 Motivation

We have outlined a nonlinear approach for finding the circulation distribution, forces, moments, and power loss due to a given set of design variables. We now wish to determine the design variables that result in the minimum power loss while satisfying constraints on lift and moments. We use one of two methods for solving this nonlinear constrained optimization problem. The first approach, described in Appendix A, uses the technique of Mathematical Programming via Augmented Lagrangians, with the unconstrained minimization phase of this technique solved using the Broyden–Fletcher–Goldfarb–Shanno (BFGS) variable metric method [8]. The gradients of the augmented cost function are found using adjoint automatic differentiation. The primary drawback of this approach is that it is computationally very slow. A given rotor configuration at a single advance ratio can take over 24 hours to converge, depending on the grid resolution. Additionally, there are many parameters, such as weighting values on penalty terms and constants used in the step size search, that must be varied by trial and error to get a solution that converges in a reasonable amount of time.

In this section, we present a method for solving the constrained nonlinear opti-

mization problem using Newton iteration. This approach approximates the circulation as linear about some set of design variables. The change in design variables required to satisfy all of the constraints and minimize power to first order accuracy can then be found by solving a system of linear equations, in a manner similar to the QP method described in Section 3.2. Since the relationship between circulation and design variables is nonlinear, this process must be done repeatedly, with the circulation linearized about a new baseline set of design variables at each successive step.

This method has several advantages over the Mathematical Programming via Augmented Lagrangians technique presented in Appendix A. First, it is much more computationally efficient, and typically converges in fewer iterations. Second, we can avoid the use of penalty functions that require arbitrary weighting functions to enforce the equality constraints, since at each iteration the linearized problem will satisfy the constraints to first-order exactly.

3.4.2 Linearizing the Circulation About a Set of Design Variables

We know that the circulation is a nonlinear function of the design variables

$$\mathbf{\Gamma} = \mathbf{\Gamma}(\mathbf{\Theta}) \tag{3.24}$$

We can also define the residual as

$$\mathbf{R} = \mathbf{R}(\mathbf{\Gamma}, \mathbf{\Theta}) = 0 \tag{3.25}$$

where $\mathbf{R}$ is a system of nonlinear equations describing the relationship between the circulation and the rotor design variables. In the present analysis, we use the nonlinear lifting line analysis described in Section 3.3.2, but $\mathbf{R}$ could also describe some other numerical method for computing the circulation in terms of the design variables, e.g., a panel method. We want to approximate the circulation at a new set of

design variables as a linear function of the change in controls. If we have a known circulation $\boldsymbol{\Gamma}_0$ about an initial set of design variables $\boldsymbol{\Theta}_0$, the circulation at design variables $\boldsymbol{\Theta} = \boldsymbol{\Theta}_0 + \boldsymbol{\Delta\Theta}$, can be approximated to first order as

$$\boldsymbol{\Gamma} \approx \boldsymbol{\Gamma}_0 + \mathbf{A}\boldsymbol{\Delta\Theta} \tag{3.26}$$

where the matrix $\mathbf{A}$ is defined as

$$\mathbf{A} = \frac{\partial \boldsymbol{\Gamma}}{\partial \boldsymbol{\Theta}^T} \tag{3.27}$$

The matrix $\mathbf{A}$ relates a change in the design variables vector, which can include a change in the chord distribution, to a linear change in the circulation. Of course, because the circulation is a nonlinear function of the design variables, Equation (3.26) is only correct to first order in $\boldsymbol{\Delta\Theta}$. We compute the entires of $\mathbf{A}$ by Taylor expanding to first-order the statement of sectional lift given by the Kutta-Joukowski theorem ($L = \rho U \Gamma$) in terms of small changes in local angle of attack and chord. This process is described in further detail in Section 3.4.4.

Because induced power is quadratic in circulation ($P_i = \frac{1}{2}\boldsymbol{\Gamma}^T\mathbf{K}\boldsymbol{\Gamma}$), through Equation (3.27) we can approximate the change in induced power due to a change in the design variables.

To optimize the total power, or the sum of the viscous and induced powers, we must also express the first-order change in viscous power in terms of a change in design variables. However, viscous power is not directly related to the circulation distribution. Instead, we define a vector $\mathbf{K}_v$ such that

$$\mathbf{K}_v = \frac{\partial P_v}{\partial \boldsymbol{\Theta}^T} \tag{3.28}$$

i.e., $\mathbf{K}_v$ relates a change in design variables to the resulting first-order change in viscous power loss. Thus,

$$P_v \approx P_{v0} + \mathbf{K}_v^T \boldsymbol{\Delta\Theta} \tag{3.29}$$

where P_{v0} is the viscous power about some initial set of design variables. We determine the entries of the $\mathbf{K}_v$ vector by Taylor expanding to first-order the expression for viscous power for small changes in chord and angle of attack. This process is detailed in Section 3.4.5.

3.4.3 Formulating the Variational Problem

To formulate the variational problem, we start with the statement of Lagrangian power from Section 2.5:

$$\Pi = \frac{1}{2}\mathbf{\Gamma}^T\mathbf{K}\mathbf{\Gamma} + P_v + \boldsymbol{\lambda}_F{}^T(\mathbf{B}\mathbf{\Gamma} - \mathbf{F_R}) + \boldsymbol{\lambda}_\mathbf{M}{}^\mathbf{T}(\mathbf{D}\mathbf{\Gamma} - \mathbf{M_R}) \tag{3.30}$$

Plugging the expression for circulation found in Equation (3.26) into Equation (3.30) and including the linearized viscous power loss given in Equation (3.29) gives

$$\begin{aligned}\Pi = \frac{1}{2}(\mathbf{\Gamma}_0 + \mathbf{A}\Delta\mathbf{\Theta})^T\mathbf{K}(\mathbf{\Gamma}_0 + \mathbf{A}\Delta\mathbf{\Theta}) + P_{v0} + \mathbf{K}_v^T\Delta\mathbf{\Theta} + \boldsymbol{\lambda}_F{}^T(\mathbf{B}(\mathbf{\Gamma_0} + \mathbf{A}\mathbf{\Delta\Theta}) - \mathbf{F_R}) \\ + \boldsymbol{\lambda}_M{}^T(\mathbf{D}(\mathbf{\Gamma_0} + \mathbf{A}\mathbf{\Delta\Theta}) - \mathbf{M_R})\end{aligned} \tag{3.31}$$

Taking the variation of Equation (3.31) and setting the result to zero for arbitrary variations in the change in design variables $\mathbf{\Delta\Theta}$ and Lagrange multipliers gives the following set of linear equations:

$$\begin{bmatrix} \frac{1}{2}\mathbf{A^T}(\mathbf{K}+\mathbf{K^T})\mathbf{A} & \mathbf{A^T}\mathbf{B^T} & \mathbf{A^T}\mathbf{D^T} \\ \mathbf{BA} & \mathbf{0} & \mathbf{0} \\ \mathbf{DA} & \mathbf{0} & \mathbf{0} \end{bmatrix} \begin{Bmatrix} \mathbf{\Delta\Theta} \\ \boldsymbol{\lambda}_F \\ \boldsymbol{\lambda}_M \end{Bmatrix} = \begin{Bmatrix} -\mathbf{A^T}\mathbf{K}\mathbf{\Gamma}_0 - \mathbf{K}_v \\ \mathbf{F_R} - \mathbf{B}\mathbf{\Gamma}_0 \\ \mathbf{M_R} - \mathbf{D}\mathbf{\Gamma}_0 \end{Bmatrix} \tag{3.32}$$

To perform an inviscid analysis (i.e., to minimize induced power only), the $\mathbf{K}_v$ term is simply set to zero. At each step of the iteration, this system of equations is solved, satisfying the equality constraints and minimizing the induced or total power to first order. The vector of design variables is then updated at each iteration as follows:

$$\mathbf{\Theta}^{k+1} = \mathbf{\Theta}^k + D\Delta\mathbf{\Theta} \tag{3.33}$$

where D is an under-relaxation factor discussed further in Section 3.4.7. Of course, if $D = 1$, the linearized circulation at controls $\boldsymbol{\Theta}^{k+1}$, which will satisfy all constraints, is simply

$$\boldsymbol{\Gamma}^{k+1} = \boldsymbol{\Gamma}^{k} + \mathbf{A}\Delta\boldsymbol{\Theta} \tag{3.34}$$

However, since this linearized relationship is only a first-order approximation, the residual $\mathbf{R}(\boldsymbol{\Gamma}^{k+1}, \boldsymbol{\Theta}^{k+1})$ will be non-zero. It is necessary to calculate the accurate, nonlinear circulation at $\boldsymbol{\Theta}^{k+1}$ after each each iteration using the nonlinear iterative lifting line procedure described in Section 3.3.2, i.e., to determine the circulation distribution $\boldsymbol{\Gamma}$ that makes $\mathbf{R}(\boldsymbol{\Gamma}, \boldsymbol{\Theta}^{k+1}) = 0$. As the iteration steps closer to the true solution and the step sizes become smaller, the linear approximation of circulation will be more and more accurate, causing the residual to decrease until the solution converges.

In summary, the algorithm for the Newton iteration is:

1. Select an initial guess at the vector of design variables, $\boldsymbol{\Theta}$, and use this as $\boldsymbol{\Theta}^{k}$ on the first iteration.

2. Find $\boldsymbol{\Gamma}^{k}$ based on $\boldsymbol{\Theta}^{k}$ using the nonlinear iterative lifting line method.

3. Use $\boldsymbol{\Gamma}^{k}$ and $\boldsymbol{\Theta}^{k}$ to form the matrix $\mathbf{A}$, defined as the first order change in circulation due to a change in design variables.

4. Assemble and solve the linear system of equations given in (3.32).

5. Update the vector of design variables: $\boldsymbol{\Theta}^{k+1} = \boldsymbol{\Theta}^{k} + D\Delta\boldsymbol{\Theta}$, where D is an under-relaxation factor.

6. Set $\boldsymbol{\Theta}^{k} := \boldsymbol{\Theta}^{k+1}$ and return to step 2 until the iteration has converged.

3.4.4 Determining the Entries of the **A** *Matrix*

To determine the entries of the **A** matrix, we start with the following expression for circulation at each panel, obtained from equating the lift calculated by the Kutta-Joukowski theorem with the definition of the sectional coefficient of lift:

$$L_i = \rho u_i \Gamma_i = \frac{1}{2} \rho {u_i}^2 c_i \left(c_{\ell\alpha}\right)_i \alpha_i \tag{3.35}$$

Solving for Γ_i gives,

$$\Gamma_i = \frac{1}{2} u_i c_i \left(c_{\ell\alpha}\right)_i \alpha_i \tag{3.36}$$

Taylor expanding this equation and retaining first-order terms to approximate $\Delta\Gamma_i$ due to changes in the local angle of attack α_i and local changes in chord c_i gives

$$\Delta\Gamma_i = \frac{1}{2} u_i c_i \left(c_{\ell\alpha}\right)_i \Delta\alpha_i + \frac{1}{2} u_i c_{li} \Delta c_i \tag{3.37}$$

The $\Delta\alpha_i$ term can be replaced by the sum of two distinct changes in angle of attack: a change in the induced angle of attack, $\Delta\alpha_{\text{ind}i}$, and a change in the angle of attack due to a change in the design variables vector, which will be referred to as $\Delta\theta_i$. Thus,

$$\Delta\Gamma_i = \frac{1}{2} u_i c_i \left(c_{\ell\alpha}\right)_i \left(\Delta\theta_i - \Delta\alpha_{\text{ind}i}\right) + \frac{1}{2} u_i c_{li} \Delta c_i \tag{3.38}$$

Next, we wish to put $\Delta\alpha_{\text{ind}i}$ in terms of a change in the circulation distribution, $\mathbf{\Delta\Gamma}$. Starting with the following definition

$$\alpha_{\text{ind}i} = \tan^{-1}\left(\frac{w_i}{u_i}\right) \tag{3.39}$$

and Taylor expanding Equation (3.39) in terms of the induced wash, w_i, and retaining first order terms gives

$$\Delta\alpha_{\text{ind}i} = \left(\frac{1}{1 + \left(\frac{w_i}{u_i}\right)^2}\right) \frac{\Delta w_i}{u_i} \tag{3.40}$$

The wash at each panel is related to the circulation through the influence coefficient matrix $\mathbf{W}$:

$$\mathbf{w} = \mathbf{W}\boldsymbol{\Gamma} \tag{3.41}$$

and therefore, to first order

$$\Delta\mathbf{w} = \mathbf{W}\Delta\boldsymbol{\Gamma} \tag{3.42}$$

and for the i^{th} panel,

$$\Delta w_i = \mathbf{W}_i\Delta\boldsymbol{\Gamma} \tag{3.43}$$

where $\mathbf{W}_i$ is the i^{th} row of the matrix $\mathbf{W}$. Substituting Equation (3.43) into Equation (3.40) and simplifying gives the following expression for $\Delta\alpha_{\mathrm{ind}i}$, i.e.,

$$\Delta\alpha_{\mathrm{ind}_i} = \left(\frac{u_i}{{u_i}^2 + {w_i}^2}\right)\mathbf{W}_i\Delta\boldsymbol{\Gamma} \tag{3.44}$$

Substituting this expression into Equation (3.38) and reorganizing terms gives

$$\Delta\Gamma_i + \frac{1}{2}c_i\left(c_{\ell\alpha}\right)_i\left(\frac{{u_i}^2}{{u_i}^2 + {w_i}^2}\right)\mathbf{W}_i\Delta\boldsymbol{\Gamma} = \frac{1}{2}u_i c_i\left(c_{\ell\alpha}\right)_i\Delta\theta_i + \frac{1}{2}u_i c_{li}\Delta c_i \tag{3.45}$$

Writing this equation in matrix form gives

$$\mathbf{R}_\Gamma\Delta\boldsymbol{\Gamma} = \mathbf{R}_{\theta\mathrm{Full}}\begin{pmatrix}\Delta\boldsymbol{\theta}\\ \Delta\mathbf{c}\end{pmatrix} \tag{3.46}$$

with the elements of matrix $\mathbf{R}_\Gamma$ defined as follows:

$$\mathbf{R}_{\Gamma ij} = \delta_{ij} + \frac{1}{2}c_i\left(c_{\ell\alpha}\right)_i\left(\frac{{u_i}^2}{{u_i}^2 + {w_i}^2}\right)\mathbf{W}_{ij} \tag{3.47}$$

and with $\mathbf{R}_{\theta\mathrm{Full}}$ made up of two diagonal matrices, $\mathbf{R}_\theta$ and $\mathbf{R}_\mathrm{c}$, with their elements defined in Equations 3.49 and 3.50:

$$\mathbf{R}_{\theta\mathrm{Full}} = \{\mathbf{R}_\theta|\mathbf{R}_\mathrm{c}\} \tag{3.48}$$

$$\mathbf{R}_{\theta ij} = \delta_{ij} \frac{1}{2} u_i c_i \left(c_{\ell\alpha}\right)_i \tag{3.49}$$

$$\mathbf{R}_{cij} = \delta_{ij} \frac{1}{2} u_i c_{l_i} \tag{3.50}$$

Note that in Equation (3.46) the vector $\Delta\boldsymbol{\Gamma}$ is of length M, where M is equal to the number of panels in the vortex lattice grid. The vectors $\Delta\boldsymbol{\theta}$ and $\Delta\mathbf{c}$ are each of length M, and the matrix $\mathbf{R}_{\theta\text{Full}}$ has dimensions $M \times 2M$.

Finally, to relate a small change in the vector of design variables $\boldsymbol{\Theta}$ to the change in circulation, we use the $\mathbf{S}_{\text{total}}$ matrix to define $\mathbf{R}_\Theta$ as

$$\mathbf{R}_\Theta = \mathbf{R}_{\theta\text{Full}} \mathbf{S}_{\text{total}} \tag{3.51}$$

allowing Equation (3.46) to be written as

$$\Delta\boldsymbol{\Gamma} = {\mathbf{R}_\Gamma}^{-1} \mathbf{R}_\Theta \Delta\boldsymbol{\Theta} \tag{3.52}$$

The matrices $\mathbf{R}_\Gamma$ and $\mathbf{R}_\Theta$ are the Jacobians of $\mathbf{R}$ with respect to $\boldsymbol{\Gamma}$ and $\boldsymbol{\Theta}$, respectively. Lastly, defining

$$\mathbf{A} = {\mathbf{R}_\Gamma}^{-1} \mathbf{R}_\Theta \tag{3.53}$$

we have formed a single matrix $\mathbf{A}$ of dimensions $M \times h$ that relates the change in each design variable to the corresponding change in circulation to first order accuracy, as stated in Equation (3.27). Note that this matrix $\mathbf{A}$ is very similar to the matrix of the same name used in the QP approach. There are, however, a couple of important differences. First, the QP approach does not account for any changes in chord, and therefore does not include any of the $\mathbf{R}_\text{c}$ terms given in Equation (3.50). Second, the QP approach assumes small induced angles of attack, and does not include the Taylor expansion of the arctangent term, instead simply using the induced angle of attack as an approximation for the arctangent.

3.4.5 Determining the Entries of the Vector $\mathbf{K}_v$

We start with the following equation for the viscous power loss at each discrete panel in the wake

$$P_{vi} = \frac{\rho u_i^2}{2} c_i c_{di} \Delta A_i \tag{3.54}$$

where ΔA_i is the area of the i^{th} panel in the wake. Taylor expanding in terms of changes in the chord distribution, c, and changes in the coefficient of drag due to changes in the angle of attack θ, and retaining first order terms yields

$$\Delta P_{vi} = \frac{\rho u_i^2}{2} \left(\Delta c_i c_{di} + c_i \left(c_{d\alpha} \right)_i \Delta \alpha_i \right) \Delta A_i \tag{3.55}$$

Expressing the change in angle of attack as two separate components, one due to a change in induced angle of attack and one due to a change in design variables, and using the expression for $\Delta \alpha_{\mathrm{ind}\,i}$ from Equation (3.44) gives

$$\Delta P_{vi} = \frac{\rho u_i^2}{2} \left(\Delta c_i c_{di} + c_i \left(c_{d\alpha} \right)_i \Delta \theta_i - c_i \left(c_{d\alpha} \right)_i \left(\frac{u_i}{{u_i}^2 + {w_i}^2} \right) \mathbf{W}_i \Delta \boldsymbol{\Gamma} \right) \Delta A_i \tag{3.56}$$

Using Equation (3.27) to replace $\Delta \boldsymbol{\Gamma}$, and including the matrices $\mathbf{S}_\theta$ and $\mathbf{S}_c$ to put changes in pitch angle $\Delta \boldsymbol{\theta}$ and chord $\Delta \mathbf{c}$ at each panel in terms of the change in design variables $\Delta \boldsymbol{\Theta}_\theta$ and $\Delta \boldsymbol{\Theta}_c$, gives the following equation

$$\Delta P_{vi} = \mathbf{P}_c^T \mathbf{S}_c \Delta \boldsymbol{\Theta}_c + \mathbf{P}_\theta^T \mathbf{S}_\theta \Delta \boldsymbol{\Theta}_\theta - \mathbf{P}_\Theta^T \mathbf{W} \mathbf{A} \Delta \boldsymbol{\Theta} \tag{3.57}$$

This equation shows that the first-order change in viscous power has distinct contributions from the change in chord design variables $\Delta \boldsymbol{\Theta}_c$ and the change in pitch angle design variables, $\Delta \boldsymbol{\Theta}_\theta$. Additionally, there is a third term that results from the change in circulation due to the change in the entire design variables vector $\Delta \boldsymbol{\Theta}$. The elements of the vectors $\mathbf{P}_c$, $\mathbf{P}_\theta$ and $\mathbf{P}_{\boldsymbol{\Theta}}$ are defined as follows

$$\mathbf{P}_{ci} = \frac{\rho u_i^2}{2} c_{di} \Delta A_i \tag{3.58}$$

$$\mathbf{P}_{\theta i} = \frac{\rho u_i^2}{2} c_i \left(c_{d\alpha}\right)_i \Delta A_i \tag{3.59}$$

$$\mathbf{P}_{\mathbf{\Theta} i} = \frac{\rho u_i^2}{2} c_i \left(c_{d\alpha}\right)_i \left(\frac{u_i}{{u_i}^2 + {w_i}^2}\right) \Delta A_i \tag{3.60}$$

We want to combine the terms on the right hand side of Equation (3.57) into a single vector, $\mathbf{K}_v$, such that

$$\Delta P_v = \mathbf{K}_v^T \Delta \mathbf{\Theta} \tag{3.61}$$

To form the $\mathbf{K}_v$ matrix, we make use of the fact that the vector $\Delta\mathbf{\Theta}$ is simply a concatenation of the $\Delta\mathbf{\Theta}_\theta$ and $\Delta\mathbf{\Theta}_c$ vectors, as shown in Equation (3.2), allowing us to sum components of Equation (3.57) as follows

$$\mathbf{K}_v = \left\{ \begin{array}{c} \mathbf{S}_\theta^T \mathbf{P}_\theta \\ \mathbf{S}_c^T \mathbf{P}_c \end{array} \right\} + \left\{ \begin{array}{c} \mathbf{A}^T \mathbf{W}^T \mathbf{P}_\Theta \end{array} \right\} \tag{3.62}$$

Note that the vector $\mathbf{A}^T\mathbf{W}^T\mathbf{P}_\Theta$ is of length h, meaning it has an entry for each design variable. The vector $\mathbf{S}_\theta^T\mathbf{P}_\theta$ has an entry for each twist design variable, while the vector $\mathbf{S}_c^T\mathbf{P}_c$ has an entry for each chord design variable, making the concatenation of these two vectors of length h as well and allowing the two vectors to be summed.

3.4.6 Additional Constraints

Two additional constraints are useful for certain configurations: an equality constraint on the solidity of the rotor, and a set of local inequality constraints on the chord distribution.

Solidity Constraint

It is useful in some circumstances to constrain the thrust weighted solidity of the rotor. As will be discussed in Chapter 5, for coaxial rotors at high forward flight speeds it is aerodynamically optimal to have a very small chord along the entire span of the blade, as the high dynamic pressure on the advancing side of the rotor

requires very little lifting surface to achieve the required lift. Such a rotor is of little practical interest, however, since it would be unable to hover or fly at low speeds. While a chord inequality constraint can be used to prevent excessively small chord values at each radial station, it gives little flexibility to the optimization routine to select a planform, as the planform is essentially prescribed by the minimum chord values. Constraining the thrust weighted solidity ensures adequate blade area while still allowing the optimization to tailor the planform to the aerodynamic optimum. The inequality constraint on chord is still used to prevent negative and infinitesimal chords.

The thrust weighted solidity of the rotor is defined as

$$\sigma_{\mathrm{TW}} \equiv \frac{3}{R^3} \int_0^R \sigma(r) r^2 \mathrm{d}r \tag{3.63}$$

This parameter weights the effects of chord at the tip more heavily than at inboard stations, as changes in the chord further outboard have a larger effect on the thrust of the rotor due to the higher rotational velocities at these stations. Because the thrust weighted solidity heavily weights chord at the blade tip, and because the circulation goes to zero at the tip regardless of the chord, we found that such a constraint produced oddly shaped tip geometries. To alleviate this problem, we constrain instead a modified thrust weighted solidity defined by

$$\sigma_{\mathrm{TWM}} \equiv \frac{3}{R^3} \int_0^R r^2 \sigma(r) \cdot \{1 - \exp[-(1 - r/R)/\epsilon]\} \, \mathrm{d}r \tag{3.64}$$

where ϵ is some constant, typically 0.1. This definition has the effect of reducing the impact of the chord near the tip on solidity, allowing the tip chord to be its aerodynamic optimum rather than being artificially inflated to boost solidity.

Regardless of which definition of solidity is used, the equality constraint on so-

lidity takes the following form

$$\sigma_{\text{constraint}} = \sigma - \sigma_{\text{req}} = 0 \tag{3.65}$$

where σ is the solidity of the rotor (based on whichever definition of solidity is used) and σ_{req} is the required solidity. It is possible to implement the solidity constraint as an inequality constraint in order to place a minimum or maximum value on the rotor's solidity. For simplicity, however, we will implement this constraint as an equality constraint.

Solidity is linearly related to the vector of design variables through Equation (3.63) or a similar sum if using the tip weighted solidity. This sum is expressed as the dot product of the vector $\mathbf{E}$ and the vector of design variables. First, we define the $\mathbf{E}_{\text{full}}$ vector, which when dotted with the vector containing the chord value at every radial station, $\mathbf{c}$, gives the resulting solidity. The entries of $\mathbf{E}_{\text{full}}$ when using the traditional thrust weighted solidity definition, with r_i equal to the radial position of the i^{th} station, are given by

$$\mathbf{E}_{\text{full}i} = \frac{3}{R^3}\sigma_i {r_i}^2 \Delta r_i \tag{3.66}$$

If using global shape functions to represent the chord distribution, $\mathbf{E}_{\text{full}}$ will have to include the linear relationship between the shape function coefficients and the resulting change in chord at each panel. We define the matrix that relates these values as $\mathbf{S}_{\text{cRadial}}$. If not using global shape functions, $\mathbf{S}_{\text{cRadial}}$ is simply the identity matrix. The matrix $\mathbf{E}$ is then given by

$$\mathbf{E} = \mathbf{S}_{\text{cRadial}}\mathbf{E}_{\text{full}} \tag{3.67}$$

The matrix $\mathbf{E}$ now has an entry for every chord coefficient and has length g. To simplify the calculation of solidity, we pad the vector with zeroes in all locations corresponding to angle controls (i.e., blade root input or fixed blade twist) to make

the length of $\mathbf{E}$ equal to h, such that

$$\sigma_{\mathrm{TW}} = \mathbf{E}^T \boldsymbol{\Theta} \tag{3.68}$$

Including the solidity constraint in a simplified Lagrangian power statement then gives

$$\Pi = P_{\mathrm{total}} + \lambda_\sigma [\mathbf{E}^T (\boldsymbol{\Theta} + \Delta\boldsymbol{\Theta}) - \sigma_{\mathrm{req}}] \tag{3.69}$$

Taking the variation of Equation (3.69) gives additional optimality conditions, which are included in the set of linear equations shown in Equation (3.32).

Chord Inequality Constraint

It is typically necessary to apply a set of inequality constraints on the chord distribution, requiring some minimum or maximum chord at all spanwise locations on the blade, to prevent the optimization from taking advantage of physically unrealizable solutions (e.g., infinitesimal or negative chords). It may also be desirable to implement a minimum chord constraint to ensure the optimum blade planform satisfies structural requirements. Additionally, if unconstrained, the chord will often become negative, as this leads to negative profile power loss (an artifact of the 2-d sectional drag model) and is therefore quickly taken advantage of by the optimization. For these reasons, an inequality constraint on the minimum chord is necessary to ensure the solution is reasonable. Similarly, it may be desirable from a design point of view to place a maximum value on the chord, so that capability is also implemented.

While the equality constraints on forces and moments are scalar, the inequality constraint $\mathbf{C}$ is a vector quantity. As written here, this constraint is a minimum chord constraint. Note that by reversing the sign of the constraint, a maximum chord constraint can be implemented using the same approach. The entries of this vector for the constraint on minimum chord are given by

$$C_i = c_i - c_{\mathrm{min}i} \geq 0 \tag{3.70}$$

The chord inequality constraint is implemented using augmented Lagrangians.The Lagrangian power including only this equality constraint is

$$\Pi = P + \boldsymbol{\lambda}_c{}^T \mathbf{C} + \frac{1}{2} W \sum_i^M \frac{(C_i - |C_i|)C_i}{2} \tag{3.71}$$

where W is a weight coefficient. Note that if the inequality constraint at the i^{th} radial station is active, i.e., the chord is below the minimum value, the term $(C_i - |C_i|)C_i/2$ is equal to ${C_i}^2$. If the inequality constraint is not active, then this term is equal to zero.

Of course in the Newton iteration, we are solving for the change in design variables about some nominal starting value. As a result, the chord at each station c_i is expressed as:

$$c_i = c_{0i} + \Delta c_i \tag{3.72}$$

where c_{0i} is the value of the chord going into the current iteration. This makes the elements of the constraint vector $\mathbf{C}$ equal to

$$C_i = c_{0i} + \Delta c_i - c_{\min i} \tag{3.73}$$

Substituting Equation (3.73) into (3.71), gives, in matrix form:

$$\Pi = P + \boldsymbol{\lambda}_c{}^T (\mathbf{c}_0 + \Delta\mathbf{c} - \mathbf{c}_{\min}) + \frac{1}{2}(\mathbf{c}_0 + \Delta\mathbf{c} - \mathbf{c}_{\min})^T \mathbf{W}_c (\mathbf{c}_0 + \Delta\mathbf{c} - \mathbf{c}_{\min}) \tag{3.74}$$

where $\mathbf{W}_c$ is a diagonal weighting matrix, with entries defined as follows

$$\mathbf{W}_{cii} = \begin{cases} W & \text{if } c_{0i} + \Delta c_i - c_{\min i} < 0 \\ 0 & \text{otherwise} \end{cases} \tag{3.75}$$

In other words, if the chord at the i^{th} radial station is in violation of the minimum constraint, the i^{th} entry in the weighting matrix's diagonal will be set to some positive

value W, otherwise it will be zero. Taking the variation of Equation (3.74) with respect to $\boldsymbol{\lambda}_c$ and $\Delta\mathbf{c}^T$, and performing some simplifications yields

$$\delta\Pi = \delta P + \delta\Delta\mathbf{c}^T[\boldsymbol{\lambda}_c^T + \mathbf{W}_c\Delta\mathbf{c} + \mathbf{W}_c(\mathbf{c}_0 - \mathbf{c}_{\min})] + \delta\boldsymbol{\lambda}_c^T(\mathbf{c} + \Delta\mathbf{c} - \mathbf{c}_{\min}) \tag{3.76}$$

The conditions on $\delta\boldsymbol{\lambda}_c^T$ will be fulfilled *a priori* due to the definition of $\boldsymbol{\lambda}_c^T$, and so are not specifically included in the system of linear equations found in Equation 3.32. This is because either C_i is equal to zero and the i^{th} radial station is on the constraint boundary with a non-zero Lagrange multiplier, or the i^{th} radial station is not on the constraint boundary and the Lagrange multiplier λ_{ci} is equal to zero.

The vectors involved in this optimality condition all have a length equal to the number of radial panels in the grid. If using global shape functions to represent the chord distribution, we incorporate the $\mathbf{S}_{\text{cRadial}}$ matrix defined in Equation (3.6) to relate the chord at each radial panel to the shape function coefficients defining the chord distribution. Including this matrix and setting the variation equal to zero for arbitrary changes in chord design variables and Lagrange multipliers gives

$$\delta\Pi = 0 = \boldsymbol{\lambda}_c^T\mathbf{S}_{\text{cRadial}} + \mathbf{S}_{\text{cRadial}}^T\mathbf{W}_c\mathbf{S}_{\text{cRadial}}\Delta\mathbf{c} + \mathbf{W}_c\mathbf{S}_{\text{cRadial}}(\mathbf{c}_0 - \mathbf{c}_{\min}) \tag{3.77}$$

When the chord inequality and solidity constraints are included in the system of linear equations, Equation (3.32) becomes

$$\begin{bmatrix} \frac{1}{2}\mathbf{A}^T(\mathbf{K}+\mathbf{K}^T)\mathbf{A} + \mathbf{S}_{\text{cRadial}}^T\mathbf{W}_c\mathbf{S}_{\text{cRadial}} & \mathbf{A}^T\mathbf{B}^T & \mathbf{A}^T\mathbf{D}^T & \mathbf{E}^T \\ \mathbf{BA} & \mathbf{0} & \mathbf{0} & \mathbf{0} \\ \mathbf{DA} & \mathbf{0} & \mathbf{0} & \mathbf{0} \\ \mathbf{E} & \mathbf{0} & \mathbf{0} & \mathbf{0} \end{bmatrix} \begin{Bmatrix} \Delta\boldsymbol{\Theta} \\ \boldsymbol{\lambda}_F \\ \boldsymbol{\lambda}_M \\ \lambda_\sigma \end{Bmatrix} =$$

$$\begin{Bmatrix} -\mathbf{A}^\mathbf{T}\mathbf{K}\boldsymbol{\Gamma} - \mathbf{K}_v - \mathbf{W}_c\mathbf{S}_{\text{cRadial}}(\mathbf{c}_0 - \mathbf{c}_{\min}) - \boldsymbol{\lambda}_c^T\mathbf{S}_{\text{cRadial}} \\ \mathbf{F_R} - \mathbf{B}\boldsymbol{\Gamma} \\ \mathbf{M_R} - \mathbf{D}\boldsymbol{\Gamma} \\ \sigma_{\text{req}} - \sigma_0 \end{Bmatrix} \tag{3.78}$$

Note that if implementing a chord constraint, the $\mathbf{S}_{\text{cRadial}}^T\mathbf{W}_c\mathbf{S}_{\text{cRadial}}$, $\mathbf{W}_c\mathbf{S}_{\text{cRadial}}(\mathbf{c}_0 - \mathbf{c}_{\min})$, and $\boldsymbol{\lambda}_c^T\mathbf{S}_{\text{cRadial}}$ terms will only be non-zero in rows that include the design

variables that affect chord, $\boldsymbol{\Theta}_c$. However, the same method can be used to implement an inequality constraint on any design variable, including the fixed blade twist and/or the root pitch inputs.

The algorithm for the Newton iteration including the inequality constraint on chord is as follows:

1. Select an initial guess at the vector of design variables, $\boldsymbol{\Theta}$, and use this as $\boldsymbol{\Theta}^k$ on the first iteration.

2. Set $\boldsymbol{\lambda}_c = 0$.

3. Find $\boldsymbol{\Gamma}^k$ based on $\boldsymbol{\Theta}^k$ using the nonlinear iterative lifting line method.

4. Use $\boldsymbol{\Gamma}^k$ and $\boldsymbol{\Theta}^k$ to form the matrix $\mathbf{A}$, defined as the first order change in circulation due to a change in design variables.

5. Use $\boldsymbol{\Theta}^k$ and the current vector of Lagrange multipliers to compute the entries of $\mathbf{W}_c$, $\mathbf{W}_c\mathbf{S}_{\text{cRadial}}(\mathbf{c}_0 - \mathbf{c}_{\min})$, and $\boldsymbol{\lambda}_c^T\mathbf{S}_{\text{cRadial}}$.

6. Assemble and solve the linear system of equations given in (3.78).

7. Update the vector of design variables: $\boldsymbol{\Theta}^{k+1} = \boldsymbol{\Theta}^k + D\Delta\boldsymbol{\Theta}$, where D is an under-relaxation factor.

8. Set $\boldsymbol{\Theta}^k := \boldsymbol{\Theta}^{k+1}$ and return to step 3 until the solution has converged.

9. Once the solution has converged, if a chord inequality constraint is violated, update the chord inequality Lagrange multipliers as follows

$$\text{for } \lambda_{i\text{old}} = 0, \;\; \lambda_{i\text{new}} = \begin{cases} W_3(C_i - |C_i|) & \text{if} < 0 \\ 0 & \text{otherwise} \end{cases} \tag{3.79}$$

$$\text{for } \lambda_{i\text{old}} < 0, \;\; \lambda_{i\text{new}} = \begin{cases} \lambda_{i\text{old}} + W_3 C_i & \text{if} < 0 \\ 0 & \text{otherwise} \end{cases} \tag{3.80}$$

and return to step 3. If no inequality constraints are violated, the optimization is complete.

Similarities to QP Method

Note that the set of equations given in (3.32) is nearly identical to that used in the Quadratic Programming approach given in Equation 3.18, with a couple of important differences. The matrix $\mathbf{A}$ in this case relates both a change in chord and pitch angle design variables to a change in circulation. In the QP approach, it only relates a change in the pitch angle design variables to a change in circulation. Secondly, the QP approach assumes small angles of attack, and therefore approximates $\tan(\boldsymbol{\alpha}_{\text{ind}})$ as α_{ind}, while the Newton method approximates the arctangent term with a first order Taylor expansion. In the QP approach, the controls are linearized about a term $\boldsymbol{\Gamma}_0$, which represents the circulation with no control inputs. In the Newton approach, the circulation is linearized about some known $\boldsymbol{\Gamma}^k$, which is the nonlinear circulation at the previous iteration's design variables. Additionally, the viscous drag model is incorporated differently. In the QP method, viscous drag is separated into its constant, linear, and quadratic components, while in the Newton iteration the entire term is linearized due to the non-quadratic nature of the drag curve outside of the unstalled region. Lastly, the QP approach takes a single step, from zero controls to some final value, while in the Newton approach we iterate, solving for some $\boldsymbol{\Delta\Theta}$ at each iteration, updating the vector of design variables, calculating the nonlinear circulation at this point, and recalculating the $\mathbf{A}$ matrix at each iteration.

3.4.7 Newton Iteration Convergence

The Newton iteration is not guaranteed to converge to a minimum solution that satisfies all constraints. There are two main modes of failure. The first is divergence, which can occur when the iteration steps outside of the feasible region (e.g. steps

to a point with a negative chord variable) and the design variables vector can no longer be accurately related to a circulation distribution. Divergence can also occur when a step is taken to a region far from the optimal solution, and subsequent linearizations of the problem continue pointing in a direction away from any sensible design variables. The second mode of failure is oscillation, where the design variable vector begins oscillating between two or more states rather than converging to one solution.

There are several steps that can be taken to improve convergence. First, the under-relaxation factor D in Equation (3.33) can be set to a value less than one. Certain design variables, particularly angle inputs at panels that are near the stall angle, can have a highly nonlinear relationship to the circulation distribution. As a result, the linearized set of controls that solve Equations (3.78) may be very far off from the optimal solution, and may in fact may not even be close to satisfying the constraints. Use of a damping factor mitigates this problem, as each step can be reduced to a size such that the linearized approximation of circulation is fairly accurate. This allows the vector of design variables to gradually step to the correct nonlinear solution. The damping factor is also often necessary once the iteration is near the optimal solution. Allowing the iteration to take too large a step often results in oscillatory behavior, with the linearized solution constantly overstepping the equality or inequality constraints, thereby never converging to a state that satisfies all constraints.

To demonstrate the effect of the damping value, Figure 3.1 shows the lift and total power at each Newton iteration using various damping factors for the viscous optimization of a coaxial rotor. As shown in the plot, using a damping factor of 0.1 results in a gradual, smooth approach to the required lift and minimum total power. Note that although not shown here, convergence plots of rolling moment and pitching moment would look similar to the required lift plot, with the values converging to

zero. A damping factor of 0.2 initially undershoots the required lift but converges smoothly in about the same number of iterations as the 0.1 case. Damping factors of 0.3 and 0.5 continue to oscillate in both lift and power and never converge. For this case, damping values above 0.5 completely diverge, with the controls assuming nonsensical values and the constrained variables never approaching their required values. Note that these behaviors are dependent on the configuration being run, so these damping values are only representative of a typical case and will not necessarily work or fail for a different configuration.

One of the methods to achieve fastest convergence, as suggested from Figure 3.1, is to start the iteration with a large damping factor, quickly getting the solution close to the optimum. At this point, the damping factor can be decreased, to gradually satisfy the constraints without overshooting and oscillating or continually violating inequality constraints, also resulting in oscillatory behavior.

Another method used to improve convergence is to add a small penalty function to any change in the chord distribution. The relationship between chord variables and circulation is typically more nonlinear than between pitch angle variables and circulation. As a result, slowing down the change in the chord distribution improves the linear approximation of circulation at each step. Another reason to implement this penalty function is that the chord variables are subject to an inequality constraint, while the pitch angle variables are not. As described in Section 3.4.6, the inequality constraint on chord is only imposed *after* each iteration. As a result, large changes in the chord distributions that occur with large step sizes make it more difficult to impose this constraint effectively and more likely that the chord will step to a negative value before the inequality constraint can alter the search direction, causing the iteration to diverge. For these two reasons, it can be advantageous to decrease the magnitude of the change in chord at each iteration, letting the chord distribution slowly approach the nonlinear optimum, and significantly decreasing the chances of

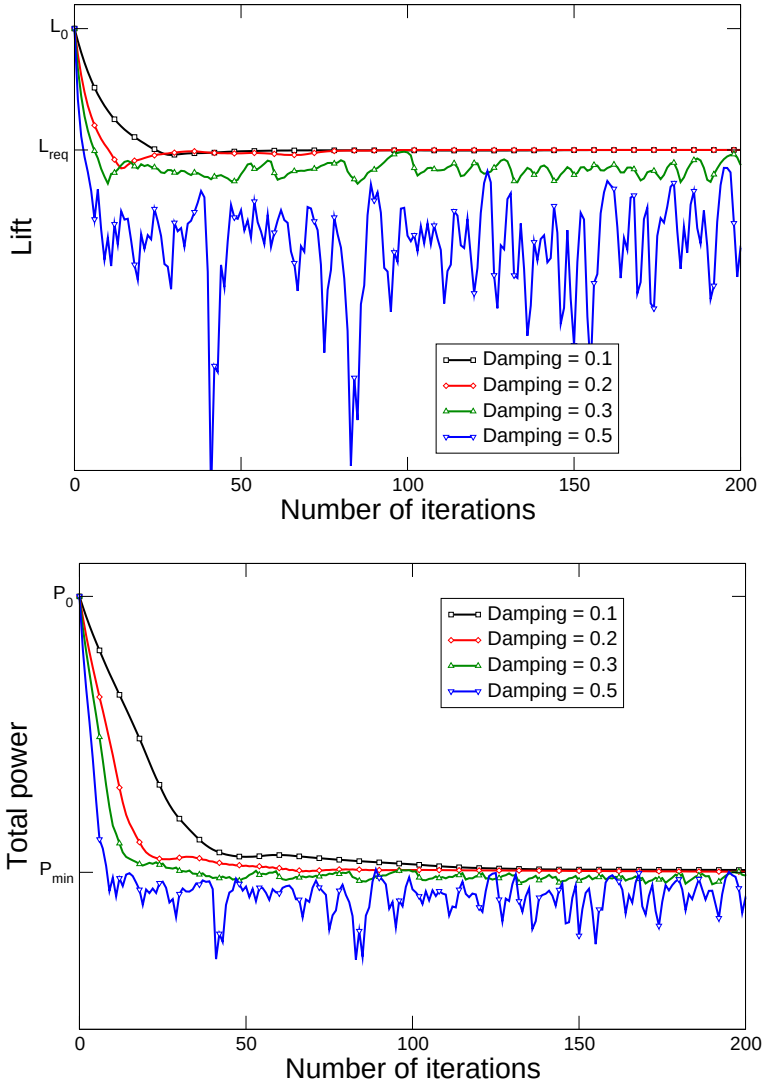

FIGURE 3.1: Convergence of lift and total power for the Newton iteration with various damping values.

divergence or oscillation. This quadratic weighting term $\mathbf{W}_{\text{chord}}$ takes the form of a diagonal matrix added to the inequality weight on chord variables $\mathbf{S}_{\text{cRed}}^T \mathbf{W}_c \mathbf{S}_{\text{cRed}}$ at each iteration in Equation (3.78).

As shown in Figure 3.2, using too small of a weight on the change in chord results in oscillatory behavior similar to that seen when the damping factor is too large. Using the appropriate value allows for a smooth convergence to the required lift, moments, and minimum power. Note that in these plots, a damping factor of

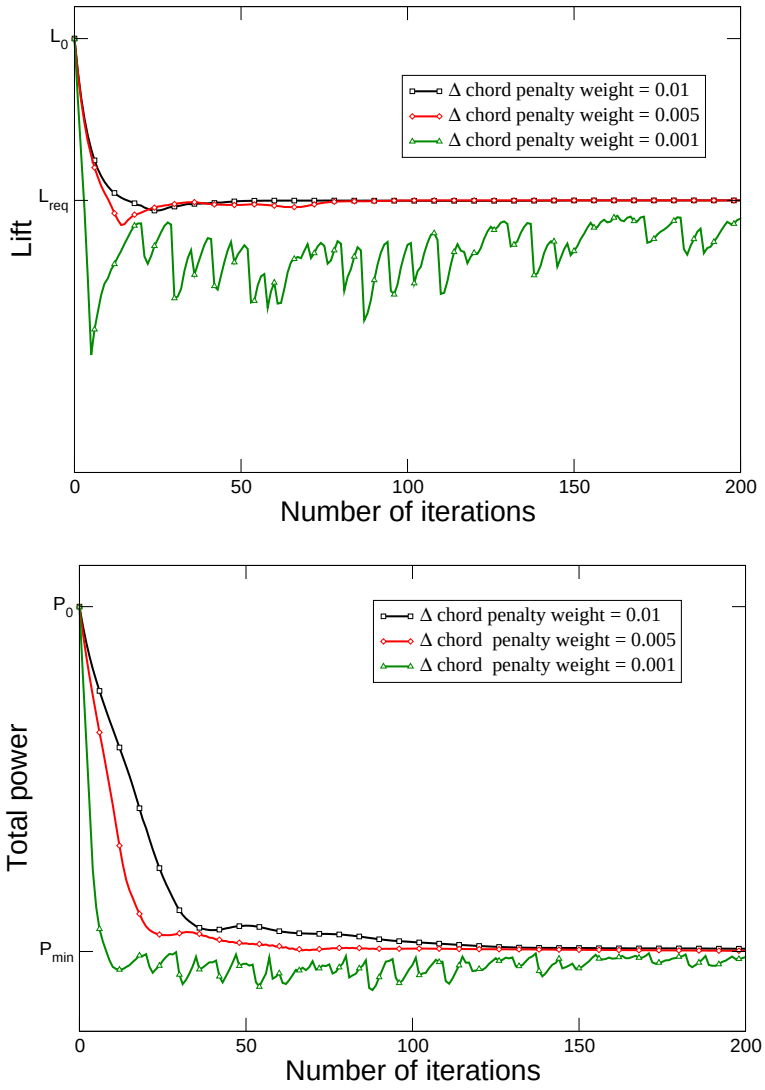

FIGURE 3.2: Convergence of lift and total power for the Newton iteration with various chord penalty weights.

$D = 0.2$ was used. In Figure 3.1, a chord weight of $\mathbf{W}_{\text{chord}} = 0.005$ is used. Both of these terms are required to ensure convergence for this case.

3.5 Comparison of Optimization Routines

In Appendix A, we describe a method of solving the fully nonlinear minimization problem using Mathematical Programming via Augmented Lagrangians. In Section 3.4, we described a method of solving the same problem using a Newton itera-

tion. Both techniques use the nonlinear iterative lifting line method to calculate the power, forces, and moments due to a given set of design variables; the only difference between these methods is the process through which the optimal set of design variables is determined. For a given configuration and flight condition, both methods locate a very similar, though not exactly identical, final set of design variables. The powers and forces associated with the two solutions are well within 1% of each other. To further investigate these discrepancies, a third optimization algorithm was used. Relevant subroutines were converted from FORTRAN90 to Matlab, and Matlab's built in optimization package was used to solve the nonlinear constrained optimization. The minimization was subjected to the same equality and inequality constraints described in the preceeding sections. Matlab's optimization package uses the Active Set Algorithm, which involves linearizing the constraints at each iteration to allow for Sequential Quadratic Programming (SQP). At the formulation of each quadratic programming problem, the Hessian matrix is approximated using the BFGS method. Matlab uses a line search and merit function to modify the step size to prevent constraints from being violated. Matlab's optimization package generated very similar though not identical results to both the NLP and Newton methods.

Figure 3.3 and Table 3.1 show the fixed blade twist and non-dimensional induced power for the case of a coaxial rotor with uniform planform optimized for minimum induced power, as calculated by each of the three optimization routines. As the figure shows, the solutions corresponding to each optimization method are slightly different in each case. It was clear from running a wide range of cases that while all three optimizations typically end up in essentially the same location, there are many local minima near the optimum that result in nearly the same power. Additionally, there are many locations with very small gradients around the solution, resulting in the possibility of an optimization routine stopping or not progressing due to the very flat nature of the minimum. Because each routine is a path dependent line search

Table 3.1: Comparison of non-dimensional power of optimal solutions for inviscid coaxial rotor with no chord variation using various optimization methods.

Method	Non-dimensional power, $\frac{C_{P_i}}{C_l{}^2}$
Newton Iteration	1.2344
Matlab	1.2347
NLP via Augmented Lagrangians	1.2348
Matlab starting at Newton Optimum	1.2344

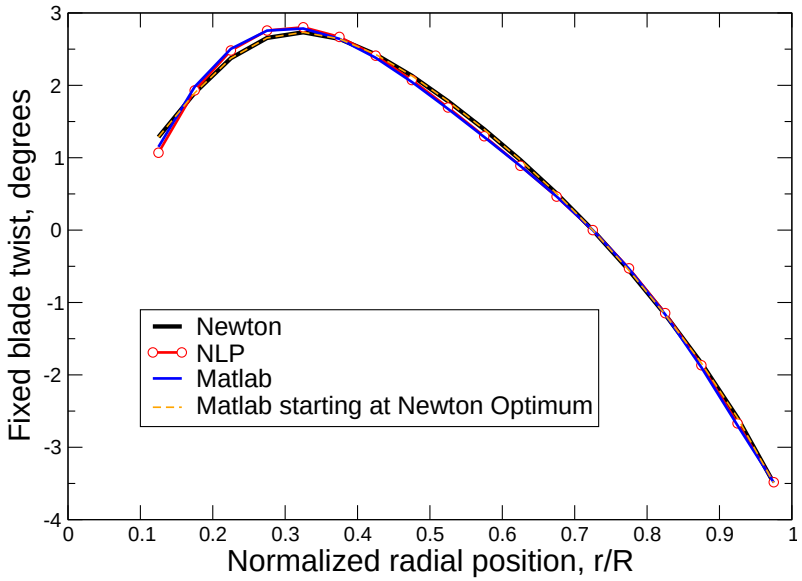

FIGURE 3.3: Comparison of inviscid optimal blade twist between various optimization methods.

algorithm, it is likely that each method is converging to a slightly different local minimum or near-minimum within a very close range. This is further illustrated by the fact that each method is sensitive to the starting point and other factors such as damping factors or weighting terms; altering these factors will change the path of the optimization and can lead to the same method converging to different minima. Also of note, starting the Matlab routine at the Newton solution results in no change in the answer, confirming the fact that the Newton minimum meets the Matlab routine's convergence criteria.

Table 3.2: Comparison of convergence times for various optimization methods.

Method	Approximate time to convergence (hours)
Newton Iteration	6
Matlab	12
NLP via Augmented Lagrangians	38

With all three methods returning nearly identical results, it is worthwhile to compare the merits of each to determine which to use prominently to generate results. In terms of time to convergence, the Newton iteration is typically the fastest algorithm. The computational time is dependent on the configuration being analyzed and the starting point of the iteration. Convergence times for the representative case of a coaxial rotor system (which includes the most panels of any configuration and is therefore the slowest) at a single advance ratio and accounting for viscous effects is shown in Table 3.2. The Newton iteration can be further sped up through various means. As mentioned in Section 3.4.7, the under-relaxation factor can be changed as the iteration progresses, allowing for large initial steps to get close to the solution, then smaller steps through increased damping to ensure there are no oscillations. Additionally, the $\mathbf{A}$ matrix can be re-used between iterations rather than recalculated each time, saving the time required to calculate this matrix. Effective use of these features is dependent on the configuration being analyzed, but can be varied as needed to speed up convergence.

The Newton iteration offers additional benefits apart from the decrease in computational time. The constraints are linearized and enforced at every iteration, whereas in the Mathematical Programming via Augmented Lagrangians method they are enforced using penalty functions with some weighting factor. The penalty function approach is more ad hoc, and can require trial and error to determine the correct weighting factors to ensure convergence in a reasonable time. Additionally, the

Newton iteration uses a simpler technique for step size control, using a uniform or iteration-varying damping factor, while the nonlinear programming via augmented lagrangian method employs the Armijo step size rule that requires two constants used in the search to be selected based on the configuration being analyzed. While the Newton iteration might produce faster computation times with the use of a more involved step size search, the simplicity of the method is an advantage when running many cases in parallel.

The primary advantage of the Newton iteration over the Matlab method is speed. The Matlab routine could possibly be sped up by incorporating an exact gradient calculation. However, given the overall good performance of the Newton algorithm, all of the following nonlinear results were computed using Newton iteration.

3.6 Validation of Linear and Nonlinear Lifting Line Models

Using the linear and nonlinear lifting line analyses described in Sections 3.2 and 3.3.2, respectively, it is possible to determine the circulation resulting from a given set of design variables $\boldsymbol{\Theta}$. The time averaged forces can then be computed from the circulation distribution using the far wake Trefftz volume approach outlined in Chapter 2. To validate both the linear and nonlinear lifting line approaches, a lifting forward flight case of the Caradonna-Tung two bladed rotor [9] was run as a test case. This is a particularly useful case for comparison because the rotor hub is not articulated and the blades are entirely rigid. The same case was used by Allen [1] to validate his unsteady CFD code, and his results are presented here. The C-T rotor has an aspect ratio of 6, a collective pitch setting of 8°, a tip Mach number of 0.7, and an advance ratio of 0.2857, corresponding to a vehicle forward flight Mach number of 0.2. In the case examined, the rotor shaft is inclined 10° into the flow, i.e., it is representative of a rotor generating forward thrust. Using both the linear and nonlinear approaches, and accounting for compressibility in each, we computed a force coefficient on the

blade defined as

$$C_L = \frac{F_z}{\frac{1}{2}\rho(\Omega R)^2 Rc} \tag{3.81}$$

where F_z is the force on the blade in the z direction, R is the radius of the disk, c is the blade chord, and Ω is the rotational rate of the rotor. This coefficient is calculated over the full range of azimuthal locations. Figure 3.4 shows the force coefficient as

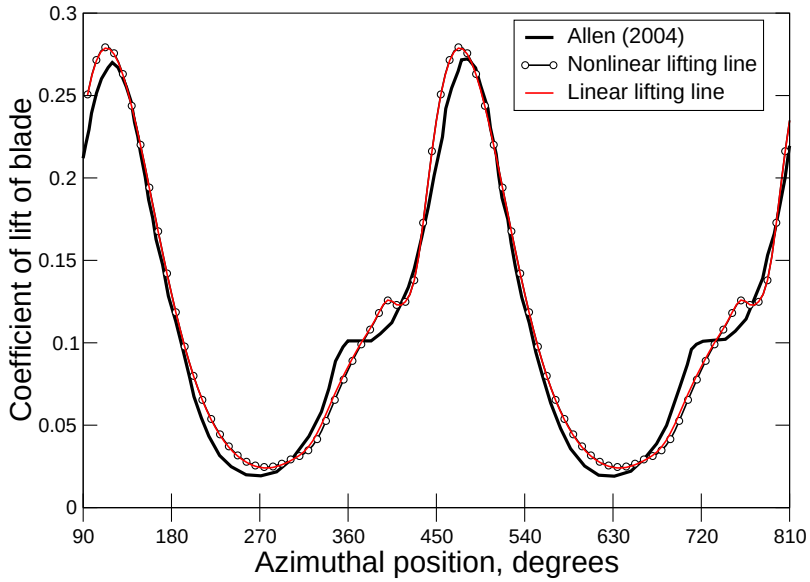

FIGURE 3.4: Comparison of linear and nonlinear lifting line results to Allen (2004) CFD results.

it varies with azimuth computed using our lifting line analysis, and compares our results to Allen's. Allen found that the loading is periodic after the first revolution of the simulation. Our approach assumes periodic behavior and only analyzes a single revolution. For ease of comparison, we have plotted multiple revolutions overlaid with Allen's periodic result.

Our results compare reasonably well with Allen's, indicating that although greatly simplified relative to an unsteady CFD simulation (both the linear and nonlinear cases ran in under two minutes), the linearized and nonlinear lifting line models are able to determine the forces on a rotor in forward flight with reasonable accuracy.

The region of largest discrepancy is at azimuthal angles between $\Psi = 330°$ and $\Psi = 40°$, which is a region in which the blade is strongly affected by the rolled up tip vortex shed from the previous blade. This indicates a slight difference in how the two models treat the convection of the shed tip vortices from each blade. This is to be expected, due to Allen's use of a free wake compared to the rigid wake used in our model. Additionally, this case is run at a relatively low advance ratio, where the rigid wake assumption is less accurate.

Because the case analyzed here is at a relatively low advance ratio, there is a very small reverse flow region on the retreating side of the blade. This results in the blade seeing low effective angles of attack in the unstalled regime in almost all azimuthal and radial locations. Additionally, the region on the retreating side with large effective angles of attack has a low dynamic pressure (due to the low relative velocity to the blade), resulting in this portion of the wake having a small impact on the overall lift of the blade. As a result, the linear and nonlinear lifting methods calculate nearly the same coefficient of lift at all azimuthal locations. This also indicates that the small angle approximations made in the QP approach may be reasonably accurate compared to the fully nonlinear problem, an area that will be explored further in the Results section.

4

Single Rotor Results

In the following chapters, we examine the optimal rotor design and minimum power requirements for various rotor configurations. We use the non-dimensional parameter C_P/C_L^2 to describe power. We choose to normalize the coefficient of power by the coefficient of lift squared because induced power is quadratic with respect to circulation, whereas lift is linear. The total power we refer to in the following results is the sum of the profile and induced power losses of the rotor. This definition is consistent with past work [14] and with the definition given by Ormiston in Reference [30]. Note that the induced, viscous, and total powers referenced here are all power *losses*; therefore a lower value of C_P/C_L^2 indicates more efficient flight.

We also examine the optimal circulation and force distributions. In these cases, we define the normalized circulation and sectional lift force as

$$\overline{\Gamma} = \frac{\rho \Omega R^2 \Gamma}{L} \tag{4.1}$$

$$\bar{l} = \frac{Rl}{L} \tag{4.2}$$

These variables are displayed with contour plots, which show the distribution of

circulation or force on the rotor disk as viewed from a body-fixed set of coordinates. As a result, the rotor appears as a disk. If we viewed the results in the fluid frame of reference, we would see the characteristic skewed helix shown in Figure 2.4. In all cases, the rotor is viewed from above, traveling up the page and rotating counter-clockwise. As a result, the right half of the disk is the advancing side ($\psi = 0° - 180°$) and the left half of the disk is the retreating side ($\psi = 180° - 360°$).

For consistency, we refer to conventional 1/rev control as $N = 1$, 2/rev as $N = 2$, and so forth, with N defined in Equation 3.1. Note then, that per Equation 3.1, $N = 2$ control is actually a superposition of 1/rev and 2/rev pitch inputs.

4.1 Baseline Rotor

In this chapter, we analyze the optimal performance of a conventional helicopter rotor in forward flight. The parameters selected for this configuration were meant to resemble a traditional four bladed helicopter such as the AH-64 Apache. Note that the rotor modeled here does not include any dynamics, such as blade flapping or rotation about the lead/lag hinge, and is therefore more representative of a hingeless, or rigid rotor.

The baseline rotor blades are constant chord, with a 10% root cutout, and an aspect ratio $R/c = 11$, implying a rotor solidity of

$$\sigma \equiv \frac{Bc}{\pi R} = 0.1157 \tag{4.3}$$

Thus, the thrust equivalent rotor solidity is

$$\sigma_{\mathrm{TW}} \equiv \frac{3}{R^3} \int_0^R \sigma(r) r^2 \mathrm{d}r = 0.1156 \tag{4.4}$$

The blade airfoil section, a NACA 0012, is uniform from root to tip.

The coefficient of rotor lift is prescribed, with $C_L = 0.00926$, making $C_L/\sigma = 0.08$. The rotor is trimmed in pitch and roll. The rotor has no coning, and is tilted nose

down at an angle of attack $\alpha_{\text{shaft}} = -5°$. For the cases presented here, unless otherwise labeled, we assume a tip Mach number of zero (i.e. incompressible flow). All of the following results, including the QP and NLP results, use this baseline rotor. NLP results that include blade chord as an optimization variable will, of course, have different blade planforms and solidities then the baseline, and will be labeled accordingly.

We calculate the minimum power solutions for a range of advance ratios from $\mu = 0.2$ to $\mu = 1.0$, and examine specific optimal controls at two advance ratios: $\mu = 0.4$, which represents the approximate upper limit of advance ratio for most conventional helicopters; and $\mu = 0.8$, to explore the rotor design features that would be required for this rather extreme flight condition.

To analyze these cases, we use the methods described in Chapters 2 and 3 with a lattice of vortex rings containing 18 elements in the spanwise direction and 20 elements in the azimuthal direction for each of the four rotor blades, resulting in a total of 80 elements in the azimuthal direction and 1440 total elements. Because we are analyzing a four bladed rotor, there is a 4/rev periodicity in the problem, and only one-quarter of a revolution of the wake is needed in the computational model. The lattice is spatially periodic, and the wake extends 40 periods (10 complete turns of the rotor) downstream for the near field lifting line analysis, and 40 periods upstream and 40 periods downstream for the far wake induced power analysis.

4.2 Quadratic Programming Results

In this section, we present solutions to the optimal blade control problem for the baseline single rotor with fixed chord, varying radial twist, a quadratic drag polar, and linearized lifting line theory. We maintain $M_{\text{tip}} = 0$ over all advance ratios. Although high Mach numbers do occur on a realistic rotor, particularly on the advancing side, the net effect of accounting for compressibility tends to be small and we

neglect it in this single rotor analysis. The airfoil sectional lift curve slope is equal to 2π, and the quadratic drag polar from Figure 2.3 is used.

Figure 4.1 shows the computed minimum total power with all design variables – including the fixed radial twist distribution – optimized at each advance ratio, together with the induced power and viscous power components that contribute to the total power. Also shown in Figure 4.1 are the results of the optimum circulation analysis, which represents the absolute minimum total power achievable for a rubber rotor. For conventional collective and cyclic control (labeled $N = 1$ in the figure), the power appears to be singular at an advance ratio of $\mu \approx 0.9$. This is consistent with findings by Ormiston [27, 28, 29]. Ormiston found that for a trimmed rotor using conventional controls and constrained by fixed blade geometry (fixed twist, chord, etc.), there is a critical advance ratio less than $\mu = 1$ at which the induced power approaches infinity. This singularity is caused by increasingly negative lift in the reverse flow region with increasing collective that leads to zero net lift sensitivity with collective at the critical advance ratio. Including higher harmonics in the blade pitch control eliminates this singularity, and dramatically improves rotor performance at high advance ratios, a result that can be seen clearly in Figure 4.1. However, higher harmonic control produces measurable but more modest improvements in total power for advance ratios less than about 0.6.

For all levels of harmonic control, the power required for a real rotor is significantly higher that that required for the ideal rubber rotor, especially for advance ratios μ greater than about 0.3. As the number of harmonics included gets large, the minimum power asymptotes to a value significantly larger than that of the rubber rotor, with rapidly diminishing improvement for more than three harmonics. For example, at $\mu = 0.7$, the asymptotic total power is nearly twice that of the optimal baseline rubber rotor. This result is discouraging, but hardly surprising as even with higher harmonic blade pitch control, the radial twist and chord distribution is fixed in

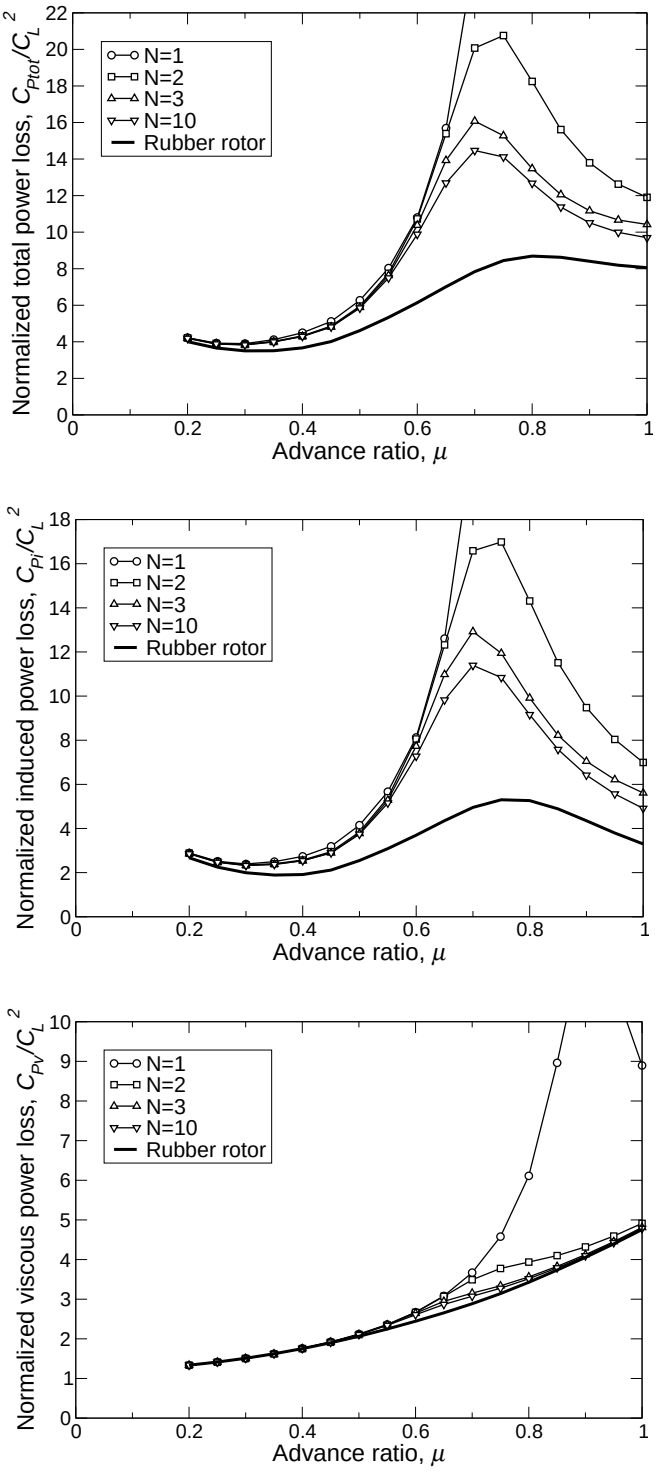

FIGURE 4.1: Top: Minimum power loss for a rotor in trimmed forward flight with varying levels of harmonic control. Middle and bottom: corresponding induced and viscous power components, respectively. All results use the Quadratic Programming method.

azimuth. Thus, not all circulation distributions can be achieved. This suggests that additional significant improvements in performance of a conventional single rotor at high advance ratios will require some sort of spanwise control actuation, e.g., distributed spanwise flaps.

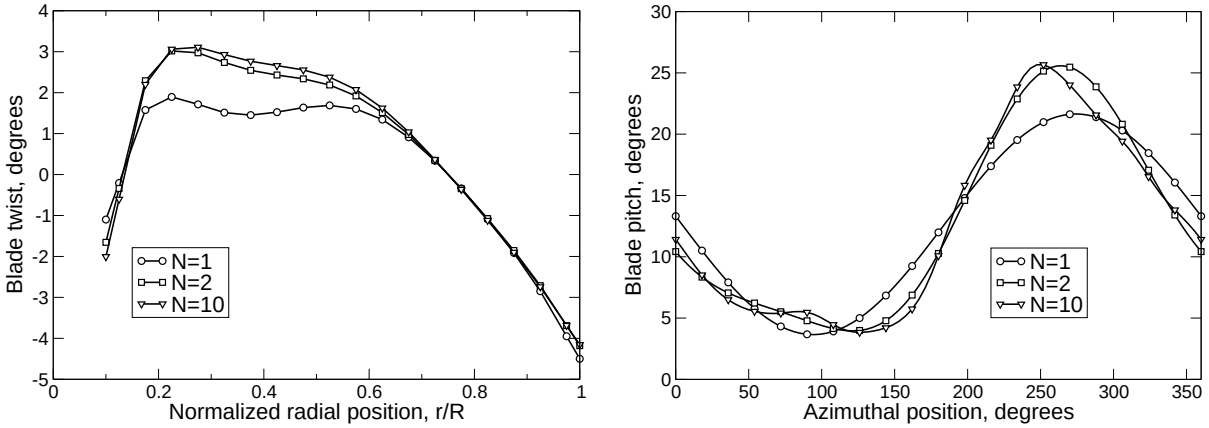

FIGURE 4.2: Optimal radial blade twist distribution (left) and azimuthal blade pitch (right) for a rotor with varying levels of harmonic control, $\mu = 0.4$, as determined by the QP method.

Figure 4.2 shows the optimal blade twist and corresponding azimuthal blade pitch control for minimum total power loss at $\mu = 0.4$, an advance ratio representative of high speed forward flight in conventional helicopters. All levels of harmonic control display a qualitatively similar twist distribution, with nearly identical distributions for N greater than three. Note the washout at the tip, which unloads the blade tip compared to an untwisted blade. This suggests a planform with a reduced chord in the outer portion of the blade may be beneficial.

Figure 4.2 also shows the optimal blade pitch control as a function of azimuth. For the $N = 1$ case – conventional collective and cyclic only – the maximum blade pitch occurs at about $\psi = 270°$, which is consistent with the requirement that the rotor generate adequate lift on the retreating side of the blade to maintain roll trim. Increased levels of harmonic control show a similar overall pattern, but with a slight flattening of the blade pitch control on the advancing side, and a sharpening of the

peak on the retreating side.

Note that the results shown here are the results of a viscous optimization, i.e. minimizing the sum of viscous and induced powers. Because for this example we do not impose a stall constraint, and because the c_{d2} term has a small influence on the optimum solution – see the discussion regarding the generalized Betz criterion, Eq. (2.15) – the control inputs, the circulation distribution, and induced power computed here are nearly identical to what would be computed with a purely inviscid analysis. In other words, the viscous forces change the value of the total power, but do not affect the optimal solution. This would not be true if a stall constraint were imposed or if the planform were allowed to vary, as we shall see in the next section.

4.3 Nonlinear Programming Results

In this section, we present solutions to the nonlinear optimal blade control problem for the baseline conventional rotor configuration, referred to as the NLP solution. The problem is solved using the Newton iteration described in Section 3.4. The full nonlinear problem accounts for a nonlinear lift curve, including stall, a non-quadratic drag polar, and does not assume small induced angles of attack. The analysis is capable of optimizing the chord distribution in addition to other design variables. The blade analyzed here uses a NACA0012 airfoil section from root to tip, with data for the coefficient of lift and drag through the full range of angles of attack obtained from Reference [39].

4.3.1 Comparison of Nonlinear Programming results to Quadratic Programming results

The QP approach is extremely efficient, capable of solving the optimal controls problem for a single advance ratio on the conventional rotor grid in about 3 minutes on a single processor desktop computer, compared to several hours for the Newton

iteration. It is interesting to see how the QP solutions compare to the more computationally expensive (and presumably more accurate) NLP results. To facilitate a direct comparison between the two methods, the chord distribution is not included as a design variable to be optimized in the NLP results, meaning that both the NLP and QP solutions will feature the same rectangular planform.

Figure 4.3 shows the minimum total, induced, and profile power losses for varying levels of blade root harmonic control over a range of advance ratios for a uniform chord distribution, as computed by each approach. The NLP results are shown in red, with the QP results in black. Up to advance ratios of approximately $\mu = 0.4$, the QP method provides a close approximation to the NLP method. However, above this advance ratio, there is a large difference in the NLP and QP results, particularly for the $N = 1$ case. The QP method computes a uniformly lower viscous power than the NLP result across all advance ratios, while the computed induced power is both higher and lower than the NLP result depending on the advance ratio.

This discrepancy in calculated minimum power is a result of how each method treats large angles of attack. The QP method uses a linear lift curve, so a large effective angle of attack will result in an (unrealistically) large sectional coefficient of lift. Additionally, the quadratic approximation used for the drag curve in the QP method severely underpredicts the coefficient of drag at large angles of attack. The NLP method uses realistic lift and drag curves, and as a result more accurately models stall and the resulting large increase in drag. It is therefore not surprising that the QP method computes a lower viscous power compared to the NLP method.

We can attempt to gain further understanding of the discrepancy in induced power, particularly prevalent in the $N = 1$ case, by investigating the optimal circulation distribution computed by each method at $\mu = 0.4$ (see Figure 4.4). The rubber rotor solution shows that a region of high circulation on the retreating side of the rotor is required to generate sufficient lift to maintain roll trim due to the

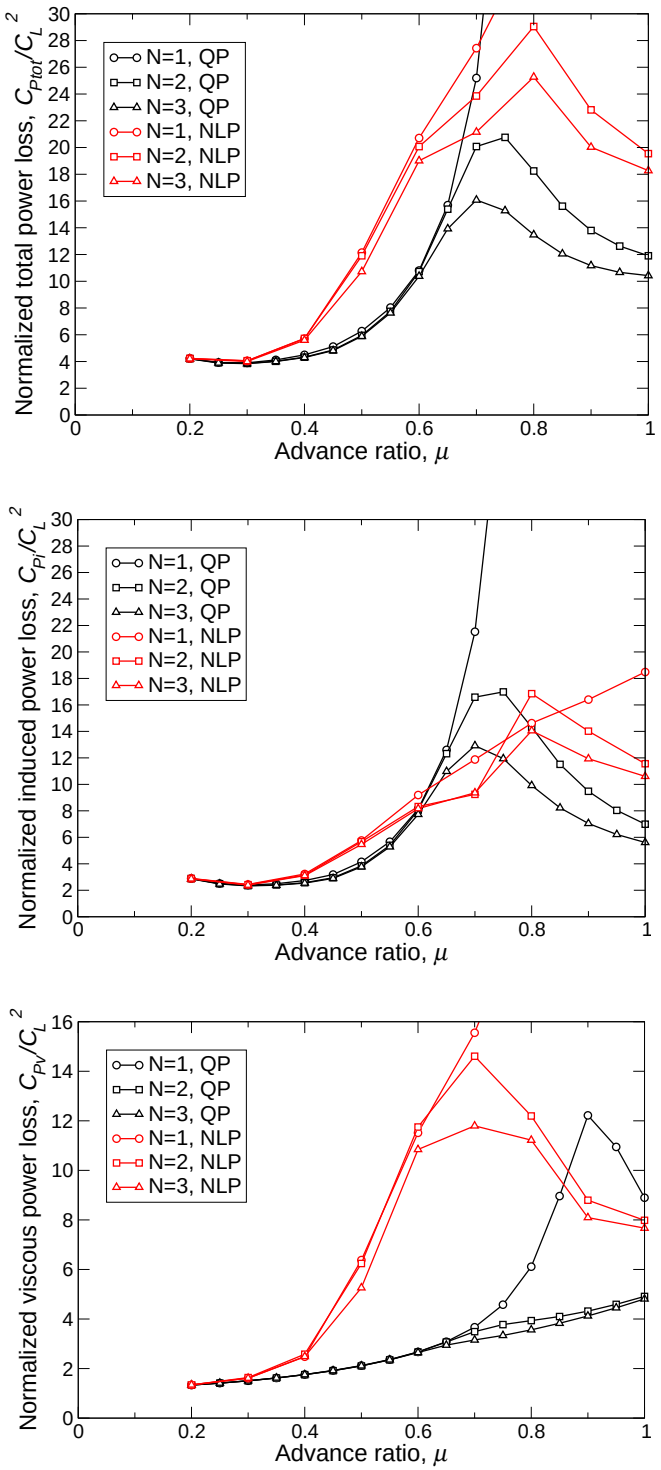

FIGURE 4.3: Top: Minimum power loss for a rotor with uniform chord distribution, as computed by the Quadratic Programming and Nonlinear Programming methods. Middle and bottom: corresponding induced and viscous power components, respectively.

low dynamic pressure in this region. Generating this large circulation requires large effective angles of attack over a significant portion of the retreating side of the rotor, particularly in the reverse flow region ($\psi = 225°$ to $\psi = 315°$, and at normalized radial positions less than ≈ 0.4 in this case), where the blade sees large and rapidly changing geometric angles of attack. The difference in the QP and NLP computed circulation distributions is primarily located in this reverse flow region. However, as we see in Figure 4.6, the $\mu = 0.4$ radial twist and pitch input shown are quite similar (though not identical) between the two methods, indicating that the two methods have a very similar effective angles of attack at all locations in the wake. In the reverse flow region, the assumption of a linear lift curve used in the QP method results in a moderate, positive circulation, while the NLP solution has areas of zero or negative circulation within this region. These differences in circulation result in different induced powers for the two solutions.

At higher advance ratios, it becomes increasingly difficult to efficiently maintain roll trim with $N = 1$ control, as investigated by Ormiston [27, 28, 29] and evidenced by the rapid rise in induced power in both the the QP and NLP cases at advance ratios above $\mu = 0.6$. At these advance ratios, the QP solution is actually penalized by its use of a linear lift curve, as the increasingly large cyclic pitch required at $\Psi = 270$ to maintain roll trim, shown in the bottom right plot of Figure 4.6, results in large portions of the wake with very large magnitudes of circulation, resulting in high induced power. The QP solution attempts to mitigate this by using a significantly different radial twist distribution for the $N = 1$ solution, featuring a large positive twist gradient from the root out to a normalized position of about 0.4. The differences between the two solutions is further illustrated in Figure 4.5, which shows the NLP, QP, and rubber rotor optimal circulation distributions at $\mu = 0.8$. The QP solution contains large levels of circulation throughout the wake, while the NLP and rubber rotor solutions have significantly lower of values of circulation at all points. In this

case, the NLP solution benefits from the fact that its sectional coefficient of lift is limited by stall, avoiding regions of excessively high circulation in the wake and resulting in a lower induced power.

With the additional degrees of freedom available with $N = 2$ or $N = 3$ control, the QP solution maintains trim without resorting to these excessively high angles of attack, and the induced powers between the NLP and QP solutions are in better (though still not perfect) agreement.

In summary, at low advance ratios ($\mu < 0.4$), the results of the QP and NLP methods are in fairly good agreement for the single rotor. The difference between the QP and NLP results at high advance ratios is a result of the single rotor configuration requiring very high coefficients of lift on the retreating side of the rotor. This leads to azimuthal pitch inputs that feature large pitch angles and post-stall effective angles of attack. The difference in how the two methods computes the coefficient of lift, and ultimately circulation due to these large effective angles of attack, results in the large differences in the power calculated by the two methods.

In a coaxial or wing-rotor configuration, maintaining trim at high advance ratios does not require large root pitch inputs on the retreating side of the rotors. In fact, the optimal solution for these configurations involves minimizing circulation and lift in reverse flow regions. As a result, the QP and NLP results are in much better agreement for these configurations, as we will see in Chapters 5 and 6. Additionally, for a conventional rotor, the trends in total power with regard to increasing levels of harmonic control are similar between the two methods, indicating that the QP approach still provides some useful insight to the conventional rotor optimal control problem at high advance ratios.

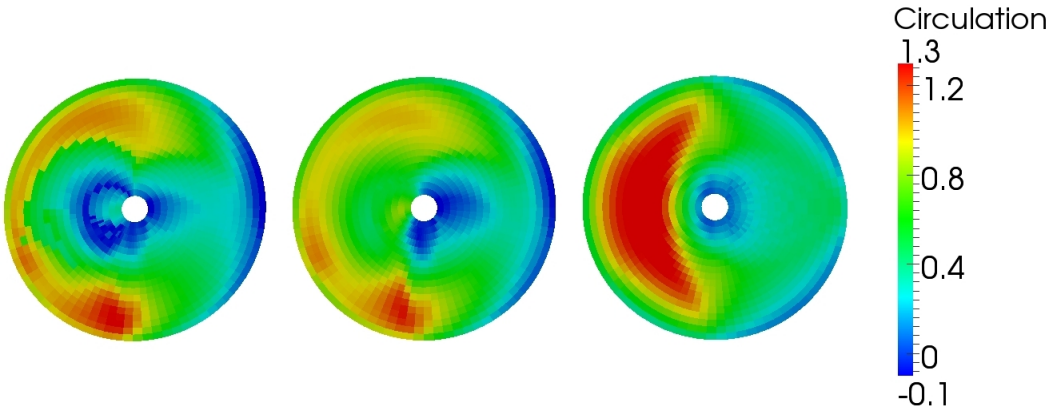

FIGURE 4.4: Optimal circulation distribution for a rotor at $\mu = 0.4$. From left to right: NLP result and QP result with $N = 1$ root control, and rubber rotor solution.

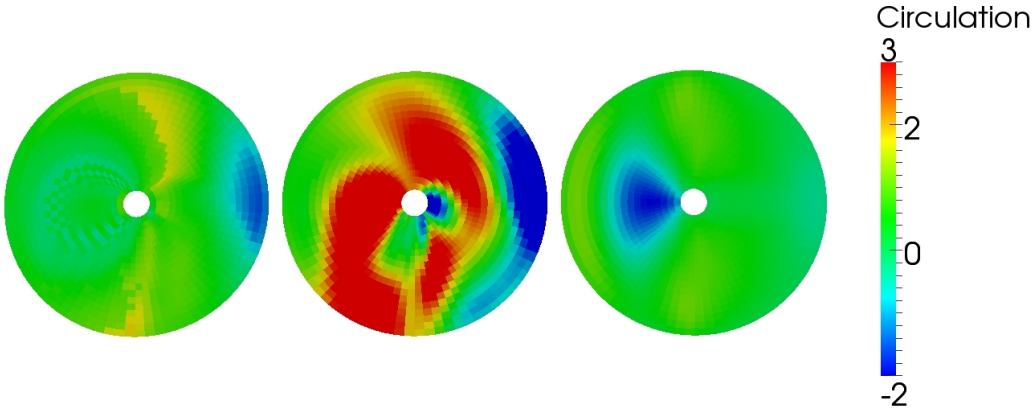

FIGURE 4.5: Optimal circulation distribution for a conventional rotor at $\mu = 0.8$. From left to right: NLP result and QP result with $N = 1$ root control, and rubber rotor solution.

4.3.2 Nonlinear Programming Results with Optimized Chord

The NLP results shown above account for realistic lift and drag curves and are therefore more accurate than the QP results. All of the preceeding results use the baseline chord distribution, which is a rectangular planform with a thrust weighted solidity $\sigma_{TW} = 0.1156$. In this section, we include the chord distribution as a design variable to be optimized, allowing the optimization algorithm to select the planform,

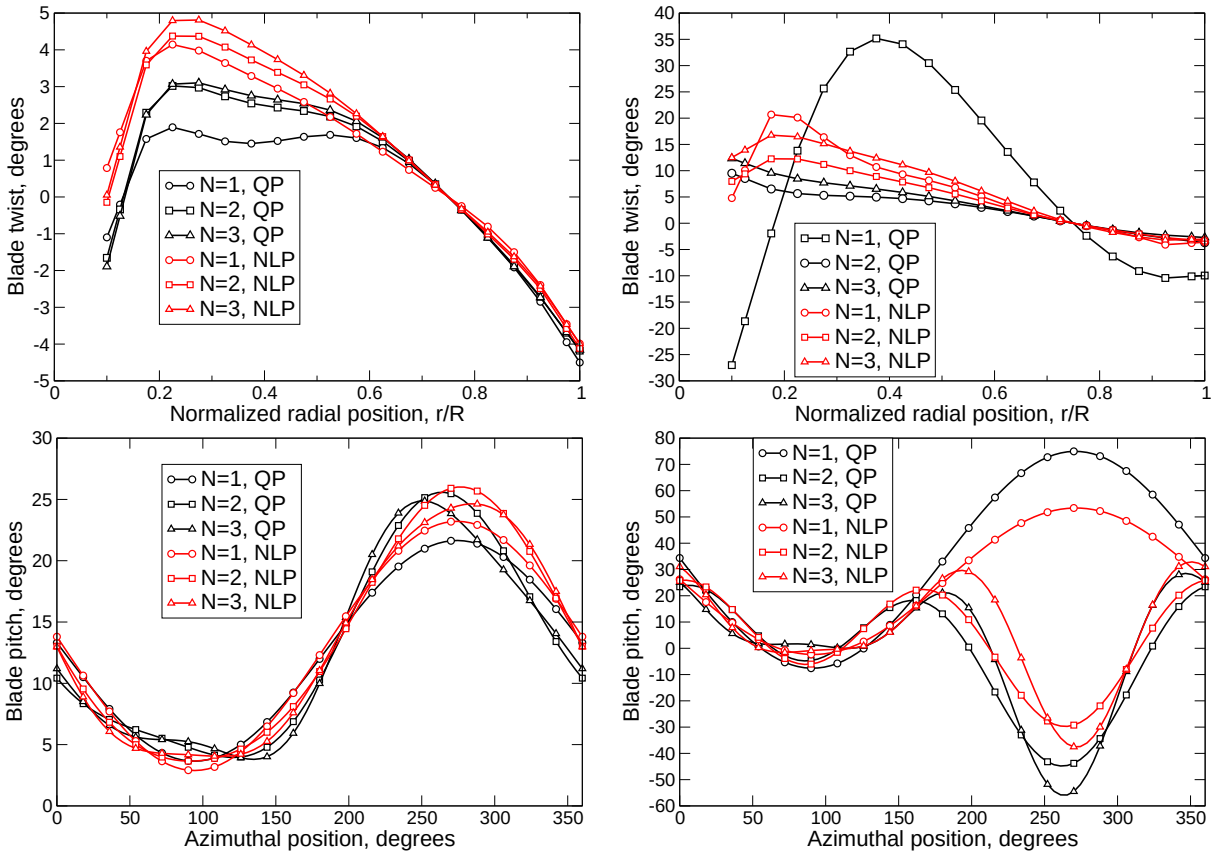

FIGURE 4.6: Left: Optimal radial and azimuthal distributions of blade twist and pitch for a conventional rotor at $\mu = 0.4$, calculated by the QP and NLP methods Right: Optimal radial and azimuthal distributions of blade twist and pitch for a conventional rotor at $\mu = 0.8$, calculated by the QP and NLP methods.

in addition to radial blade twist and root pitch input, that minimizes total power.

Figure 4.7 shows the minimum total power for a rotor using an optimized chord distribution, compared to the uniform chord case. Also plotted is the minimum power for a rotor using the baseline uniform chord distribution and an untwisted blade, with only the root pitch inputs varied to maintain trim and achieve the required lift. This case serves as a benchmark of performance for a single rotor and is a useful comparison to show the improvements possible through blade twist and chord design. Note that all design variables are optimized at each advance ratio, including the chord distribution. In other words, each data point represents the minimum total

power for a single point optimization at that specific advance ratio.

The optimized chord case achieves modest reductions in power at advance ratios below $\mu = 0.4$. Above this advance ratio, optimizing the chord results in large reductions in power compared to the uniform chord case for all levels of harmonic control. At $\mu = 0.8$, the total power for the $N = 1$ case is reduced by 17% with the use of an optimized chord distribution. Additionally, higher harmonic control improves the performance among the optimized chord rotors, with $N = 3$ control providing a 25% decrease in power relative to the $N = 1$ case. Of course, even with higher harmonic control and a chord and twist distribution optimized only for fast forward flight, the power requirements are still very high. The $N = 3$ optimized chord case at $\mu = 0.8$, which represents a value close to the lowest achievable power with any blade root control scheme, corresponds to a lift over effective drag value below 4, which is still low relative to a fixed wing aircraft or the compound configurations we will see in the following sections.

Figure 4.8 shows the radial twist and azimuthal pitch distribution for the optimized chord case compared to the uniform chord case at an advance ratio of $\mu = 0.4$. Figure 4.9 shows the corresponding planform for the $N = 1$ and $N = 3$ optimized chord cases. The optimal planform features a very unusual shape, with an extremely small chord on its inner portion, a maximum chord at a normalized radial position of 0.6, and then a rapid taper extending to the tip. The largest chord is nearly twice as large as the baseline chord distribution. The thrust weighted solidity of the optimal rotor is $\sigma_{\mathrm{TW}} = 0.132$, compared to $\sigma_{\mathrm{TW}} = 0.116$ for the baseline rotor. It is somewhat surprising that the optimal viscous rotor planform has a *higher* solidity and larger wetted surface area than the baseline constant chord case, which results in higher viscous power. But in fact, at this advance ratio, the variable chord rotor shape significantly reduces induced losses, more than the attendant increase in viscous power. The influence of induced power on the solution will be explored further

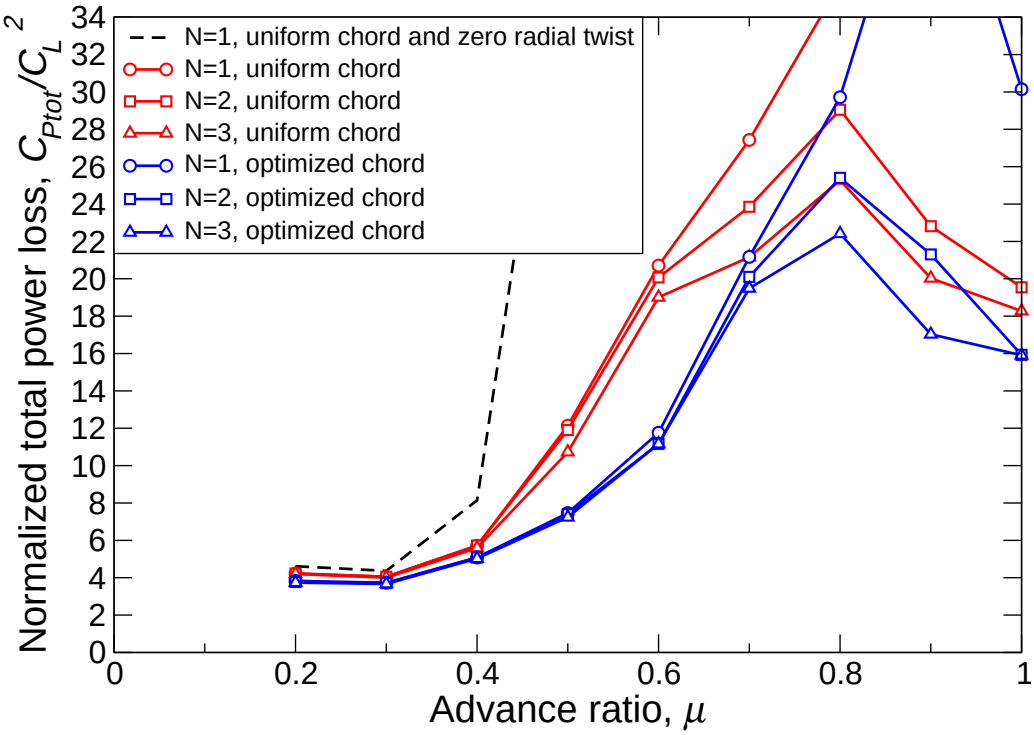

FIGURE 4.7: Minimum power loss for a conventional rotor with chord optimized compared to a uniform chord case and a uniform chord and uniform twist case.

in the following section.

Lastly, Figure 4.10 shows the radial twist and azimuthal pitch distribution for the optimized chord conventional rotor case at an advance ratio of $\mu = 0.8$; Figure 4.11 shows the corresponding planforms. This is a fairly extreme flight condition, and is not realistically attainable by conventional rotors. It is interesting, however, to see the controls required to maintain trim at this high advance ratio. The $N = 3$ optimized chord case has a signficantly different root pitch input in the region from $\psi = 200°$ to $\psi = 330°$ than the uniform chord case, although both achieve a similar final effective angle of attack, albeit with the blade traversing through the flow in the opposite direction, i.e. rotated by 180°. The solidities of the optimal blades are smaller at this high speed flight condition than in the $\mu = 0.4$ case, as higher dynamic pressures further penalize the large viscous drag resulting from a large

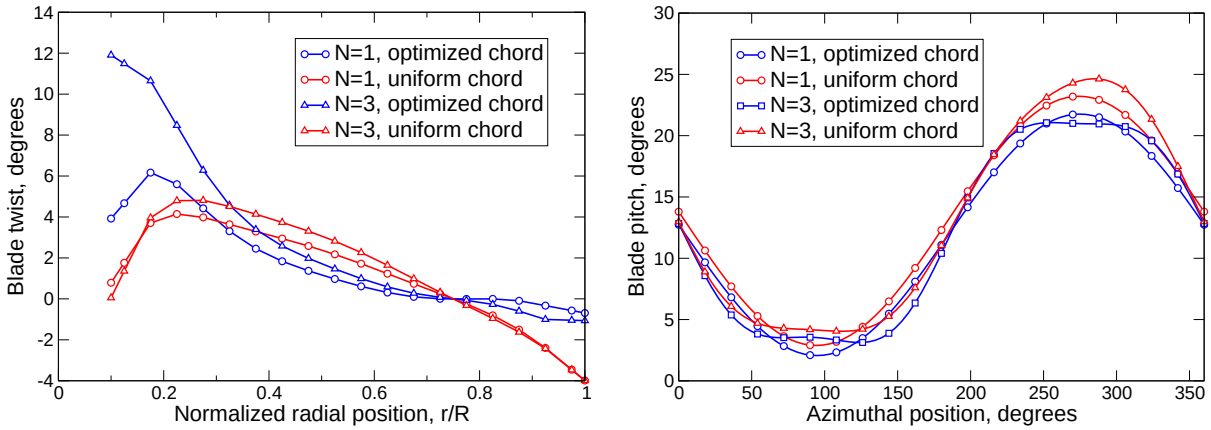

FIGURE 4.8: Optimal radial and azimuthal distributions of blade twist and pitch for a rotor with and without an optimized chord distribution, at $\mu = 0.4$.

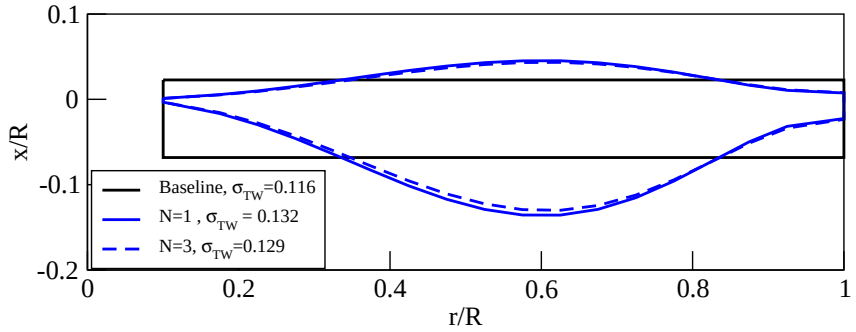

FIGURE 4.9: Optimal blade planform at $\mu = 0.4$ for varying levels of harmonic control.

chord. Additionally, the $N = 1$ and $N = 3$ cases now have fundamentally different planforms, with the majority of the blade area for the $N = 1$ case located near the tip of the blade. The $N = 3$ case results in a more symmetric blade, with the largest chord located approximately at midspan and without the excessively small root chord values seen in the $N = 1$ case.

Figures 4.12 and 4.13 show the optimal circulation distribution and force distribution, respectively, for the optimized chord cases. The solutions for the $N = 1$ case and the $N = 3$ case are shown, along with the rubber rotor solution. It is interesting to note that at this high speed flight condition, nearly all of the lift is being generated at the fore and aft positions of the rotor. This is a result of a ma-

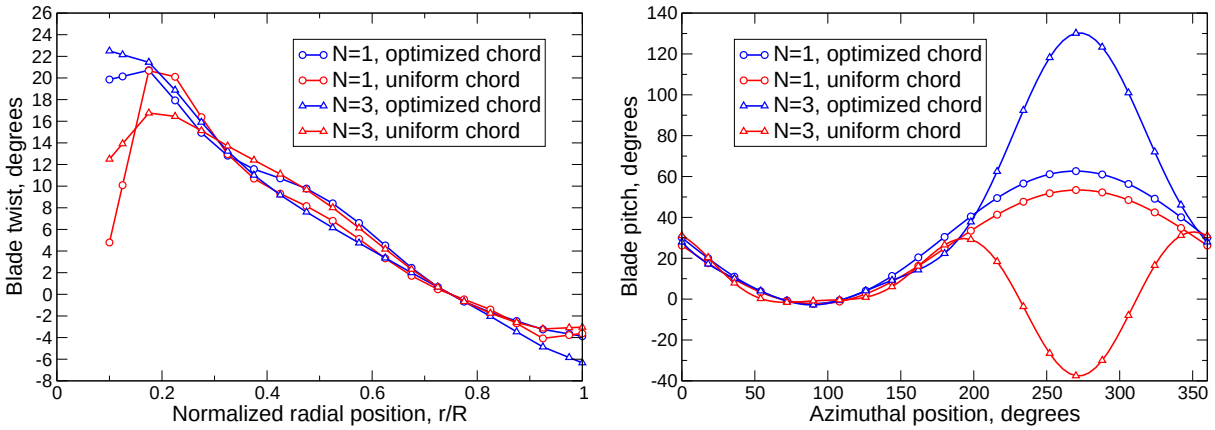

FIGURE 4.10: Optimal radial and azimuthal distributions of blade twist and pitch for a conventional rotor with and without an optimized chord distribution, at $\mu = 0.8$.

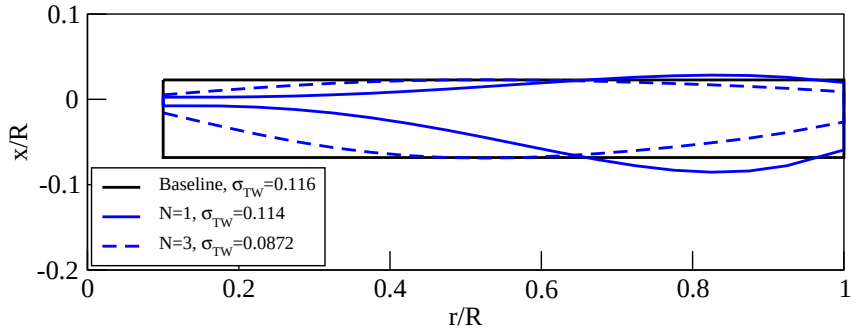

FIGURE 4.11: Optimal blade planform at $\mu = 0.8$ for varying levels of harmonic control.

jority of the retreating wake having a low dynamic pressure, making it incapable of generating significant lift. As a result, the advancing side must be almost entirely offloaded to maintain roll trim. The force distribution is still skewed slightly towards the advancing side, which must be balanced by a region of negative force at $\psi = 90°$ in the $N = 1$ and $N = 3$ cases, leading to minimum powers much higher than the rubber rotor optimal. The $N = 3$ case more closely matches the rubber rotor result by decreasing the magnitude of the circulation at $\psi = 0°$ and $\psi = 180°$ and generating a region of negative circulation in the reverse flow region between $\psi = 270°$ and $\psi = 330°$.

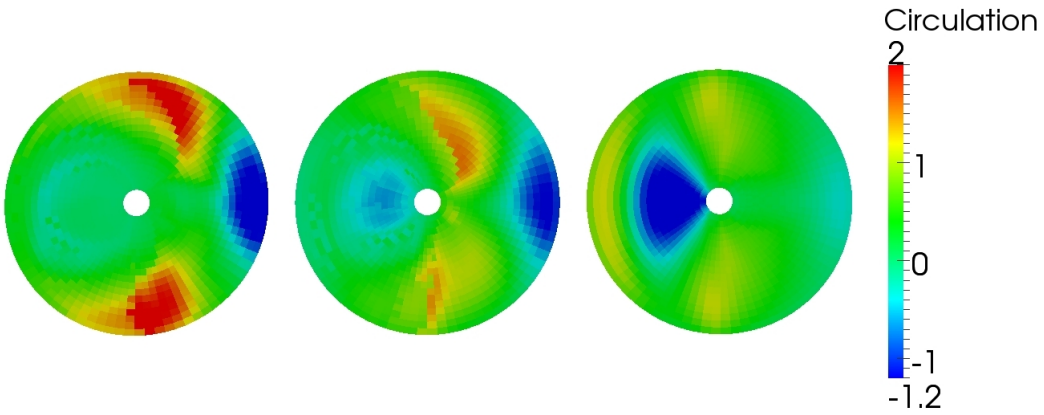

FIGURE 4.12: Optimal circulation distribution for a rotor with optimized chord at $\mu = 0.8$. From left to right: $N = 1$ control, $N = 3$ control, and rubber rotor solution.

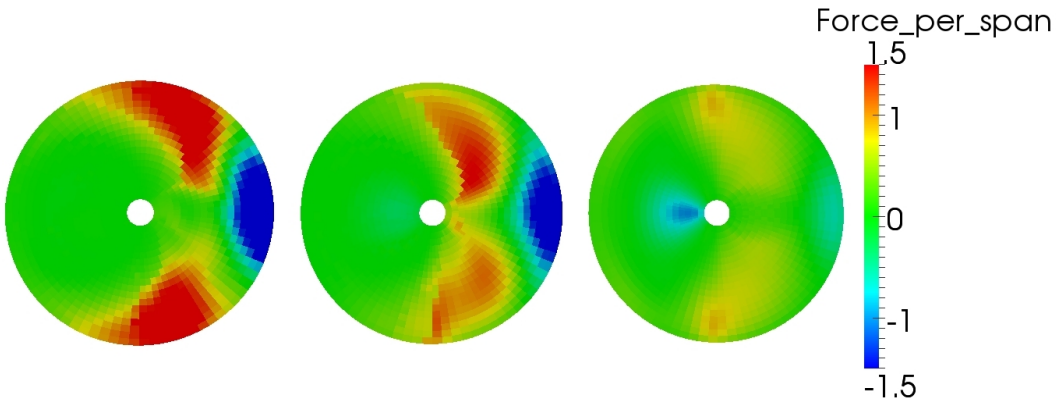

FIGURE 4.13: Optimal force per span distribution for a rotor with optimized chord at $\mu = 0.8$. From left to right: $N = 1$ control, $N = 3$ control, and rubber rotor solution.

4.3.3 Comparison of Viscous Optimum to Inviscid Optimum

The previous sections showed the results of viscous optimizations, or optimizations that sought to minimize the sum of induced and viscous power. It is interesting to examine the inviscid solution, which minimizes only induced power, to see how it compares to the viscous solution. First, Table 4.1 shows a comparison of the inviscid and viscous minimum powers at $\mu = 0.4$ using $N = 1$ and $N = 3$ control. Note that although the inviscid optimizations were performed without regard to viscous

power, a viscous power associated with the optimal solution can still be computed. As expected, for both $N = 1$ and $N = 3$ control, the inviscid optimum has a lower induced power (C_{Pi}/C_L^2), than the viscous optimum (of course this has to be the case, or the viscous optimum would in fact be the inviscid optimum). Similarly, the viscous optimum has a lower total power than the inviscid case. It is interesting to note that the induced power for the viscous optimizations is very close (within about 10%) to the induced minimum power. The viscous solution is able to trade some of this induced power for further decreases in viscous power, resulting in a lower total power. Also of interest, the lower total power associated with $N = 3$ control is entirely a result of reductions in induced power, as the viscous powers of the $N = 1$ and $N = 3$ cases are identical. More generally, the $N = 3$ case is only slightly better than the $N = 1$ case for the viscous analysis.

Table 4.1: Induced, viscous, and total power at $\mu = 0.4$ for inviscid and viscous optimal solutions of single rotor.

	N=1		N=3	
	Inviscid design	Viscous design	Inviscid design	Viscous design
Induced power, C_{Pi}/C_L^2	2.52	2.68	2.35	2.62
Viscous power, C_{Pv}/C_L^2	2.97	2.40	3.17	2.40
Total power, C_{Ptot}/C_L^2	5.49	5.08	5.52	5.03

The optimal circulation distribution for each solution is shown in Figure 4.14. The two distinct optimizations have a nearly identical circulation distribution, reinforcing the fact that induced losses are a significant driver in the total power optimum, even in cases featuring an optimized chord. Figure 4.15 shows the inviscid versus viscous radial twist and azimuthal pitch input for $\mu = 0.4$. Both the inviscid and viscous solutions are very similar.

The effect of induced losses on optimal planform shape can be seen by examining

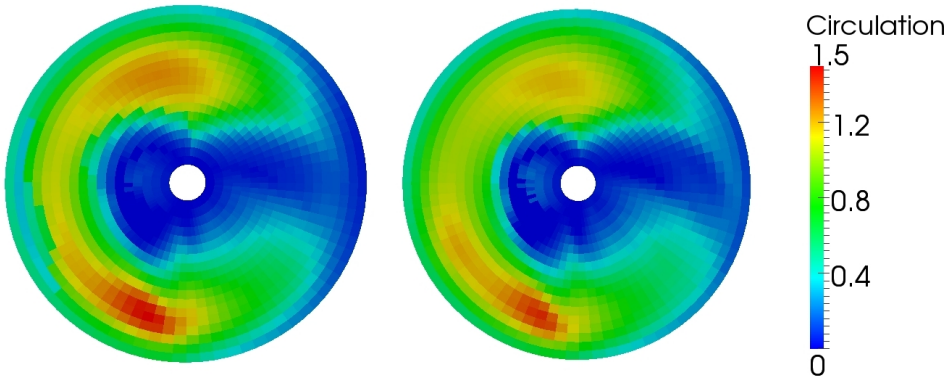

FIGURE 4.14: Optimal circulation distribution for a rotor with $N = 1$ control and an optimized chord distribution at $\mu = 0.4$. Left: Viscous solution. Right: Inviscid solution.

the optimal inviscid rotor planform shown in Figure 4.16. Note that for the inviscid case, the planform has the same general shape, but with a slightly higher solidity. The optimized viscous planform, as one might expect, has a slightly smaller wetted surface area than the inviscid case, although as discussed previously, it is still larger than the baseline rotor.

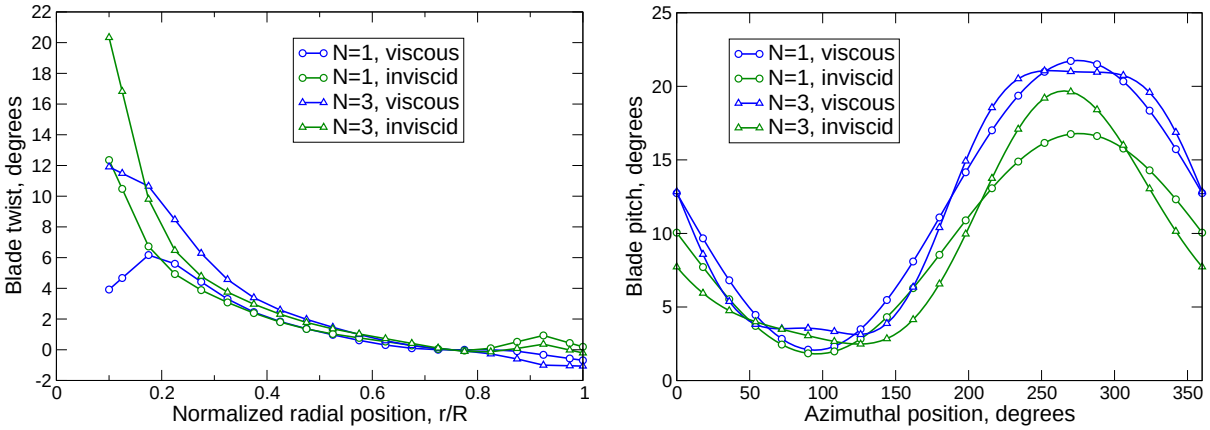

FIGURE 4.15: Comparison of inviscid and viscous radial and azimuthal distributions of blade twist and pitch for a rotor using $N = 1$ and $N = 3$ control at $\mu = 0.4$

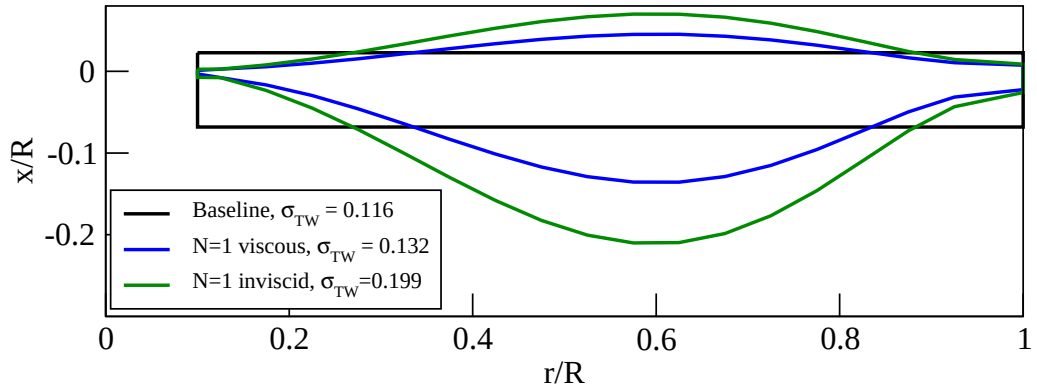

FIGURE 4.16: Comparison of inviscid and viscous optimal planforms at $\mu = 0.4$ for a rotor using $N = 1$ control.

4.4 Conclusions from Analysis of a Conventional rotor

Based on the analysis of a conventional rotor using higher harmonic control in this chapter, we can draw the following specific conclusions

1. The quadratic programming method is computationally fast, requiring only several minutes of CPU time on a desktop computer for each flight condition. At advance ratios below about $\mu = 0.4$, the quadratic programming method produces a solution that is very close to the more accurate nonlinear programming method. At advance ratios above $\mu = 0.4$, the two methods arrive at similar radial twist and azimuthal pitch solutions, but compute significantly different induced, viscous and total powers. This is a result of the large effective angles of attack required on the retreating side of the rotor to maintain roll trim.

2. Despite the differences in the results at high advance ratios, the general trends with respect to advance ratio, level of harmonic control, and basic radial and azimuthal pitch inputs are similar between the QP and NLP methods, indicating that the QP method is still of use in the analysis of a single rotor despite its simplifying assumptions. Additionally, at advance ratios below $\mu = 0.4$, the

QP and NLP methods are in close agreement.

3. For the uniform chord case, the use of higher harmonic control produces large decreases in total power, with $N = 2$ and $N = 3$ control offering reductions of 19% and 42%, respectively, compared to $N = 1$ control at $\mu = 0.8$. At lower advance ratios typical of a conventional rotor, the reduction in power is more modest, on the order of 2%.

4. Use of an optimized chord distribution also provides large reductions in power at both low and high advance ratios. For $N = 1$ control, use of an optimized chord distribution results in an 11% reduction in total power at $\mu = 0.4$ and a 17% reduction in total power at $\mu = 0.8$. The optimal planform in the $\mu = 0.4$ case has a higher solidity than the baseline rotor, with a large chord near the midspan of the blade which tapers towards the root and tip.

5. Higher harmonic control is effective in reducing power at high advance ratios when used in conjuction with an optimized chord distribution. For example, use of $N = 3$ control with optimized chord provides a 25% reduction in power compared to the $N = 1$ optimized chord case at $\mu = 0.8$.

6. The viscous minimum power solution is driven by induced losses, as the optimal inviscid and viscous circulation distributions and radial twist and azimuthal pitch inputs are very similar. This fact is supported by both the theory (the generalized Betz criterion) and the numerical results.

5

Coaxial Rotor Results

In this chapter, we analyze the optimal performance of a coaxial, counter-rotating rotor system. The contour plots displayed in this chapter will include representations of both the upper and lower rotor in body-fixed coordinates. In all contour plots, the vehicle is traveling up the page, with the upper rotor rotating counter-clockwise and the lower rotor rotating clockwise. As a result, the advancing side is the right half of the upper rotor and the left half of the lower rotor.

5.1 Baseline Rotor

The parameters selected for this configuration were meant to closely resemble the Sikorsky X2 Technology Demonstrator, shown in Figure 1.4.

We consider a system of two coaxial counterrotating rotors. We analyze rotors similar to the design intent of the X2 rotor system in high speed cruise as described by Bagai [5]. The design intent advance ratio, μ, is 0.85; the thrust weighted solidity, σ_{TW}, is 0.1441, and the modified thrust weighted solidity as defined in Equation 3.64, σ_{TWM}, is 0.116; the coefficient of lift, C_L, is 0.02324 corresponding to a C_L/σ_{TW} of 0.1613; and the relative tip Mach number is 0.9. The rotors have no coning, and the

shaft is tilted nose down at an angle of $\alpha_{\text{shaft}} = -5°$. We use a root cutout equal to 10 percent of the rotor radius, with a vertical spacing between the rotors equal to 20 percent of the rotor radius. Both the upper and lower rotors are constrained to use the same fixed radial blade twist and chord; however, each rotor has its own set of root pitch inputs.

In all cases, we require the total rotor system to be in moment trim; the moments on an individual rotor may be nonzero as long as the net moment is zero, requiring that the rotors be rigid. As a result, each rotor will carry an offset lift on the advancing side of the rotor.

To analyze these cases, we use the methods described in Chapters 2 and 3 with a lattice of vortex rings containing 18 elements in the spanwise direction and 15 elements in the azimuthal direction for each of the eight rotor blades, for a total of 2160 vortex ring elements.

5.2 Quadratic Programming Results

In this section, we present solutions to the optimal blade control problem for the baseline rotor with fixed chord, varying radial twist, a quadratic drag polar, and linearized lifting line theory. We assume a uniform chord that gives the modified thrust weighted solidity of the X2 design. Although the relative tip Mach number of the X2 design varies from approximately 0.65 to 0.9 over the range of advance ratios from 0.2 to 1.0 [5], for simplicity we maintain $M_{\text{tip}} = 0.9$ over all advance ratios. Although Mach number has some effect on the optimal controls, it has a minimal effect on power requirements, and the simplification of a uniform M_{tip} does not result in large changes in the optimal solution. The airfoil sectional lift curve slope is equal to 2π, and the NACA 0012 quadratic drag polar shown in Figure 2.3 is used.

Figure 5.1 shows the computed minimum total, induced, and profile power losses for varying levels of blade root harmonic control over a range of advance ratios. At

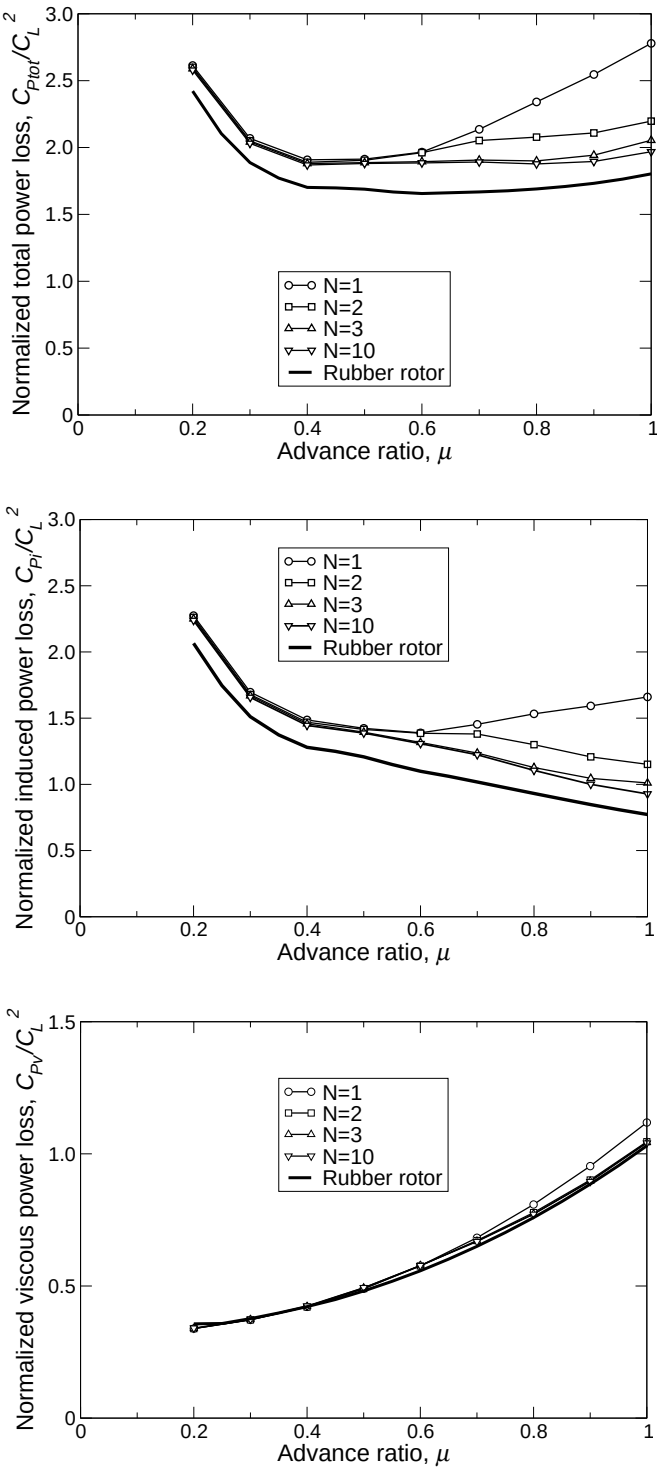

FIGURE 5.1: Top: Minimum power loss for a coaxial rotor in trimmed forward flight with varying levels of blade root harmonic control. Middle and bottom: corresponding induced and viscous power components, respectively. All results use the Quadratic Programming method.

each advance ratio, all design variables, including the fixed radial twist, are optimized. Also shown is the rubber rotor minimum power, i.e. the absolute minimum power achievable within this rotor configuration assuming infinite degrees of freedom in blade articulation. For advance ratios less than about 0.5, higher harmonic control does not provide a significant reduction in power. For higher advance ratios, however, the total power required is dramatically reduced with diminishing returns for N greater than three. At the design advance ratio of $\mu = 0.85$, higher harmonic control can reduce the total power required by about 20%. As in the single rotor case, the minimum power solution does not asymptote to the rubber rotor optimum, even with high levels of blade root harmonic control, because of the lack of radial twist control as a function of azimuth. Furthermore, almost all of the decrease in total power is a result of improvements in the induced power of the rotor. The viscous power losses are nearly identical for all levels of harmonic control.

Figure 5.2 shows the optimal fixed blade twist at advance ratios of $\mu = 0.5$ and $\mu = 0.85$ for varying levels of harmonic control. Also shown is the blade pitch control as a function of azimuth. The azimuthal angle is positive in the direction of each of the rotors' rotation, so here azimuth represents advancing time. The blade pitch is nearly the same for the upper and lower rotors, with a slight asymmetry caused by the -5° tilt of the shaft.

For the $\mu = 0.85$ case, note the very interesting azimuthal variation of blade root pitch in both the $N = 2$ and $N = 10$ higher harmonic control schemes. The twist is abruptly reduced by about 25 degrees at $\psi \approx 225^\circ$, with a corresponding increase at $\psi \approx 310^\circ$. This dropoff in pitch angle takes place in the portion of the rotor disk where the blade enters and exits the reverse flow region. To understand this behavior, the optimal circulation on the rotor disk for $N = 1$ and $N = 10$ is plotted in Figure 5.3, and also for the rubber rotor. Note that the $N = 1$ solution has a region of positive circulation on the retreating sides of the upper and lower rotors, a

feature not present in the rubber rotor. The circulation in this region is dramatically reduced in the $N = 10$ solution by reducing the pitch of the blade as it sweeps through this region, resulting in lower induced and total power. The $N = 1$ control scheme does not have the level of azimuthal control necessary to achieve this abrupt reduction in pitch, and instead compensates by using a significantly decreased level of fixed blade twist on the inboard portion of the blade, a method not as effective at mitigating the circulation in the reverse flow region, leading to the $N = 1$ case having significantly higher induced and total powers than the $N = 2$ and higher cases.

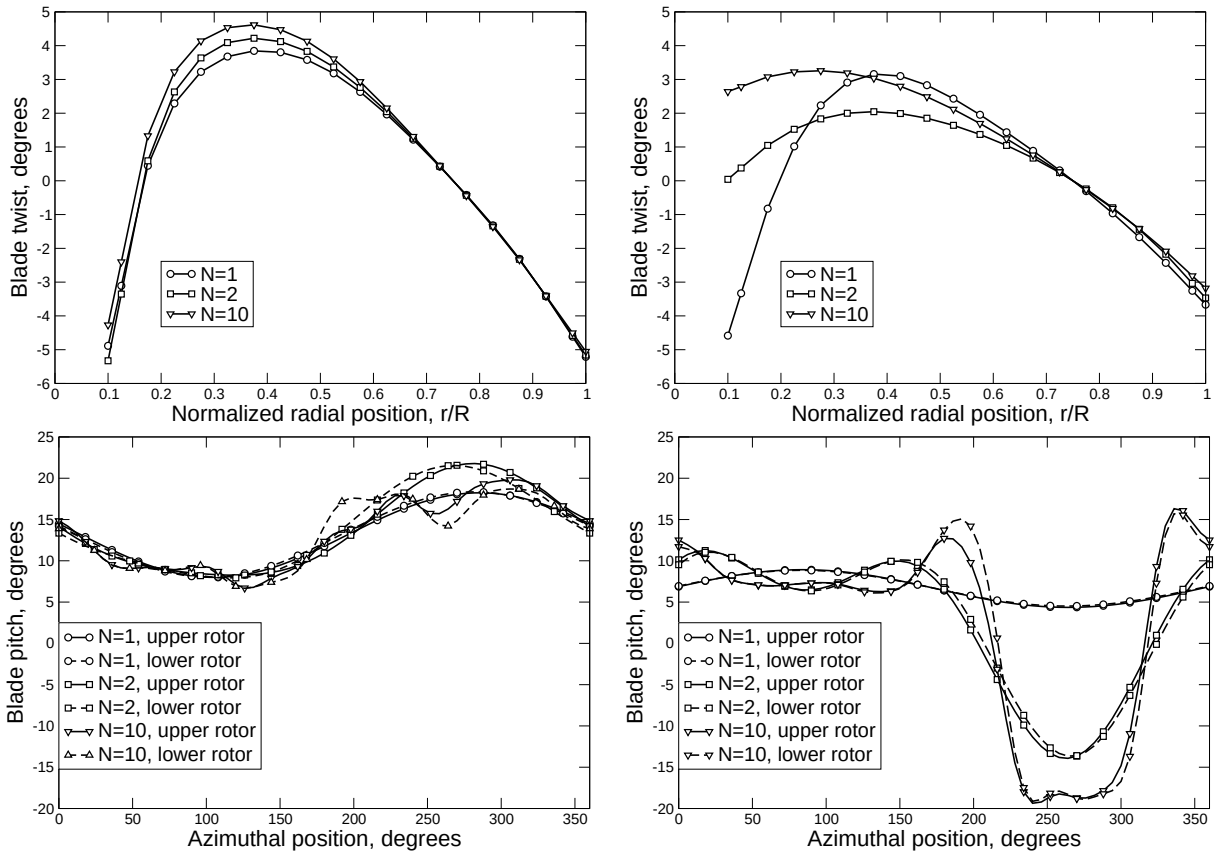

FIGURE 5.2: Left: Optimal radial and azimuthal distributions of blade twist and pitch for coaxial rotors at $\mu = 0.5$. Right: Optimal radial and azimuthal distributions of blade twist and pitch for coaxial rotors at $\mu = 0.85$.

Figure 5.4 shows the optimal force per span distribution on the rotor. For both

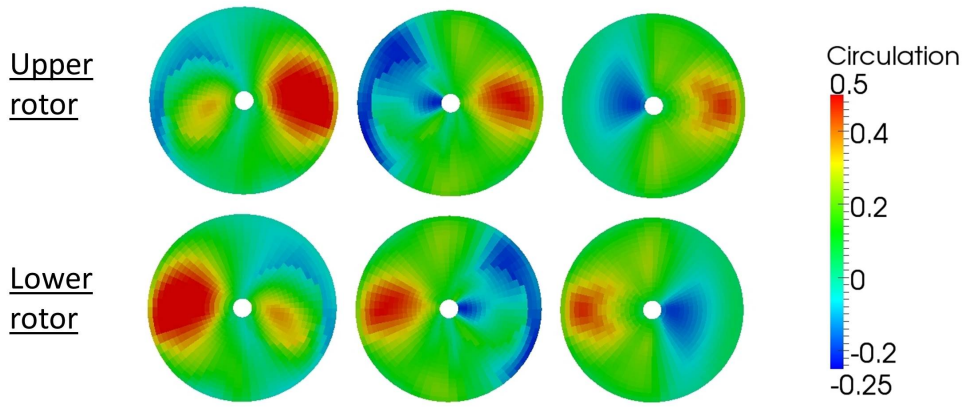

FIGURE 5.3: Optimal circulation distribution on upper and lower rotors of a coaxial system at $\mu = 0.85$, computed by QP method. Left: $N = 1$ control. Middle: $N = 10$ control. Right: Rubber rotor.

$N = 1$ and $N = 10$ control and the rubber rotor case, nearly all of the force is generated on the advancing side of the rotor, where dynamic pressures are high, allowing much of the retreating blade to be offloaded. The region of positive circulation on the retreating side of the $N = 1$ solution results in a small region of force on the retreating side, a feature that adds to the total power and is not seen in the $N = 10$ and rubber rotor solutions.

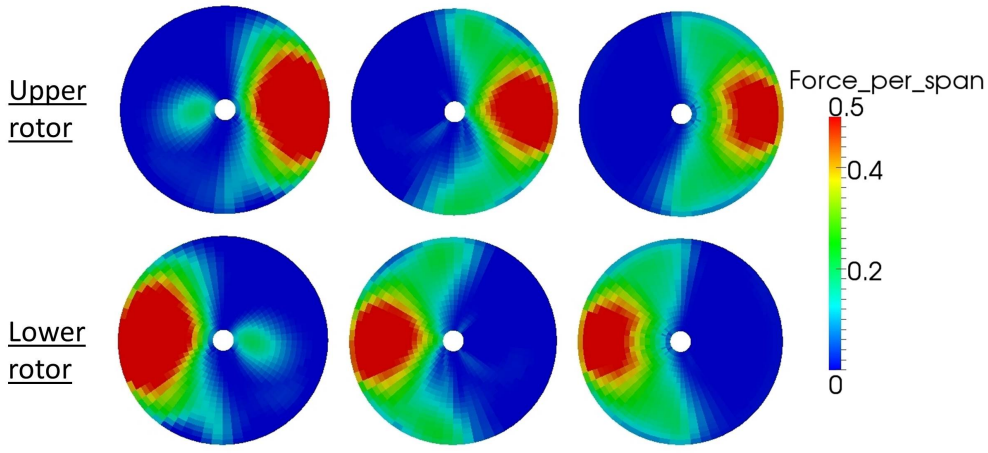

FIGURE 5.4: Optimal force distribution on upper and lower rotors of a coaxial system at $\mu = 0.85$, computed by QP method. Left: $N = 1$ control. Middle: $N = 10$ control. Right: Rubber rotor.

The $\mu = 0.5$ optimal controls are fundamentally different than the $\mu = 0.85$ case. The optimal fixed blade twist for each level of harmonic control features a large positive gradient on the inboard portion of the blade. The pitch inputs, even for the $N = 10$ case, no longer exhibits the large decrease in pitch angle in the reverse flow region, but rather a steady increase in pitch over this region that closely mirrors the $N = 1$ input. Figure 5.5 shows the optimal circulation for the $N = 1$, $N = 10$, and rubber rotor solutions at $\mu = 0.5$. The $N = 1$ case now closely resembles the $N = 10$ and rubber rotor cases, again showing that the large decrease in pitch on the retreating side of the rotor is no longer required to achieve a circulation distribution similar to the rubber rotor optimum at this lower advance ratio. As a result, use of $N = 2$ or higher control systems does not yield significant power decreases over $N = 1$ control at advance ratios at or below $\mu = 0.5$, and the high positive inboard twist gradient seen in the $N = 1$ case at $\mu = 0.85$ produces the minimum power solution.

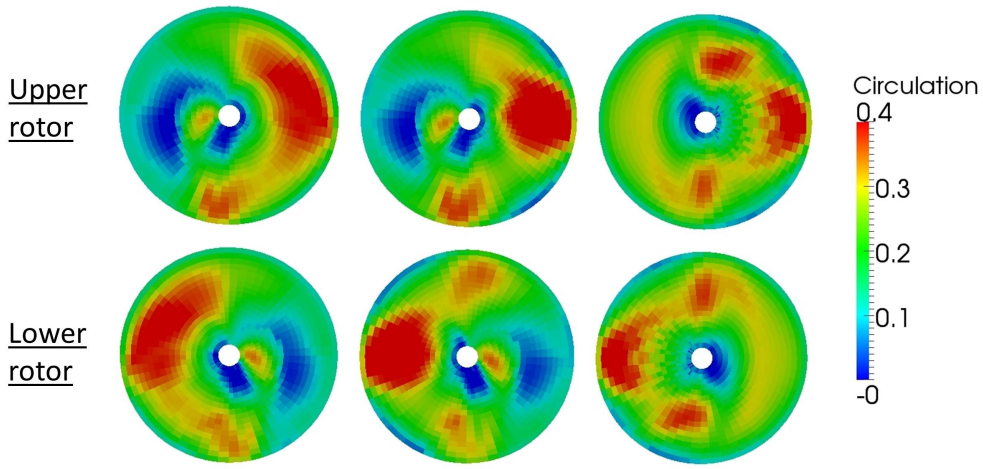

FIGURE 5.5: Optimal circulation distribution on upper and lower rotors of a coaxial system at $\mu = 0.5$, computed by QP method. Left: $N = 1$ control. Middle: $N = 10$ control. Right: Rubber rotor.

5.3 Nonlinear Programming Results

In this section, we present solutions to the nonlinear optimal blade control problem for the baseline coaxial configuration. The full nonlinear problem accounts for a nonlinear lift curve, including stall, a non-quadratic drag polar, does not assume small induced angles of attack, and is capable of optimizing the chord distribution in addition to other design variables. The blade analyzed uses a NACA0012 airfoil from root to tip, with data of the coefficient of lift and drag through the full range of angles of attack obtained from Reference [39]. Again, the coefficient of lift is modified by Mach number using the Prandtl-Glauert transform, and the coefficient of drag is unchanged. All advance ratios are analyzed assuming a relative Mach number of 0.9.

5.3.1 Comparison of Nonlinear Programming Results to Quadratic Programming Results

First, we compare the nonlinear programming results (NLP) for a uniform chord distribution to the Quadratic Programming results shown in the preceeding section. The QP approach is extremely efficient, capable of solving the optimal controls problem for a single advance ratio in about 10 minutes on a single processor machine compared to several hours for the NLP problem. To make a direct comparison of the two methods, the chord distribution is not included as a design variable to be optimized in the following NLP results. Thus, both the NLP and QP solutions will have the same uniform blade planform.

Figure 5.6 shows the minimum total, induced, and profile power losses for varying levels of blade root harmonic control over a range of advance ratios for a uniform chord distribution, as computed by each approach. The NLP results are shown in red, with the QP results in black. The QP and NLP results are very much in agreement, particularly at low advance ratios. The QP method tends to slightly underpredict the viscous power loss, particularly for the $N = 1$ case. This is a result

of using the quadratic drag polar, which underpredicts the coefficient of drag at angles of attack beyond stall, resulting in a lower profile power loss. The minimum induced power losses are also very similar between the two approaches, again with excellent agreement at low advance ratios. For every level of harmonic control across all advance ratios, the QP result slightly underpredicts the total power loss of the NLP result. It is encouraging, however, that the QP and NLP results all follow the same trends and are in general very close to one another.

It is useful to compare the design variables predicted by the two methods, in addition to the minimum powers, to ensure that the two methods don't lead to fundamentally different control inputs. Figure 5.7 shows the optimal fixed blade twist and root pitch input at an advance ratio of $\mu = 0.85$ computed by the QP and NLP approaches. The optimal controls are very similar between the two methods.

Part of the reason the QP method gives good results is that its primary assumptions of a linear lift curve, quadratic drag polar, and small induced angles of attack are reasonable when the blade is operating at small effective angles of attack (i.e. unstalled). These assumptions are less accurate in the reverse flow region of the wake, where geometric angles of attack can be large, leading to large effective and induced angles of attack. In the conventional rotor result, large effective angles of attack are required in the reverse flow region, and in fact on the entire retreating side of the disk, to provide lift to maintain roll trim at high advance ratios. As a result, the optimal controls feature large portions of the blade operating in the stalled regime, leading to significant differences between the QP and NLP results at these high advance ratios. In contrast, the coaxial rotor solution minimizes the circulation in the reverse flow region, and does not require significant lift generation on the retreating side of the rotor. As a result, the optimal coaxial solution does not rely on large angles of attack to maintain roll trim, and the QP and NLP optimum controls and minimum powers are in very good agreement.

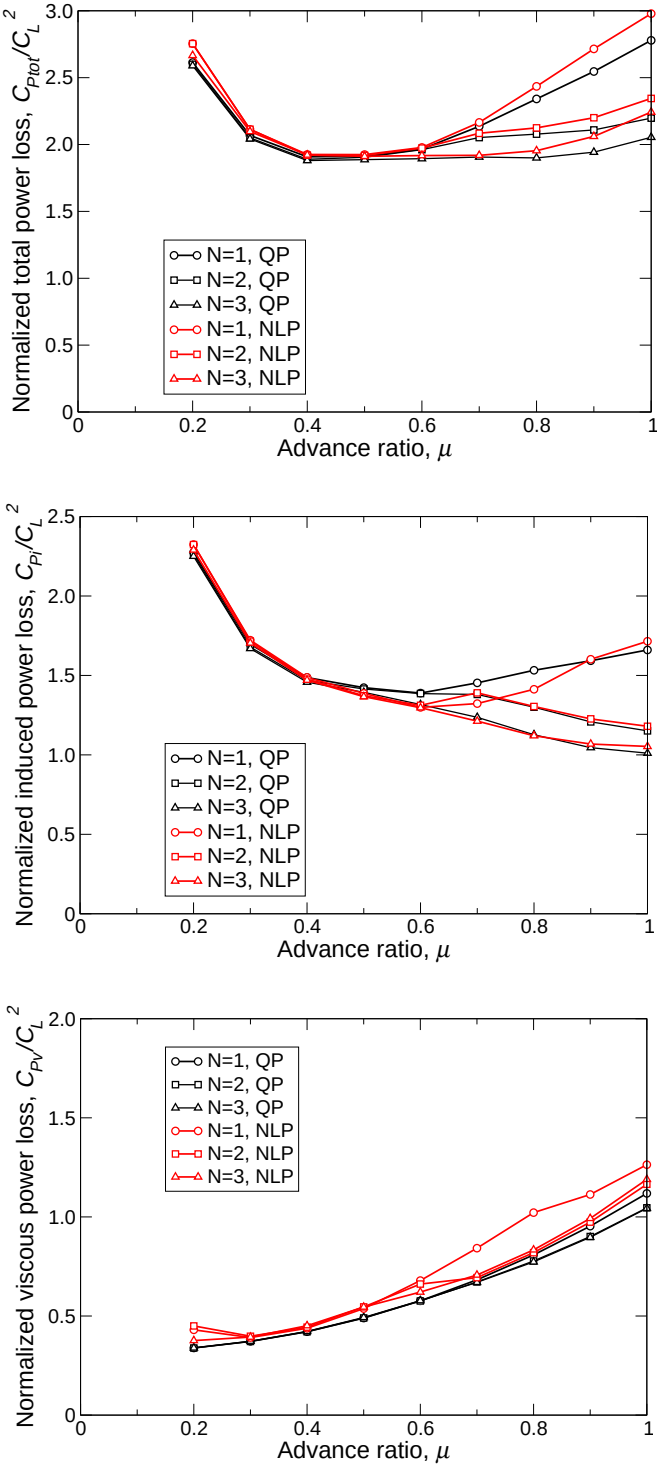

FIGURE 5.6: Top: Minimum power loss for a coaxial rotor with uniform chord distribution, as computed by the Quadratic Programming and Nonlinear Programming methods. Middle and bottom: corresponding induced and viscous power components, respectively.

Figure 5.8 shows the optimal circulation distributions for the QP and NLP results at $\mu = 0.85$. The similarity between the two results reaffirms the accuracy of the QP method. As might be expected, the only significant discrepancy occurs in the reverse flow region, where the QP result computes a higher circulation than the NLP result due to its use of a linear lift curve, resulting in unrealistically high coefficients of lift at these high angles of attack. The QP result is further helped by the fact that the reverse flow region has a low dynamic pressure, resulting in the circulation generated in this region having a relatively small effect on the total calculated power and forces. In summary, the QP method is an extremely useful tool to efficiently compute optimal coaxial rotor design over a range of advance ratios.

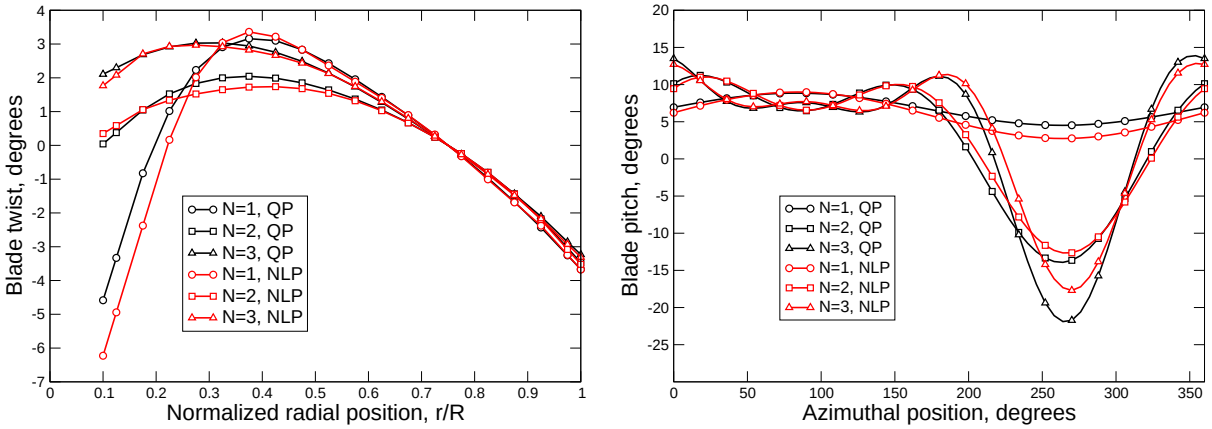

FIGURE 5.7: Optimal radial and azimuthal distributions of blade twist and pitch for coaxial rotors with varying levels of harmonic control at $\mu = 0.85$, with QP results compared to the Newton iteration results with a uniform chord.

5.3.2 Nonlinear Programming Results with Optimized Chord

The primary benefit of the nonlinear approach for the coaxial configuration then, apart from some marginal improvement in accuracy over the QP method, is the ability to optimize the chord distribution. In this section, we examine the improvements that can be gained by tailoring the chord distribution with and without higher harmonic control.

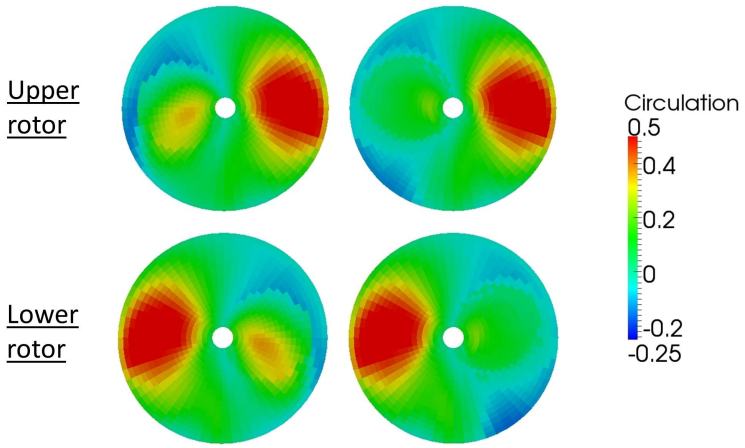

FIGURE 5.8: Optimal circulation distribution for a coaxial rotor with $N = 1$ control at $\mu = 0.85$, as computed by the QP and NLP methods. Left: QP solution. Right: NLP solution.

For each of the optimized chord cases, the modified thrust weighted solidity is constrained to be the same as the X2 technology demonstrator, $\sigma_{\text{TWM}} = 0.116$. If the rotor's solidity is left unconstrained, the optimal rotor for high advance ratios has excessively small blade areas. This is because the high dynamic pressures on the advancing side of each rotor do not require very much blade area to generate the required lift, and small chord values minimize profile losses and lift generation in sub-optimal locations. While very efficient in forward flight, this solution is not practical in hover and is therefore of limited interest. Implementing a solidity constraint ensures an adequate blade area for flight in all regimes, including hover.

We choose to constrain the modified thrust weighted solidity, rather than the traditional thrust weighted solidity. Because the thrust weighted solidity heavily weights chord at the blade tip, and because the circulation goes to zero at the tip regardless of the chord, we found that a constraint on thrust weighted solidity produced oddly shaped tip geometries. To alleviate this problem, we constrain instead the modified thrust weighted solidity defined by Equation 3.64, allowing the optimization to select the most advantageous tip shape for aerodynamic performance.

The minimum blade chord is constrained to be 1% of the rotor radius, to ensure the chord distribution does not assume a negative value at any point along the span. While this very small blade chord would likely not meet structural requirements for the blade, this case is still of interest, as it gives the most aerodynamically efficient rotor design at this speed, and when used in addition to the solidity constraint, ensures sufficient blade area for the vehicle to hover. A case with a higher minimum chord constraint that more accurately reflects the actual design of a blade is given in Section 5.3.6.

Figure 5.9 shows the minimum total power over a range of advance ratios and levels of harmonic control for the coaxial rotor, with all control inputs and design variables optimized at each advance ratio. Also plotted in Figure 5.9 is the minimum total power for the coaxial rotor with a uniform chord distribution, which has the same solidity ($\sigma_{\mathrm{TWM}} = 0.116$) as each optimized chord case. Additionally, the minimum total power for a rotor using $N = 1$ control, a uniform chord distribution, and a blade with no radial blade twist (i.e., an untwisted rectangular blade where only the root inputs are optimized) is also plotted. This serves as a benchmark of performance for the coaxial rotor if the twist, chord, and higher harmonic control design variables are not utilized.

For a given level of harmonic control, optimizing the chord distribution provides power reductions over the uniform chord case at all advance ratios. At the design point of $\mu = 0.85$, the $N = 1$ case with an optimized chord distribution results in a 16% reduction in total power compared to the uniform chord case. This reduction in power is achieved primarily through a reduction in induced power, although profile power losses are also decreased. Use of $N = 3$ control with an optimized chord results in an additional 16% reduction in power compared to the $N = 1$ control case with an optimized chord, showing that even with an optimized chord, higher harmonic control still produces substantial benefits.

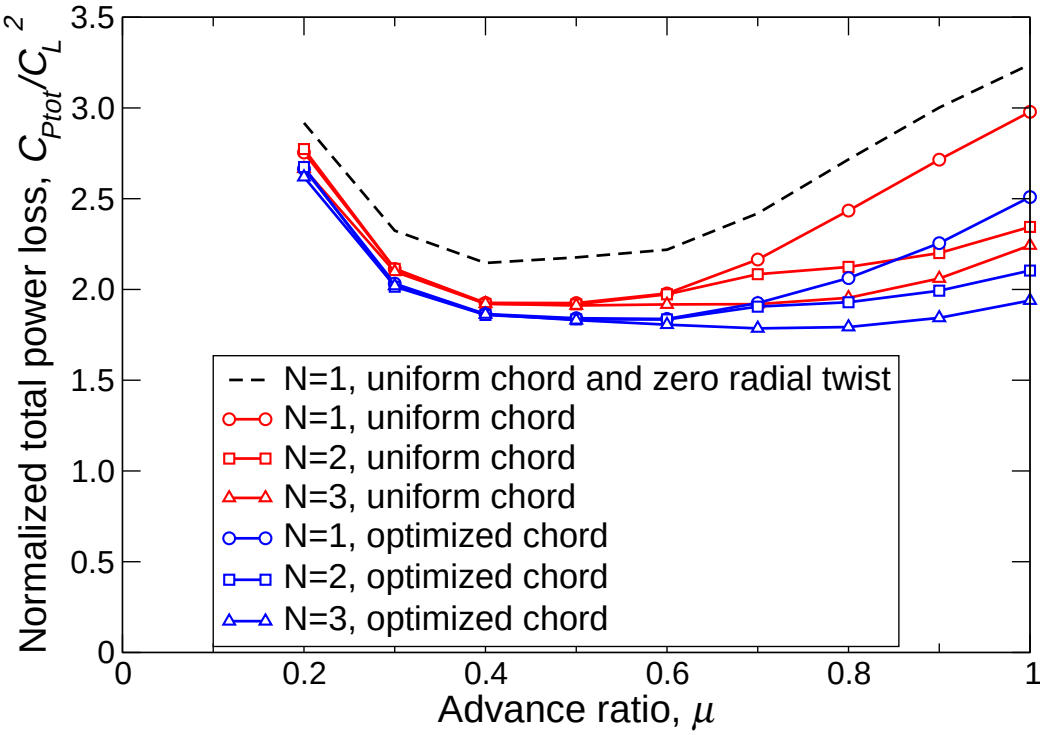

FIGURE 5.9: Minimum power loss for a coaxial rotor with chord optimized compared to a uniform chord case and a uniform chord and uniform twist case.

Figure 5.10 shows the optimal radial twist and pitch input for the optimized chord case at $\mu = 0.85$, as well as the optimal pitch input for the $N = 1$ uniform chord case. Note that because the pitch input for the upper and lower rotors are so similar, for simplicity only the upper rotor pitch input is plotted. Figure 5.11 shows the optimal planform for $N = 1$ and $N = 3$ control, in addition to the baseline uniform chord distribution. As in the uniform chord case, the $N = 1$ case uses a large positive twist gradient on the inboard section of the blade at high advance ratios, in addition to a very small chord at the root. Both the small chord and positive twist gradient serve to decrease the circulation generated in the reverse flow region, resulting in a circulation distribution that more closely resembles the rubber rotor optimum. For the $N = 2$ and $N = 3$ cases, it is optimal to have more of the blade area inboard, and use the extra degrees of freedom in the root pitch input to decrease pitch angle and

minimize circulation on the retreating side. Also of note, the $N = 1$ pitch control for the optimized chord case has switched phase compared to the uniform chord case. For the optimized chord case, cyclic control is no longer providing roll trim, because the coaxial counterrotating rotor is naturally trimmed. Instead, the cyclic control here improves the performance primarily by reducing induced power.

Figure 5.12 shows the circulation distributions for the $N = 1$ fixed and optimized chord cases, the $N = 3$ optimized chord case, and the rubber solution. Looking at the two $N = 1$ cases shows the differences in the circulation distribution simply as a result of optimizing the planform – the positive region of circulation on the retreating side of each rotor is no longer present, due to the small inboard chord distributions, and the region of positive circulation on the advancing side is reduced, more closely resembling the rubber rotor optimum. Using $N = 3$ control with the optimized chord results in further improvements, with the circulation distribution further approaching the rubber rotor optimal.

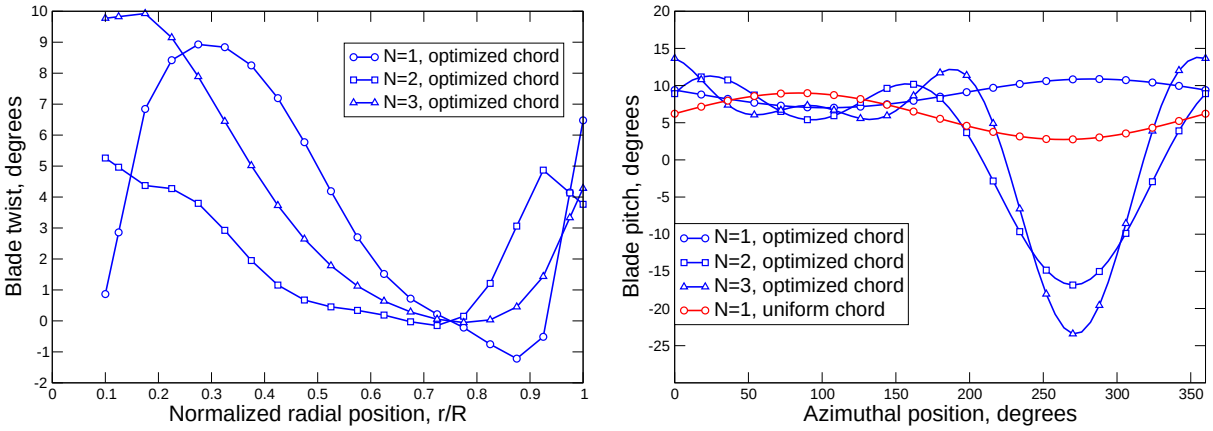

FIGURE 5.10: Optimal radial and azimuthal distributions of blade twist and pitch for coaxial rotors with varying levels of harmonic control and chord optimized at $\mu = 0.85$.

Lastly, Figure 5.13 shows how the optimal blade planform varies with advance ratio for the $N = 1$ case. At low advance ratios, it is optimal to have more of the blade area inboard. This results in higher total blade area, as the inboard chord is weighted

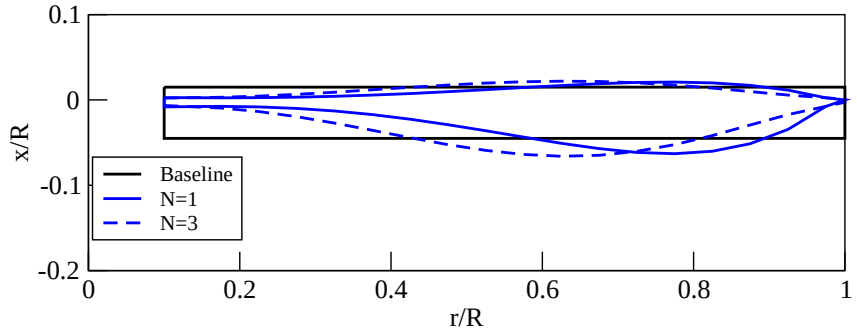

FIGURE 5.11: Optimal coaxial blade planform at $\mu = 0.85$ for varying levels of harmonic control. Note that the modified thrust weighted solidity of all blades is $\sigma_{\text{TWM}} = 0.116$.

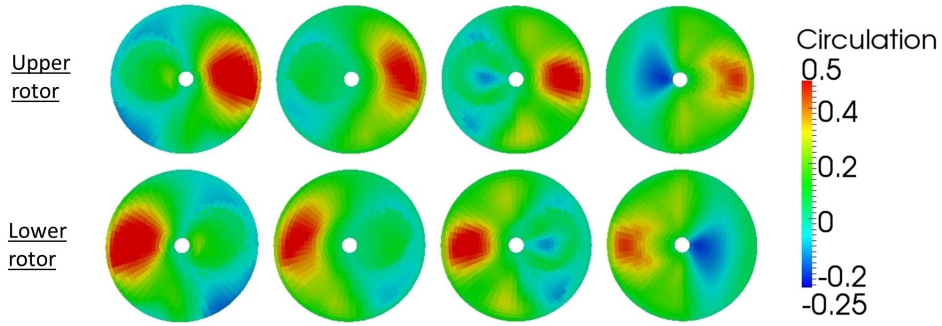

FIGURE 5.12: Optimal circulation distribution for a coaxial rotor with uniform and optimized chord at $\mu = 0.85$. From left to right: $N = 1$ control with uniform chord, $N = 1$ control with optimized chord, $N = 3$ control with optimized chord, rubber rotor solution.

less heavily than the outboard chord; however, at lower speeds, the penalty paid in profile power is also decreased, and the improvement in induced power performance outweighs the increased profile losses.

5.3.3 Comparison of Viscous Optimum to Inviscid Optimum

Up until this point, all coaxial results have shown the optimal controls and minimum powers as determined from a viscous optimization, i.e., an optimization that minimizes the sum of viscous and induced losses. We can also perform an inviscid optimization that only minimizes the induced power, with no regard for the viscous

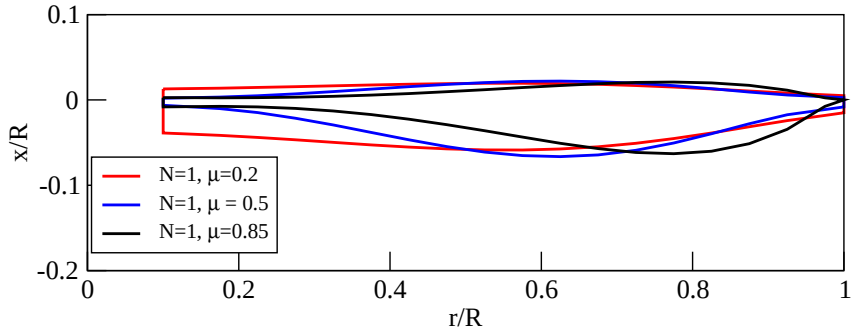

FIGURE 5.13: Optimal coaxial blade planform at varying advance ratios for $N = 1$ harmonic control.

losses. While minimizing viscous losses on a rotor involves decreasing blade area and ensuring that airfoils operate at angles of attack where they have a high ratio of lift to drag, it is not as clear what design features make up the minimum induced loss solution. As a result, it is interesting to look at the completely inviscid solution with no regard to viscous losses, and compare this to the viscous optimization that accounts for both these induced losses and viscous effects.

First, we examine the minimum powers from each of these optimizations at the design point of $\mu = 0.85$, shown in Table 5.1. These cases optimized both chord and twist for $N = 1$, $N = 2$, and $N = 3$ harmonic control. Note that although the inviscid optimization does not account for viscous effects in determining the optimal control inputs, the viscous power loss associated with these controls can still be computed, to give the inviscid solution a viscous and total power. First note that for the inviscid optimization, higher harmonic control results in decreased induced power (C_{Pi}/C_L^2), while for the viscous solution, higher harmonic control results in decreased total power (C_{Ptot}/C_L^2) It is interesting to see how the viscous solution achieves this reduction in total power with the use of higher harmonic control. The $N = 2$ viscous solution improves total power through decreases in viscous power; in fact, the inviscid power is actually slightly higher for the $N = 2$ solution than the $N = 1$ solution. The $N = 3$ viscous solution is able to substantially reduce

Table 5.1: Induced, viscous, and total power at $\mu = 0.85$ for coaxial rotor at inviscid and viscous optimal solutions.

	N=1		N=2		N=3	
	Inviscid design	Viscous design	Inviscid design	Viscous design	Inviscid design	Viscous design
Induced power, C_{Pi}/C_L^2	1.11	1.19	1.05	1.20	1.00	1.04
Viscous power, C_{Pv}/C_L^2	1.26	0.97	1.75	0.76	1.15	0.77
Total power, C_{Ptot}/C_L^2	2.38	2.15	2.81	1.96	2.15	1.81

induced power over the $N = 2$ solution while maintaining the same viscous losses. At $N = 3$, the induced power for the viscous solution, 1.04, is very close to the minimum induced power, 1.00. In fact, the viscous optimization is within 15% of the minimum induced power loss at all levels of harmonic controls, indicating that minimizing induced power losses is a key driver in minimizing total power.

The fact that induced losses dominate the viscous optimization is also reflected in Figure 5.14, which shows the optimal radial pitch and root pitch input for the inviscid and viscous solutions using $N = 1$ and $N = 3$ control at the design point of $\mu = 0.85$. In all cases, both the blade twist and blade chord are optimized. The inviscid radial blade twist is very similar to the viscous solution, with the exception of the behavior at the tip of the blade, where the viscous solution has a large positive twist gradient. The root pitch inputs are also very similar between the viscous and inviscid solutions, however the inviscid inputs tend to "exaggerate" the same features seen in the viscous solutions. For example, the $N = 3$ inviscid solution has a significantly larger decrease in pitch angle between $\psi = 230°$ and $\psi = 330°$ than the viscous solution. The inviscid solution is able to achieve slightly lower induced powers by using this large negative blade pitch, reducing circulation in this region. However, the resultant large angles of attack seen on some portions of the blade result in blade stall and high coefficients of drag, as evidenced by the fact that the inviscid solution

has nearly 50% higher viscous drag then the viscous solution. The viscous solution uses a slightly less drastic dip in pitch angle, trading a small increase in induced power for a large decrease in viscous power to locate the minimum total power. This similarity in the controls results in nearly identical circulation distributions between the inviscid and viscous solutions, as shown in Figure 5.15 for the $N = 1$ case. The viscous solution has slightly exagerrated regions of circulation, resulting in slightly higher induced powers; however, this tradeoff induced power results in a decrease in viscous power and a net reduction in total power.

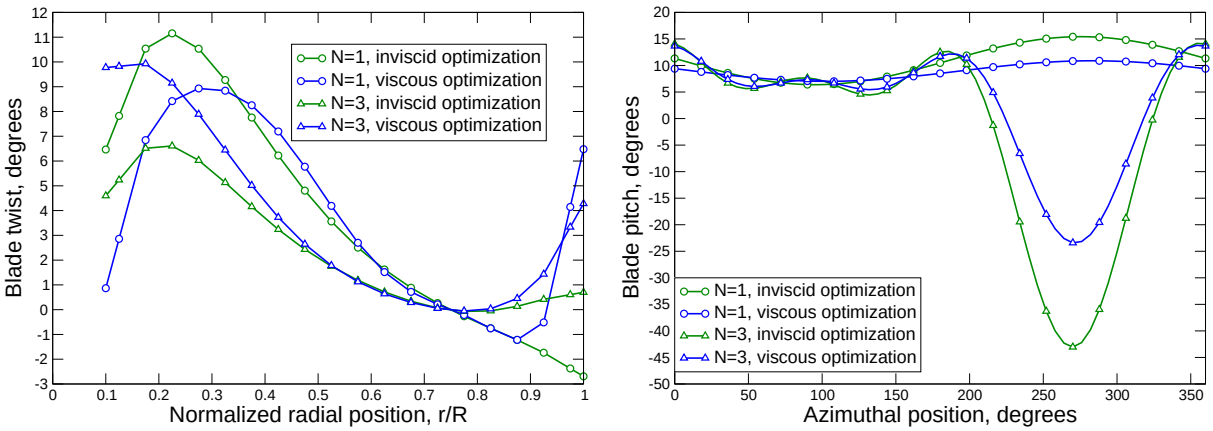

FIGURE 5.14: Comparison of inviscid and viscous radial and azimuthal distributions of blade twist and pitch for $N = 1$ and $N = 3$ control at $\mu = 0.85$.

Figure 5.16 shows the optimal blade planforms for the $N = 1$ and $N = 3$ inviscid and viscous optimizations at the design point. Similar to the radial blade twist distributions, the $N = 1$ viscous and inviscid solutions have remarkably similar planforms with the exception of the blade tip. The viscous optimum has a drastically reduced tip chord, a feature that makes sense given the high dynamic pressure at the tip and the minimal impact on the induced power that this region has, given that the circulation goes to zero at the tip regardless of blade geometry. The $N = 3$ inviscid case does not have the large tip chord seen in the $N = 1$ case. As a result, for $N = 3$ control, the inviscid and viscous solutions have a nearly identical planform.

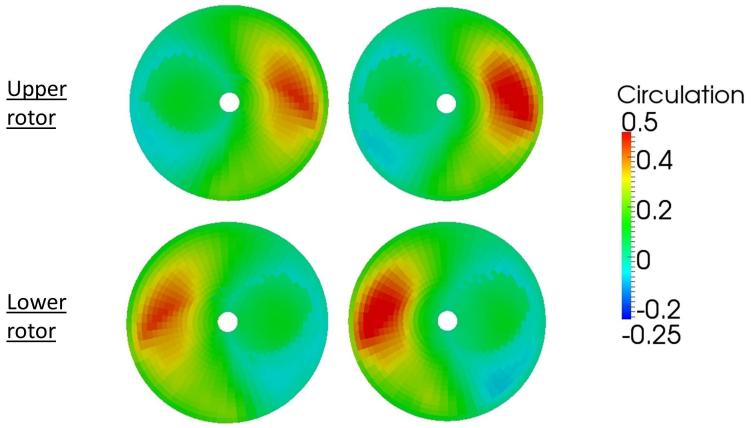

FIGURE 5.15: Optimal circulation distribution for a coaxial rotor with optimized chord and $N = 1$ control at $\mu = 0.85$ Left: Inviscid solution. Right: Viscous solution.

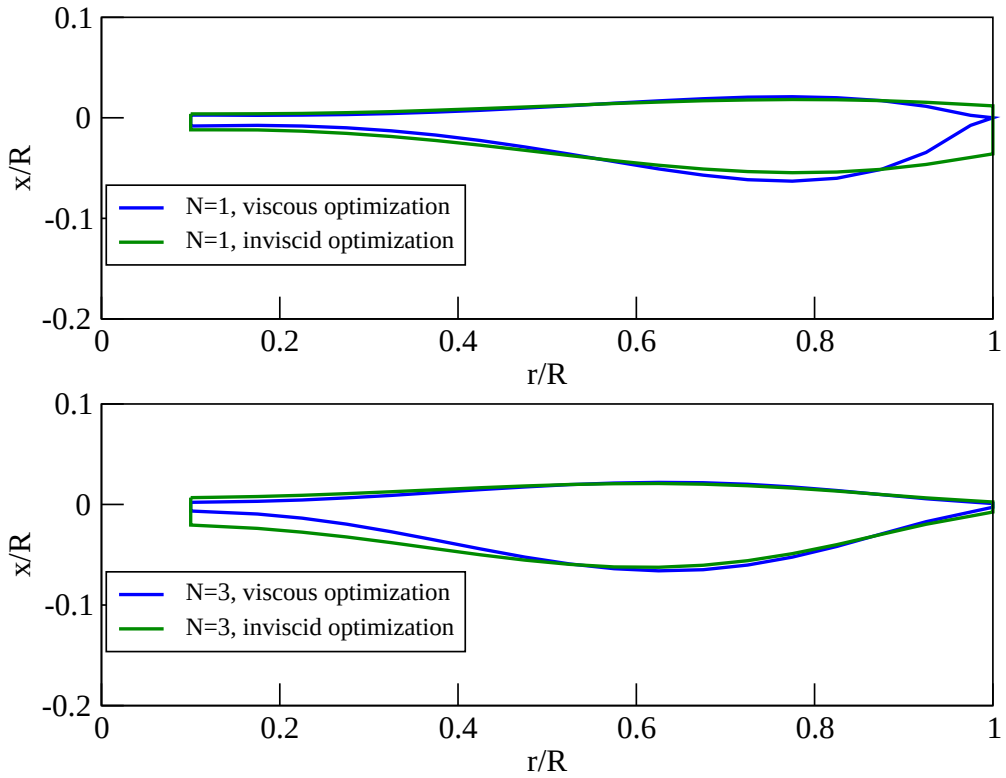

FIGURE 5.16: Comparison of inviscid and viscous optimal planforms at $\mu = 0.85$ for $N = 1$ and $N = 3$ control.

5.3.4 Single Point Optimization

The previous results showed the minimum power solution with every design variable optimized at each advance ratio. Practically, a single planform and radial twist distribution would need to be used across all advance ratios. In this section, we explore how a single blade design performs across a range of advance ratios. Additionally, we investigate what design point maximizes performance across advance ratios, and how higher harmonic control affects off-design performance of a blade. Two blade designs were analyzed across multiple advance ratios for each level of higher harmonic control: the optimal blade for the $\mu = 0.5$ flight condition, and the optimal blade for the $\mu = 0.85$ flight condition. For these cases, the radial twist and planform were held fixed, while only the root pitch inputs were varied at each advance ratio as required to ensure zero net trim on the vehicle and minimize total power. Figure 5.17 shows the total power for the $N = 1$, $N = 2$, and $N = 3$ cases using both the $\mu = 0.5$ optimal blades and the $\mu = 0.85$ optimal blade. Also included is the minimum total power with blade chord and twist optimized at each advance ratio, providing a lower bound on performance for a given level of control and advance ratio. As a baseline level of performance, the minimum total power of a uniform chord, untwisted blade is also plotted.

In all cases, the single point designs achieve very close to optimal performance around their design point, as expected. For the $N = 1$ case, the $\mu = 0.5$ blade has a 5% increase in power at $\mu = 0.85$ and an 8% increase at $\mu = 1.0$ over the optimal design at each of these advance ratios. The $\mu = 0.85$ blade performs worse than the optimal at low advance ratios, with a total power 10% higher than the optimum at $\mu = 0.2$. Both blades perform significantly better than the baseline untwisted, uniform chord blade at all advance ratios, with the exception of the region between $\mu = 0.2 - 0.3$ for the $\mu = 0.85$ single point design, where power required

is approximately equal to the baseline blade. For the $N = 2$ and $N = 3$ cases, the differences in power between the single point designs and the absolute minimum power decreases. In fact, for $N = 3$ harmonic control, both the $\mu = 0.5$ and $\mu = 0.85$ designs are nearly exactly equal to the minimum power across all advance ratios. This is due to the increased degrees of freedom in the blade root control scheme, allowing for similar levels of performance even with a different fixed blade twist and chord.

In summary, even at off-design points, the optimal blades perform nearly as well as the minimum power solution, and in almost every case perform better than a uniform chord, untwisted blade. This is an encouraging result, as selecting a single planform and radial twist distribution, which would be necessary in the design of a real rotor, can still lead to close to near-optimum performance at off-design advance ratios. Of course, this analysis does not account for hover performance, which often has conflicting design requirements with high speed cruise efficiency. A thorough multi-point design that includes a hover analysis is required to determine the overall optimal aerodynamic rotor design.

5.3.5 Performance with Constrained Lift Offset

Lift offset is defined as the effective lateral displacement of the lift vector for each of the rotors from the hub center line, or $\Delta M_x/LR$ where ΔM_x isthe difference in rolling moment between the two rotors, R is rotor radius, and L is total lift. Figure 5.18, taken from Reference [5], illustrates this concept of lift offset in a coaxial rotor system. Note that the rotor system must have zero net rolling moment for trimmed flight.

The optimal solutions presented in the preceeding sections are all unconstrained in lift offset, allowing the optimization to determine the level of lift offset that results in the minimum power. Figure 5.19 shows the optimal lift offset at each advance ratio for the viscous, optimized chord solutions with varying levels of harmonic control.

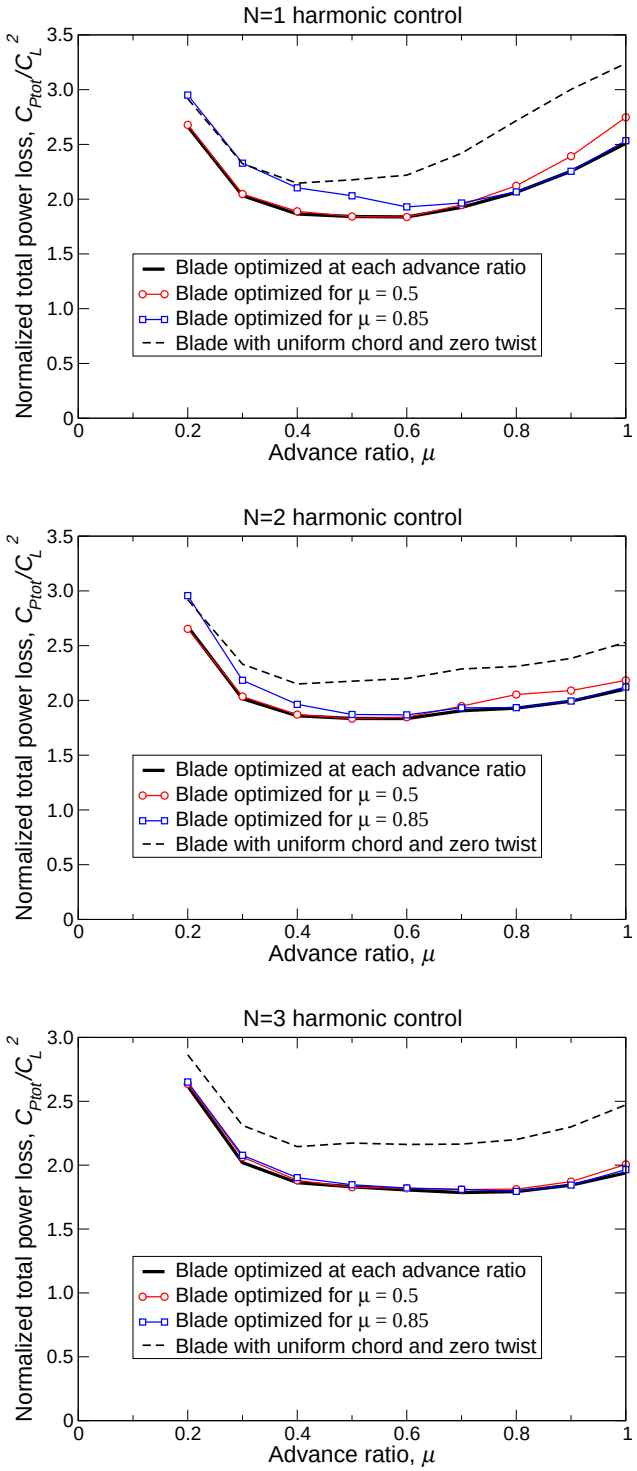

FIGURE 5.17: Minimum total power using $\mu = 0.5$ and $\mu = 0.85$ optimal blade design across a range of advance ratios. From top to bottom: using $N = 1$, $N = 2$, and $N = 3$ harmonic control.

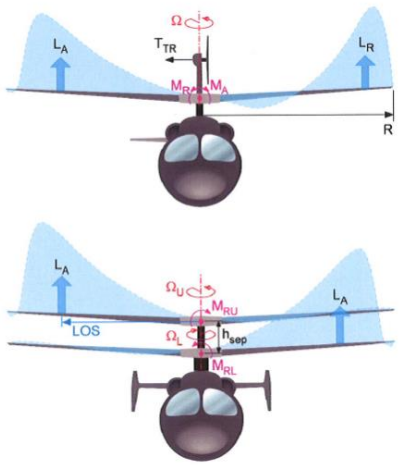

FIGURE 5.18: Illustration of lift distribution and lift offset on a coaxial rotor system compared to a single rotor. Taken from Reference [5].

Each level of harmonic control has a similar lift offset until an advance ratio of $\mu = 0.7$, at which point the $N = 2$ and $N = 3$ cases have a somewhat smaller lift offset than the $N = 1$ case. This indicates that the higher harmonic control cases generate lift further inboard than the $N = 1$ case, a feature that is reflected in the inboard concentration of blade chord shown in Figure 5.11.

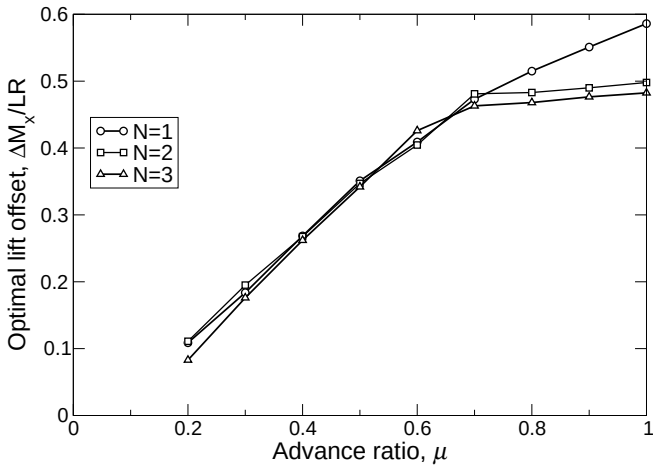

FIGURE 5.19: Optimal lift offset versus advance ratio for varying levels of harmonic control for a coaxial rotor with chord optimized.

In the actual design of a rotor, it may be necessary to constrain the rotor's lift

offset to limit blade root and shaft bending moments for structural considerations. Figure 5.20 shows the minimum induced, viscous, and total power for the $N = 1$ case with the lift offset constrained to values between 0.3 and 0.7 at the $\mu = 0.85$ design point. Note that the optimal value of lift offset at this advance ratio, as shown in Figure 5.19, is approximately 0.53. This plot shows that at values of lift offset lower than the optimal, there is an increase in both viscous and induced powers compared to the unconstrained power. At high values of lift offset, the total power increases because of increases in induced power; the viscous power actually continues to decrease with increasing lift offset.

Figure 5.21 shows the minimum total power for varying levels of harmonic control with the lift offset constrained between 0.3 and 0.7. Note that in each of these cases, all rotor design variables are optimized at the specified lift offset constraint. At a high prescribed lift offset, the advantages of higher harmonic control decrease dramatically, and all three levels of harmonic control approach the same minimum power. At low prescribed lift offsets, the minimum total powers for the $N = 2$ and $N = 3$ control cases are significantly lower than the power for the $N = 1$ control case. This is an interesting result, as in the design of a real rotor, there may be a limit on the maximum lift offset. For example, according to Reference [5], the lift offset was limited to 0.3 for structural and hub weight considerations in the design of the X2 technology demonstrator. At this lift offset, use of $N = 2$ control produces a 47% decrease in total power, a much larger improvement than the 9% reduction achieved with $N = 2$ control and an unconstrained lift offset.

Figure 5.22 shows the optimal force distribution for the cases with lift offset constrained to 0.3 using both $N = 1$ and $N = 3$ control. These are compared to the optimal force distribution for the solution unconstrained in lift offset with $N = 1$ control. For the unconstrained case, the lift is generated in a large region on the advancing side of each rotor, resulting in a lift offset of 0.53. Implementing a

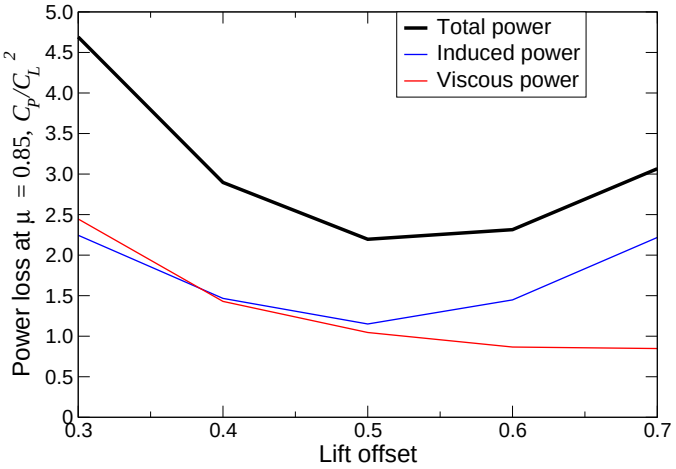

FIGURE 5.20: Minimum induced, viscous, and total powers at $\mu = 0.85$ with varying prescribed values of lift offset for $N = 1$ control.

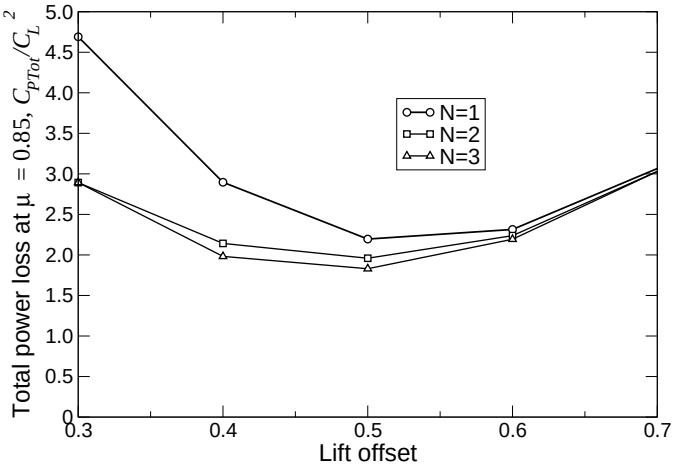

FIGURE 5.21: Minimum total power at $\mu = 0.85$ with varying prescribed values of lift offset and varying levels of harmonic control.

constraint on the lift offset drastically changes the optimal force distribution. The $N = 1$ constrained case generates lift in two main regions, between $\psi = 0°$ and $\psi = 45°$, and between $\psi = 135°$ and $\psi = 180°$. The lift is generated near the tip of the blade in these two regions, however this distribution results in less rolling moment on each rotor than the unconstrained case, as these regions are closer to the longitudinal axis of the rotor. To further reduce the rolling moment on each rotor, a large negative force is generated near the tip of the blade on the advancing

side at $\psi = 90°$. The $N = 3$ solution is able to satisfy the lift offset constraint more efficiently by concentrating the majority of lift into one main region on the advancing side, located at $\psi = 90°$, that is located further inboard than the unconstrained case.

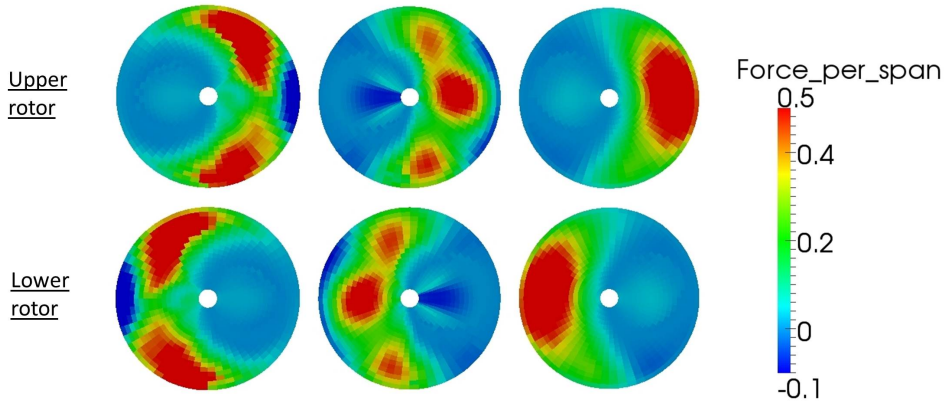

FIGURE 5.22: Optimal force distribution for a coaxial rotor with lift offset constrained to 0.3, at $\mu = 0.85$. Left: lift offset = 0.3 with $N = 1$. Middle: lift offset = 0.3 with $N = 3$. Right: lift offset = 0.53 (unconstrained) with $N = 1$.

5.3.6 Comparison to X2 Technology Demonstrator Blade Design

In this section, we compare the results of our analysis to the actual rotor design of the X2 Technology Demonstrator. We make several changes to the configuration being analyzed to more closely match the X2 parameters. First, we constrain the lift offset to a value of 0.3, to match the X2's design lift offset. Second, we use a root cutout of 15% rather than 10%. Lastly, we use a different minimum chord constraint. In the preceeding analysis, the minimum chord value at any radial station is constrained to be 1% of the rotor radius, which in this section will be referred to as the baseline minimum chord constraint. Of course, the X2 blade has structural and other requirements that likely preclude the use of such a small chord. To get a more accurate comparison to the X2 design, we constrain the chord to be greater than 5% of the rotor radius at points inboard of a normalized radial position of 0.8

and 2.5% of the rotor radius outboard of 0.8. This set of constraints is referred to as the X2 minimum chord constraint.

The top plot of Figure 5.23 shows the blade planform for the X2 design, taken from Reference [5], compared to the $N = 1$ optimal planform as determined by our analysis with the baseline chord constraint, at the design point of $\mu = 0.85$. The optimal blade from our analysis features a significantly smaller chord on inboard portions of the blade than the X2 design, while also using a much larger twist at these stations, as seen in the lower plot of Figure 5.23.

The optimal planform and twist using the X2 minimum chord constraint is shown in the middle and lower plots of Figure 5.23. The $N = 1$ optimal planform is very similar to the X2 blade. While the twist distributions differ somewhwat, they both have a positive twist gradient out to approximately 30-40% span, and then a large negative twist gradient out to the tip. There are several notable differences between the methods used in the X2 blade design and the analysis presented here. The X2 blade was designed to minimize profile losses, and utilizes a complicated distribution of airfoils and blade thicknesses, whereas the analysis presented here is designed to minimize both induced and profile losses and uses a NACA 0012 airfoil from root to tip, which could help to explain some of the differences in the optimal twist distributions.

We now compare the results of our analysis using higher harmonic control and the X2 minimum chord constraint to the X2 TD blade design. Figure 5.24 shows the optimal blade planform for the $N = 3$ case to the X2 planform. Using $N = 3$ control results in a very different chord distribution than the $N = 1$ and X2 designs, with more area shifted inboard and a slightly smaller chord near the tip. The twist distribution for the $N = 1$ and $N = 3$ cases and the X2 are shown in Figure 5.25. These results demonstrate that if the X2 technology demonstrator were to use higher harmonic control, a blade and twist redesign would likely be necessary to achieve

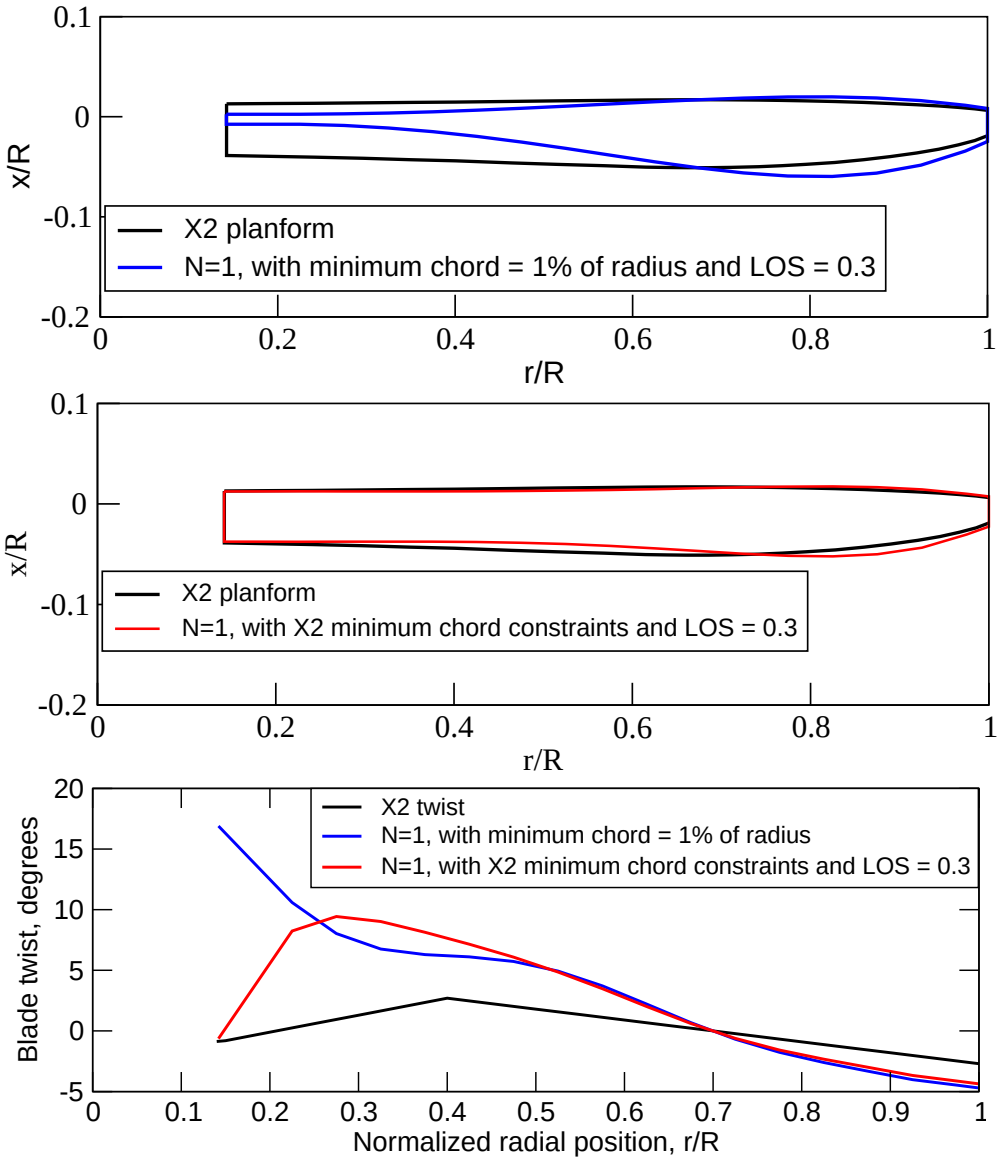

FIGURE 5.23: X2 Technology Demonstrator blade planform and twist compared to $N = 1$ optimal results with varying chord constraints.

optimal performance.

Table 5.2 shows the minimum total power for $N = 1$, $N = 2$, and $N = 3$ control using both the X2 minimum chord constraint and the baseline minimum chord constraint. Using a blade that satisfies the X2 minimum chord constraint results in approximately 10% higher total power for $N = 1$ control than the blade satisfying the

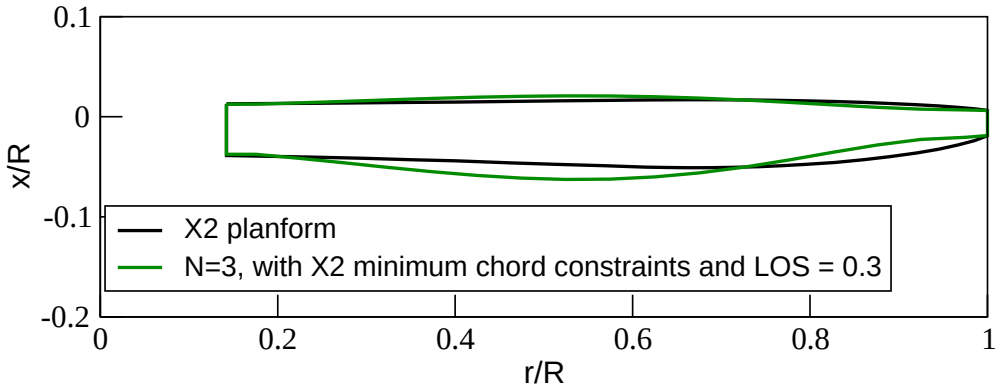

FIGURE 5.24: X2 Technology Demonstrator blade planform compared to $N = 3$ optimal results with X2 minimum chord constraints.

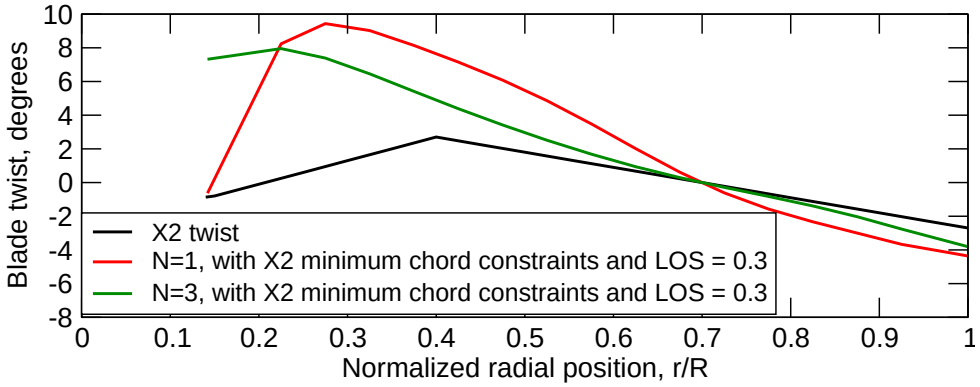

FIGURE 5.25: X2 Technology Demonstrator twist compared to $N = 1$ and $N = 3$ optimal twist distributions with X2 minimum chord constraints.

baseline minimum chord constraint. For $N = 2$ control, using the more restrictive X2 minimum chord constraint only results in a 2% increase in power over the baseline chord constraint. The increased level of harmonic control is capable of mitigating the power increases associated with a larger inboard chord. Another interesting conclusion from Table 5.2 is that using $N = 2$ control with the X2 minimum chord constraints and constrained to a lift offset of 0.3 results in a 40% reduction in total power compared to the $N = 1$ control case. In summary, in the practical design of the rotor where excessively small chord values are prohibited and the maximum lift offset is constrained, higher harmonic control is very effective at reducing power

requirements at high speeds.

Table 5.2: Minimum total power, C_{Ptot}/C_L^2, at $\mu = 0.85$ for a coaxial rotor with varying levels of harmonic control subject to the X2 minimum chord constraints or the baseline minimum chord constraint.

N/rev control	X2 minimum chord constraint and LOS = 0.3	Baseline chord constraint LOS = 0.3
N=1	5.26	4.80
N=2	3.14	3.09
N=3	2.95	2.89

5.4 Conclusions from Coaxial Rotor Analysis

Based on the analysis of coaxial rotors using higher harmonic control in this section, we can draw the following specific conclusions

1. The quadratic programming method provides for an accurate approximation of optimal rotor design and minimum power requirements for the optimization of a fixed blade chord. The method is computationally fast, requiring only several minutes for each flight condition, and produces a solution that is very close to the more accurate nonlinear method.

2. Higher harmonic control is effective in reducing total power at advance ratios above $\mu = 0.5$. When using an optimized chord distribution in all cases, $N = 2$ control provides a 9% power reduction and $N = 3$ control provides an additional 16% power reduction over a rotor using $N = 1$ control at the design advance ratio of $\mu = 0.85$. The $N = 2$ solution achieves power losses by decreasing viscous power, while the $N = 3$ solution achieves additional power losses by decreasing both induced and viscous power compared to the $N = 1$ solution.

3. The viscous optimum is driven by induced losses, as the $N = 1$, $N = 2$, and $N = 3$ viscous solutions have similar control inputs and rotor design features as

the inviscid optimal solution. At the design advance ratio, the induced power loss for the viscous solution is within 15% of the inviscid solution's minimum induced power loss for all levels of harmonic control.

4. Using the $\mu = 0.5$ and $\mu = 0.85$ optimal blades across a range of advance ratios provides an improvement in performance relative to an untwisted, uniform chord blade at all advance ratios for $N = 1$ control. However, the power at off-design advance ratios is substantially higher than the minimum power achieved when using a blade optimized for each advance ratio.

5. Using the $\mu = 0.5$ and $\mu = 0.85$ optimal blades across a range of advance ratios with $N = 2$ and $N = 3$ harmonic control results in nearly optimal performance even at off-design points. For the $N = 3$ case in particular, the $\mu = 0.5$ or $\mu = 0.85$ optimal blades at advance ratios from 0.2 to 1 result in total powers that are nearly as low as optimizing the blade at each advance ratio. This indicates that another benefit of higher harmonic control is improving a given blade design's performance at off-design conditions.

6. The optimal lift offset of the coaxial rotor system increases with increasing advance ratio, reaching a value above 0.5 for $N = 1$ control. Use of $N = 2$ and $N = 3$ control results in a slightly lower optimal lift offset at high advance ratios.

7. If the lift offset is constrained to values that are lower than optimal, which may be a requirement in the actual design of a rotor, $N = 2$ and $N = 3$ control provide an even larger reduction in power compared to the case that is unconstrained in lift offset. For example, with the lift offset constrained to 0.3 and the blade planform optimized, use of $N = 2$ harmonic control results in a 47% decrease in power requirements over $N = 1$ control at $\mu = 0.85$, compared

to a 9% decrease in power when each system is unconstrained in LOS. This indicates that higher harmonic control can provide significantly larger power reductions on a coaxial rotor system where the maximum allowable lift offset is less than 0.5.

8. When minimum chord constraints meant to resemble the X2 blade are implemented, the resulting $N = 1$ optimal rotor design has a blade planform and twist distribution that resemble the actual X2 blade. Using $N = 2$ or $N = 3$ control with the same chord constraints results in a signficantly different optimal planform and twist distribution, while providing large reductions (40%) in total power at the design point over the $N = 1$ case. This indicates that higher harmonic control may improve high speed aerodynamic efficiency if implemented in the design of the X2 TD or similar rotorcraft.

6

Wing-Rotor Compound Results

6.1 Baseline Rotor

In this section, we analyze the optimal performance of a Cheyenne-style compound helicopter with a four-bladed rotor and lifting wing. The parameters selected for this configuration were meant to resemble the Cheyenne AH-56 helicopter.

We consider a rotor very similar to the conventional rotor described in Chapter 4, with no coning and the shaft tilted nose down at an angle of $\alpha_{\text{shaft}} = -5°$. The baseline rotor has a thrust weighted solidity of $\sigma_{\text{TW}} = 0.1156$. We use a root cutout equal to 10% of the rotor radius, with a vertical spacing between the rotor and wing equal to 25% of the rotor radius. The coefficient of rotor lift is prescribed, with $C_L = 0.00926$. The net roll and pitch moment on both the wing and rotor are constrained to zero, although each individual device may have a net moment on it. Although the relative tip Mach number of a rotor would vary with advance ratio, we assume a constant $M_{\text{tip}} = 0.9$ over the range of advance ratios. We evaluate varying levels of harmonic control to determine its effect on minimum power and optimal rotor design. Note that harmonic pitch control is used in the rotor only. The wing

has $N = 0$ control in all cases, i.e., the wing's twist is fixed in time in all cases (note, however, that the wing's radial twist distribution is optimized). Although we are not making comparisons to a specific design point, as we did in the coaxial rotor case using the X2 TD design intent, we will examine optimal controls at two advance ratios: $\mu = 0.5$, which is typical of the maximum advance ratio on the Cheyenne, and $\mu = 0.8$, to explore potential rotor designs for future compound rotorcraft with increased top speeds.

The baseline wing has a span equal to the rotor radius and an aspect ratio of 3.5. For the vortex-lattice model, we used 18 elements in the spanwise direction and 20 elements in the azimuthal direction for each of the four rotor blades. For the wing, we use 20 elements in the spanwise direction with 20 elements per quarter period. The complete model contains 1840 vortex ring elements.

6.2 Quadratic Programming Results

In this section, we present solutions to the optimal blade control problem for the baseline rotor with fixed chord, varying radial twist, a quadratic drag polar, and linearized lifting line theory. The radial twist of the wing is optimized in addition to the twist of the rotor. The airfoil sectional lift curve slope is equal to 2π, and the drag polar from Figure 2.3 is used.

Figure 6.1 shows the computed minimum total, induced, and profile power losses for varying levels of blade root harmonic control over a range of advance ratios. Also shown is the rubber rotor minimum power. Higher harmonic control is effective at achieving significant reductions in power, particularly at advance ratios above $\mu = 0.6$. Almost all of this reduction is due to reductions in induced power, as the viscous power loss is nearly constant regardless of the level of harmonic control. Because of the large baseline chord of the wing, viscous power is the dominant contributor to total power at high advance ratios, particularly with $N = 2$ or higher

control. However, through induced power reductions alone, $N = 10$ control results in an approximately 20% decrease in total power at $\mu = 0.8$ compared to $N = 1$ control, compared to a 5% reduction at $\mu = 0.5$.

To shed light on the mechanism behind this power reduction, we now look at the optimal controls at $\mu = 0.5$, where higher harmonic control only achieves modest power reductions, and $\mu = 0.8$, where it achieves large power reductions. Figures 6.2 shows the optimal rotor blade radial twist, azimuthal pitch input, and fixed wing twist at each of these advance ratios for varying levels of harmonic control. For the $\mu = 0.5$ case, the rotor radial twist distribution and azimuthal pitch input are relatively similar for all levels of harmonic control. The $\mu = 0.8$ case has significant differences between the $N = 1$ case and $N = 2$ cases. For $N = 2$ control, the inner 40% of the blade no longer has the large positive twist gradient seen in the $N = 1$ case, and instead has a twist distribution that monotonically decreases from root to tip. Additionally, the $N = 2$ case has a large decrease in pitch angle from $\psi = 230°$ to $\psi = 330°$ that is not present in the $N = 1$ case.

The advantages of these differences in the rotor's radial twist and azimuthal pitch can be deduced from Figures 6.3 and 6.4, which show the optimal circulation distributions at $\mu = 0.5$ and $\mu = 0.8$, respectively. The rubber rotor solution, shown at the far right of each image, is significantly different between the two advance ratios. At $\mu = 0.5$, it contains a region of positive circulation on the retreating side of the rotor. The $N = 1$ case is able to achieve a similar circulation distribution by using the small ($\approx 2°$) cyclic pitch input shown in Figure 6.2. As a result, the $N = 1$, $N = 2$, and $N = 10$ optimal design variables and circulation distributions are very similar, and higher harmonic control does not provide significant power reductions. At $\mu = 0.8$, however, the rubber rotor solution contains a large region of negative circulation on the inboard portion of the retreating side. Similar to the coaxial case, a reduction in circulation in this region is most effectively achieved via

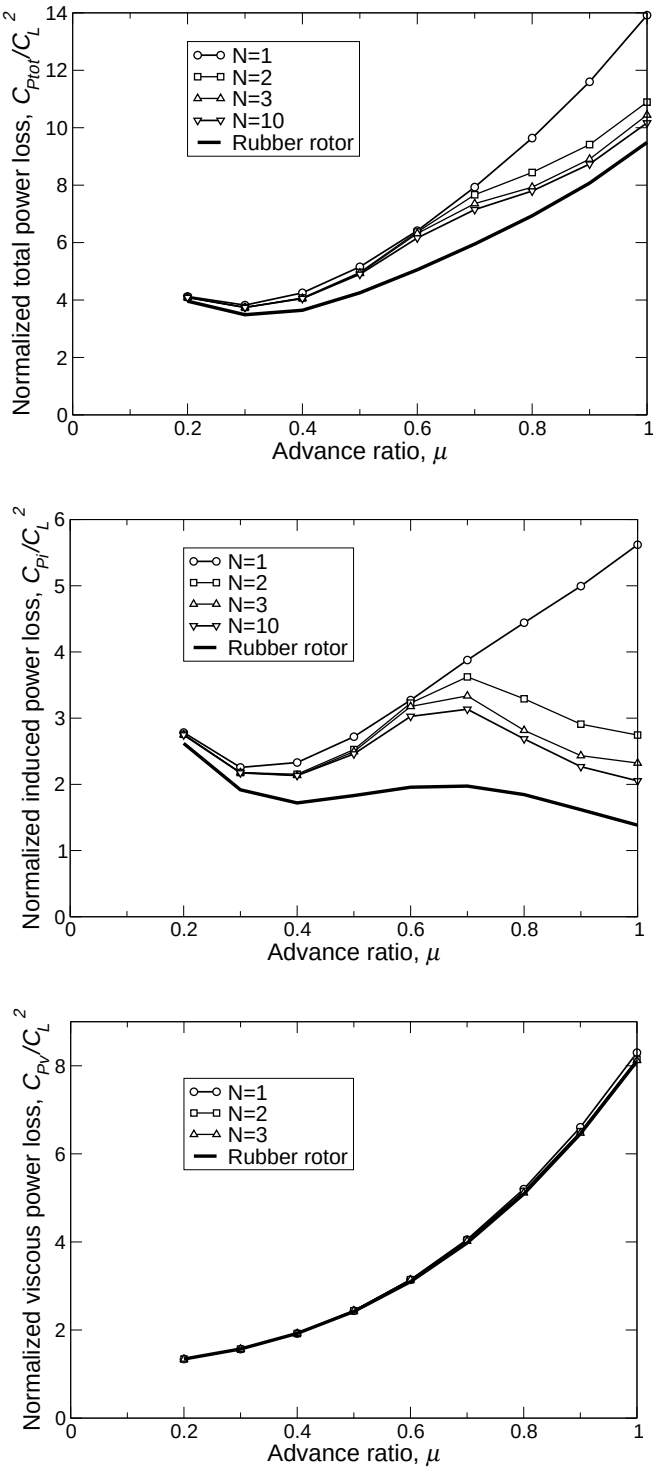

FIGURE 6.1: Top: Minimum power loss for a wing-rotor compound in trimmed forward flight with varying levels of blade root harmonic control. Middle and bottom: corresponding induced and viscous power components, respectively. All results use the Quadratic Programming approach.

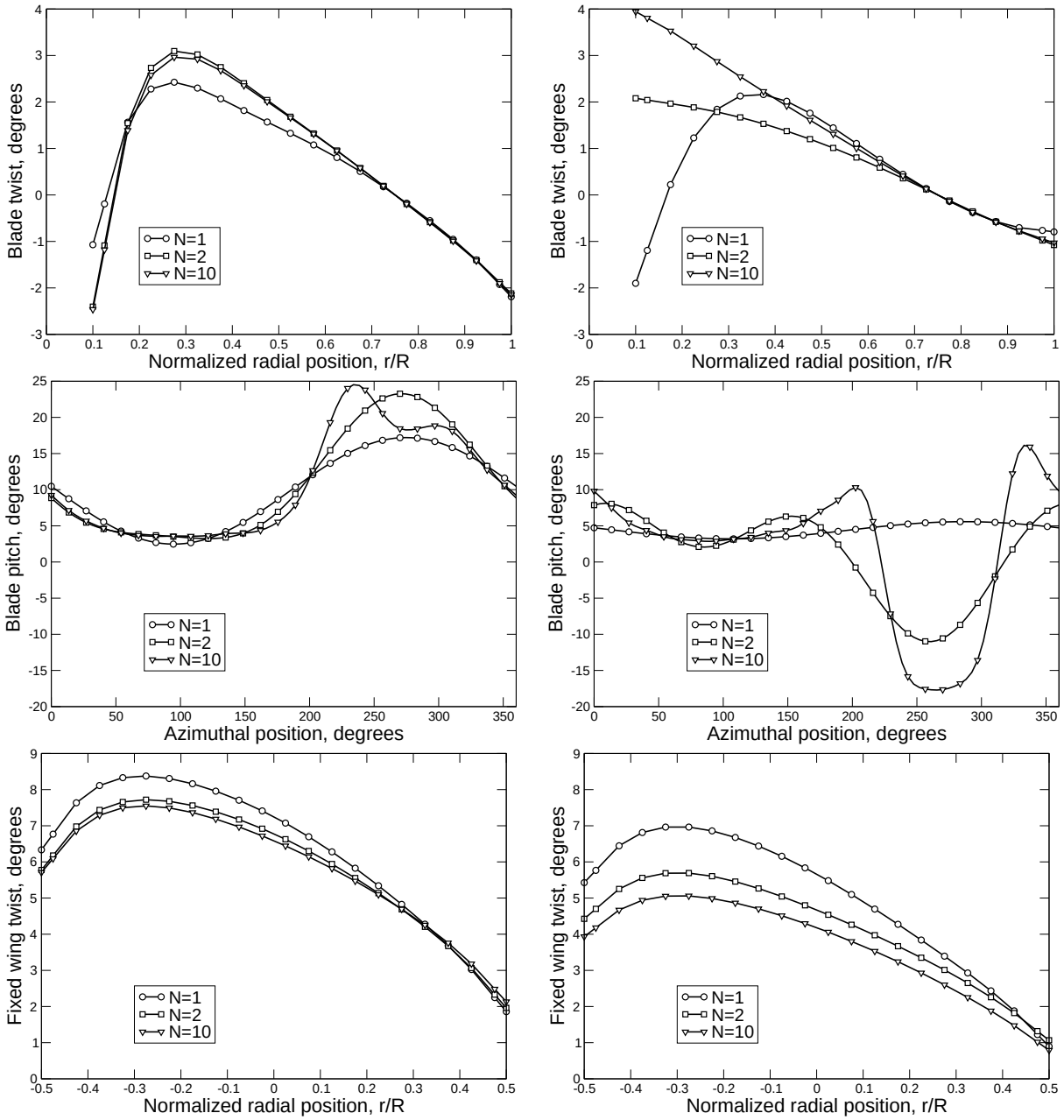

FIGURE 6.2: Left: Optimal control inputs at $\mu = 0.5$. Right: Optimal control inputs at $\mu = 0.8$. Top: Optimal radial rotor twist of wing/rotor compound. Middle: Optimal azimuthal pitch. Bottom: Optimal radial twist of wing.

a large decrease in pitch as the blade sweeps through this region, an azimuthal pitch distribution that is only possible with the use of $N = 2$ or higher harmonic control. This feature is only optimal at high advance ratios; at advance ratios below about $\mu = 0.6$, it is more effective to use a large positive twist gradient than a large decrease in pitch input on the retreating side of the rotor. As a result, the $N = 1$ solution at $\mu = 0.8$ has a large region of positive circulation not present in the rubber rotor solution, while the $N = 2$ and $N = 10$ solutions are able to minimize the circulation in this region, resulting in lower power requirements with the use of higher harmonic control.

The wing has a very asymmetric radial twist distribution regardless of the level of harmonic control or advance ratio. The tip of the wing on the retreating side of the rotor (a normalized radial position of -0.5) has increasing twist with increasing r/R, with a maximum twist at a normalized radial position of about -0.3. The twist then decreases nearly linearly to a value near zero at the tip of wing on the advancing side of the rotor (a normalized radial position of 0.5). This asymmetric twist results in a net rolling moment, which is balanced by the rolling moment on the rotor generated from the rotor creating more lift on its advancing side. The fact that the rotor no longer has to maintain trim results in a more efficient circulation distribution and reduced power requirements compared to a single rotor.

Also of interest in Figures 6.3 and 6.4, the rubber rotor solution has lower levels of circulation and lift on the wing compared to the $N = 1$ and $N = 10$ solutions, indicating that the cases constrained by control schemes are forced to use a higher than optimal fraction of lift on the wing.

6.3 Nonlinear Programming Results

In this section, we present solutions to the nonlinear optimal blade control problem for the baseline wing-rotor configuration. The blade and wing analyzed use a NACA

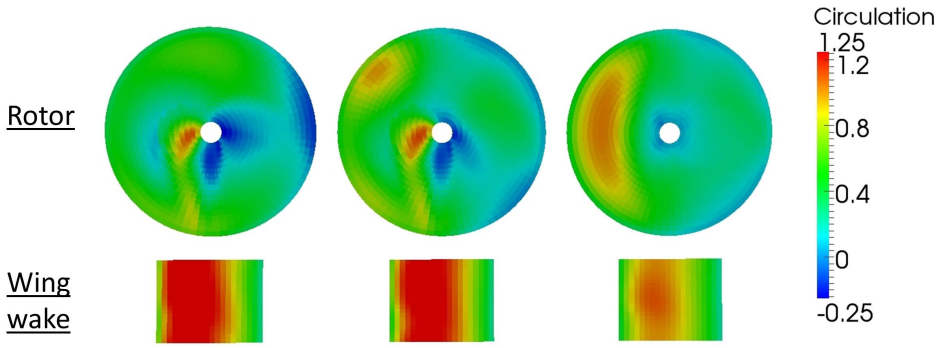

FIGURE 6.3: Optimal circulation distribution for a wing-rotor compound at $\mu = 0.5$, with rotor distribution shown above the wing wake, computed by QP method. Left: $N = 1$ control. Middle: $N = 10$ control. Right: Rubber rotor solution.

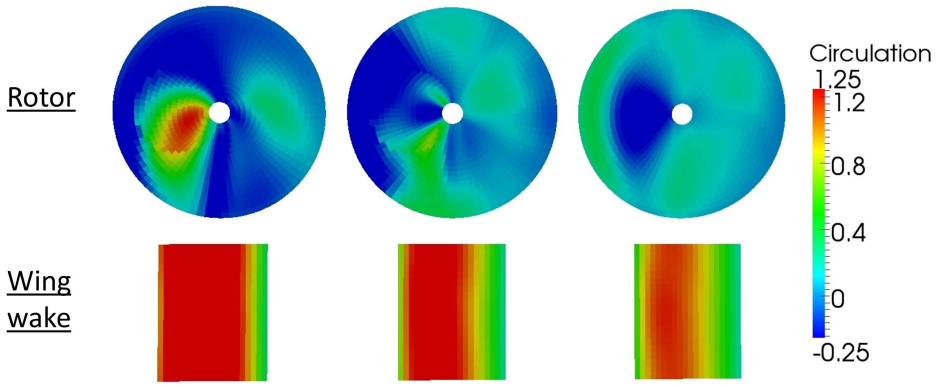

FIGURE 6.4: Optimal circulation distribution for a wing-rotor compound at $\mu = 0.8$, with rotor distribution shown above the wing wake, computed by QP method. Left: $N = 1$ control. Middle: $N = 10$ control. Right: Rubber rotor solution.

0012 airfoil from root to tip, with data of the coefficient of lift and drag through the full range of angles of attack obtained from Reference [39]. Again, the coefficient of lift is modified by Mach number using the Prandtl-Glauert transform, while the coefficient of drag is unchanged based on Mach number.

6.3.1 Comparison of Nonlinear Programming Results to Quadratic Programming Results

As discussed previously, the QP approach is extremely efficient compared to the Nonlinear Programming approach. As a result, it is a useful to compare the QP

results to NLP solutions using a fixed chord, to ensure that both methods generate a similar answer. The QP results for the single rotor given in Chapter 4 show a large discrepancy between the QP and NLP results at high advance ratios, where large effective angles of attack are required on the retreating side of the rotor, leading to differences between the two solutions. However, the wing-rotor compound is actually more similar to the coaxial case, as the wing provides its own rolling moment to balance the moment of the rotor, meaning that large pitch angles are not required on the retreating side of the rotor. As a result, the minimum power solutions for both the QP and NLP cases, seen in Figure 6.5, are in good agreement for the wing-rotor compound. Similar to the coaxial case, although not shown here, the computed minimum viscous power is slightly lower for the QP method, resulting in a slightly lower total power.

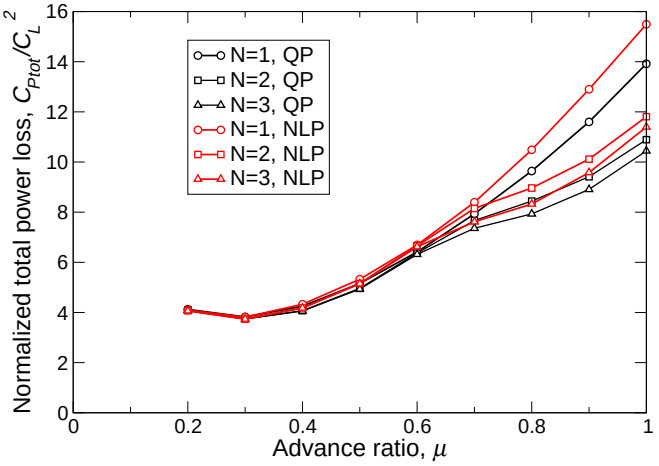

FIGURE 6.5: Minimum total power for the wing-rotor compound using a uniform chord distribution, as computed by the Quadratic Programming and Nonlinear Programming methods.

Additionally, as seen in Figure 6.6, the NLP optimal controls are very similar to the QP controls, even at high advance ratios, further indicating that the QP method results in a useful, efficient, and accurate approximation for the wing-rotor compound.

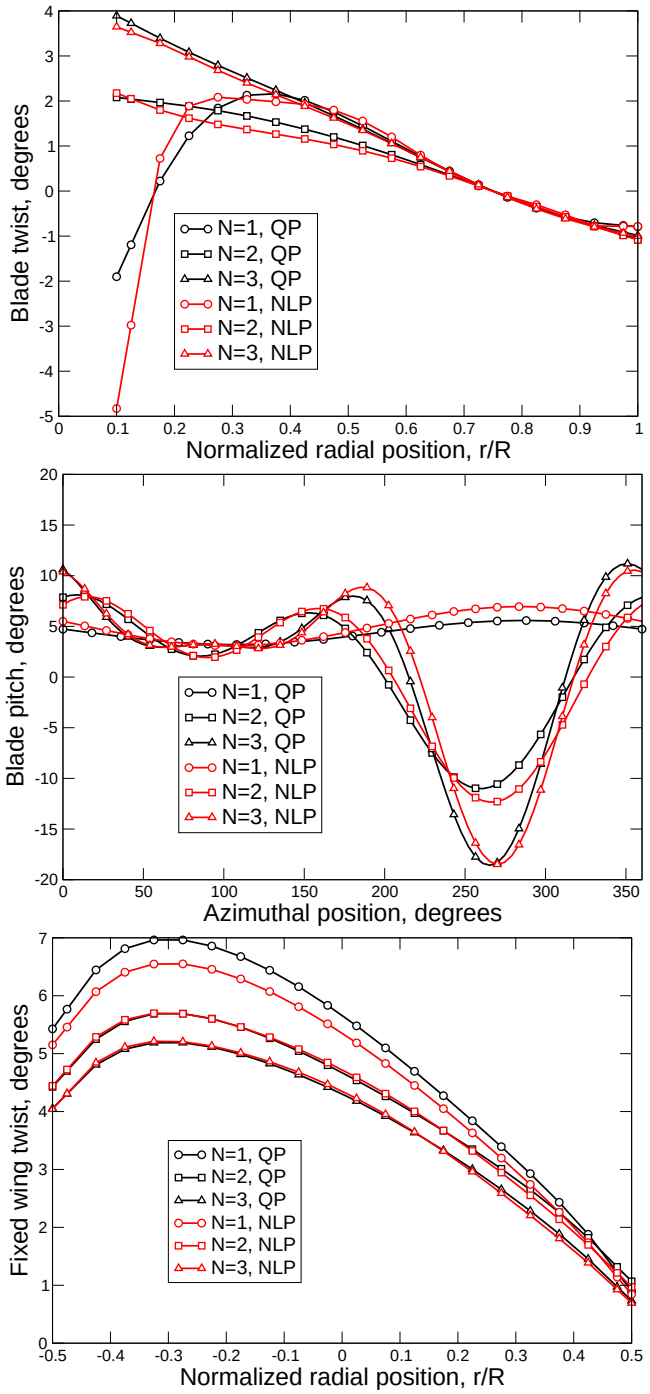

FIGURE 6.6: Comparison of optimal QP and NLP design variables at $\mu = 0.8$. Top: Blade twist. Middle: Pitch angle. Bottom: Wing twist.

6.3.2 Nonlinear Programming Results with Optimized Chord

In this section, we examine the reductions in power possible in the wing-rotor system when using an optimized chord distribution on both the rotor and the wing. Of course, the wing itself is a far more efficient generator of lift than the rotor system, so if possible, the optimization will minimize rotor chord and shift as much of the lift as possible to the wing. This solution, while very efficient, is not of interest, as the small blade areas would not be capable of hover or low speed flight and the optimization would essentially recover the optimal twist and chord distribution for a wing. To prevent this, the minimum modified thrust weighted solidity of the rotor is constrained to be $\sigma_{\mathrm{TWM}} = 0.08787$, the same modified thrust weighted solidity of the uniform chord single rotor investigated in Chapter 4. The chord on the wing is constrained only to remain positive, although in no case is this minimum chord constraint activated.

The top plot in Figure 6.7 shows the minimum total power for a wing-rotor compound using an optimized chord on both the wing and rotor compared to the same configuration using a uniform chord on both the wing and rotor. Also included is a plot of the minimum total power of a wing-rotor compound using a uniform chord, untwisted rotor and wing, to serve as a point of comparison. For this case, because the wing's radial twist is not optimized, the wing has a single degree of freedom, allowing it to set the uniform twist at all spanwise stations.

Optimizing the blade and wing chord distributions achieves a 40% reduction in power over the fixed chord case for $N = 1$ control at $\mu = 0.8$. To further investigate this large reduction in power, the induced and viscous components of power are also plotted in Figure 6.7, where we see that both the induced and viscous powers are both reduced by approximately 40%. Because the viscous power is nearly twice the induced power, this makes up the majority of the total power reduction. While for

the fixed chord case, higher harmonic control provides substantial power savings, for the variable chord case, $N = 3$ control only provides a 5% decrease in power at $\mu = 0.8$, and almost no improvement at lower advance ratios.

It is also useful to look at the optimal fraction of lift carried by the wing in the compound configuration, shown in Figure 6.8. Also plotted is the rubber rotor fraction of wing lift, i.e., the optimal fraction of lift generated by the wing without constraints on controls. At high advance ratios, the rubber rotor wing lift fraction is lower than any of the other cases. Use of higher harmonic control and/or chord optimization results in a reduced fraction of wing lift at high advance ratios that approaches (but never matches) the rubber rotor optimal. Note that for both the $N = 1$ uniform chord case and the untwisted, uniform chord case, the fraction of wing lift is actually greater than one at advance ratios above about $\mu = 0.7$, indicating that at these advance ratios, the rotor is actually generating negative lift. The reason for this can be understood by looking at the isolated rotor results in Chapter 4, that show that a fixed chord rotor with $N = 1$ control hits a rapid rise in total power at high advance ratios. As a result of the rotor's inefficiencies, the minimum power solution for these cases involves offloading the rotor as much as possible, even if it results in a negative lift from the rotor that must be compensated for by the wing.

Figure 6.9 shows the optimal radial twist and pitch input for the uniform and optimized chord cases at an advance ratio of $\mu = 0.8$. Similar to the coaxial case, the $N = 1$ cases use a large positive twist gradient at inboard portions of the blade, a feature that is less efficient than using the large reduction in blade pitch on the retreating side of the rotor seen in the $N = 3$ case. The wing twist of the variable chord case follows a similar pattern to the uniform chord case, but has a higher magnitude (between 3° and 7°) at all points.

As seen in Figure 6.10, the optimized wing planform has a much smaller chord than the baseline wing, with an average chord of 0.06 compared to 0.2857 for the

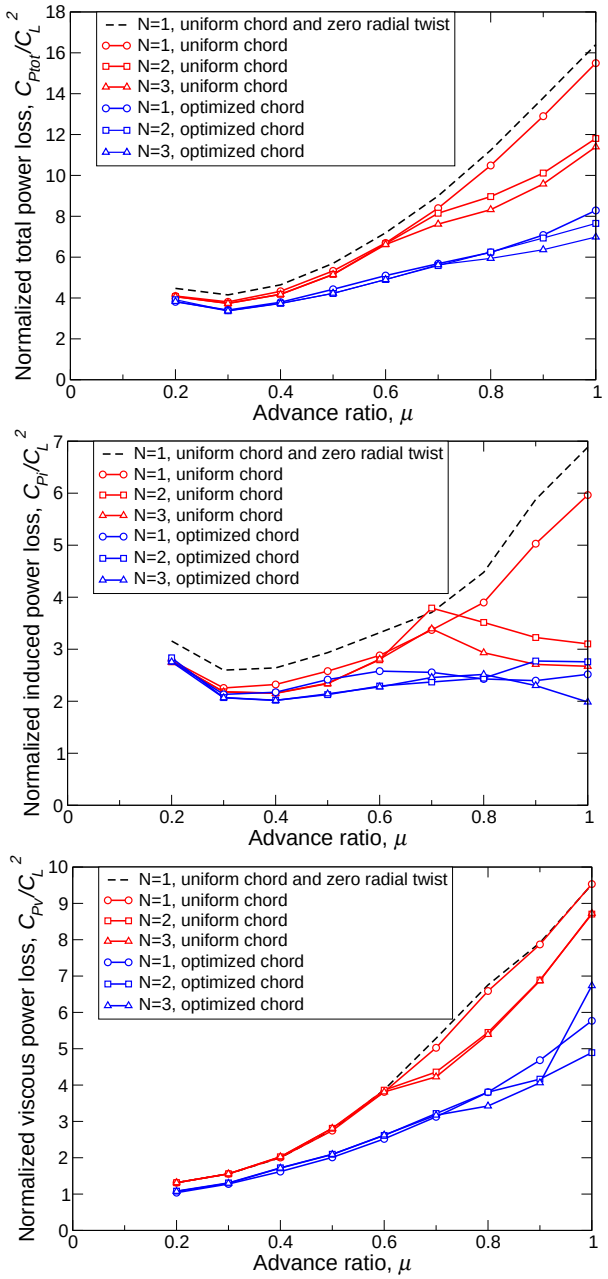

FIGURE 6.7: Top: Minimum total power loss for a wing-rotor compound with optimized wing and rotor chord distributions compared to a uniform chord case for varying levels of harmonic control. Middle and bottom: corresponding induced and viscous power components, respectively.

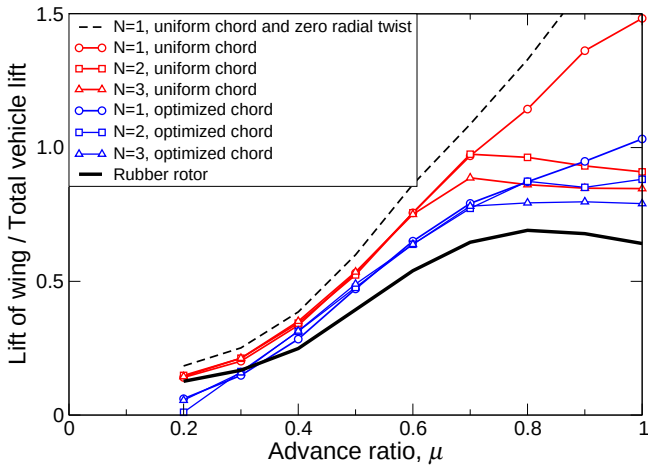

FIGURE 6.8: Optimal fraction of lift provided by the wing of compound helicopter with varying advance ratio.

baseline wing. This results in an aspect ratio of about 17, compared to 3.5 for the baseline wing. The decreased wing chord plays a large part in reducing viscous drag. Figure 6.10 also shows the optimal rotor planform for the $N = 1$ case, which has a very small inboard chord distribution with a large outboard chord. Note that as depicted in the figure, the blade does not extend to the full normalized radial position of 1; this is because the last panel of the vortex lattice grid is actually centered at a position of 0.975, and due to the large tapering of chord at the tip, there was no way to naturally extend the planform to include a position of 1. The $N = 3$ rotor planform looks significantly different from the $N = 1$ planform, with the majority of the blade area shifted inboard to form a more symmetric spanwise blade. The wing planform and twist is nearly the same regardless of the level of harmonic control.

Figure 6.11 shows the rotor's optimal circulation distribution at $\mu = 0.8$ for the $N = 1$ fixed and optimized chord cases. The fixed chord case contains a large region of positive circulation on the retreating side of the rotor, a result that is far from the rubber rotor optimum. The $N = 1$ variable chord case is able to mitigate this by moving nearly all of the chord to the outboard portion of the blade, resulting in very low circulations at inboard points and dramatically reducing the power. This

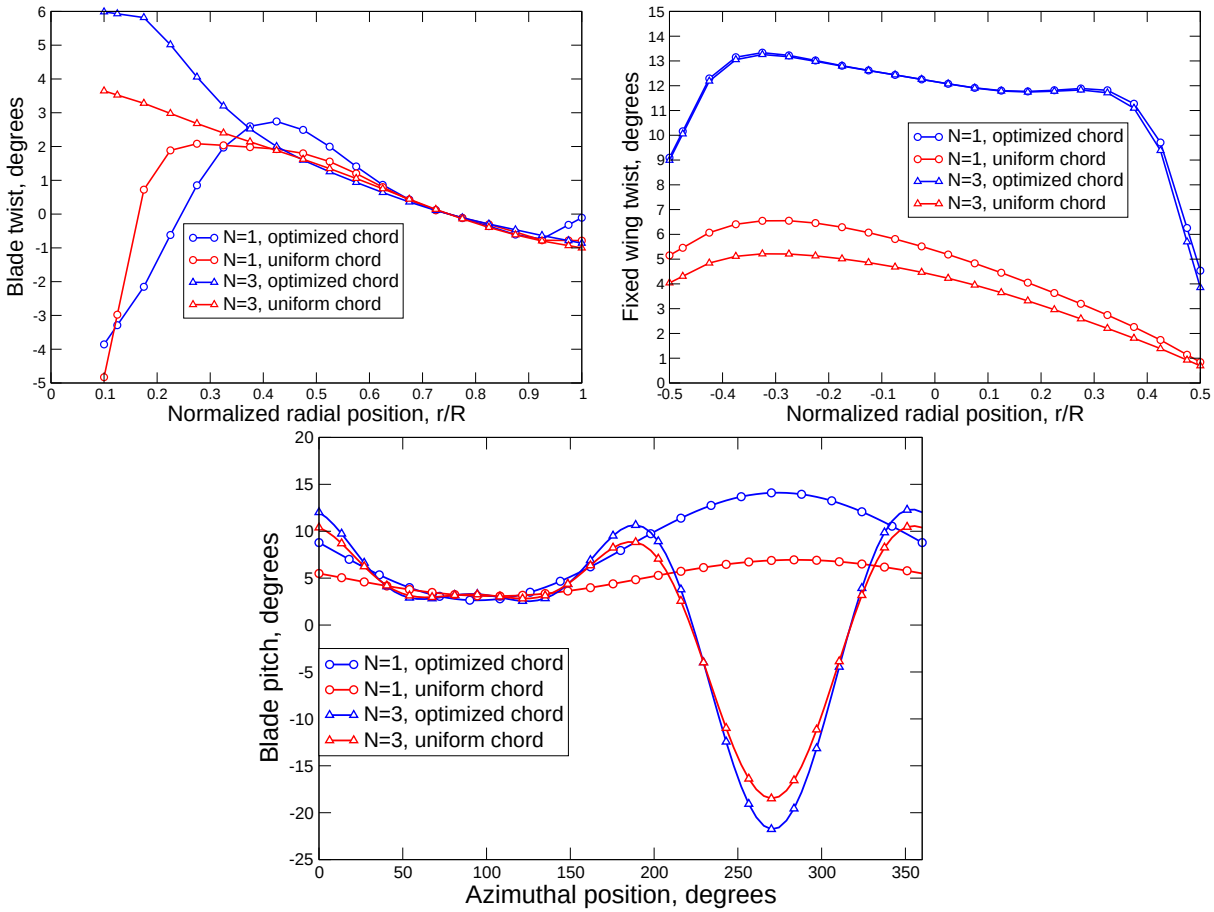

FIGURE 6.9: Optimal radial and azimuthal control inputs for a wing-rotor compound with optimized chord at $\mu = 0.8$. Top left: Optimal rotor twist. Right: Optimal wing twist. Bottom: Optimal azimuthal pitch input.

also has the effect of allowing the rotor to carry a larger fraction of the vehicle's lift, more closely approaching the rubber rotor fraction of wing lift.

6.3.3 Comparison of Viscous Optimum to Inviscid Optimum

It is instructive to look at the inviscid optimal solution, to get a better idea of what drives the viscous total power solution at each level of harmonic control. Table 6.1 gives the minimum powers for the inviscid and viscous optimizations at the high speed design point of $\mu = 0.8$. As expected, an increased level of harmonic control is effective at reducing the minimum induced power for the inviscid case. The $N =$

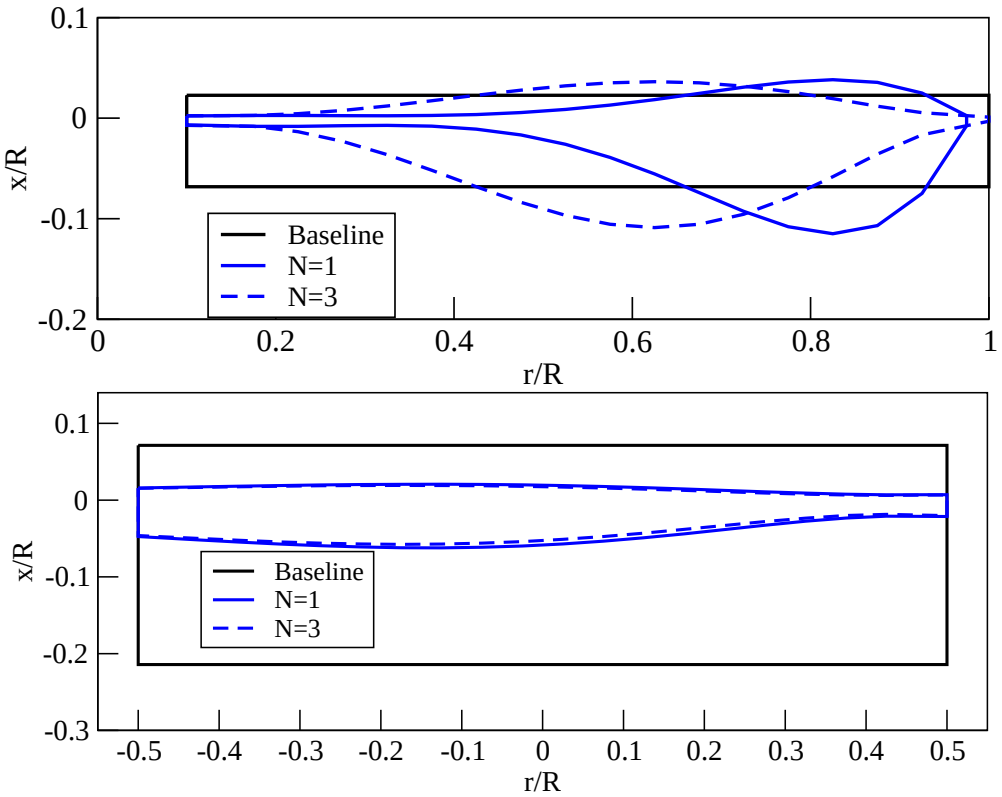

FIGURE 6.10: Top and bottom: Optimal rotor blade and optimal wing planform, respectively, for compound helicopter at $\mu = 0.8$.

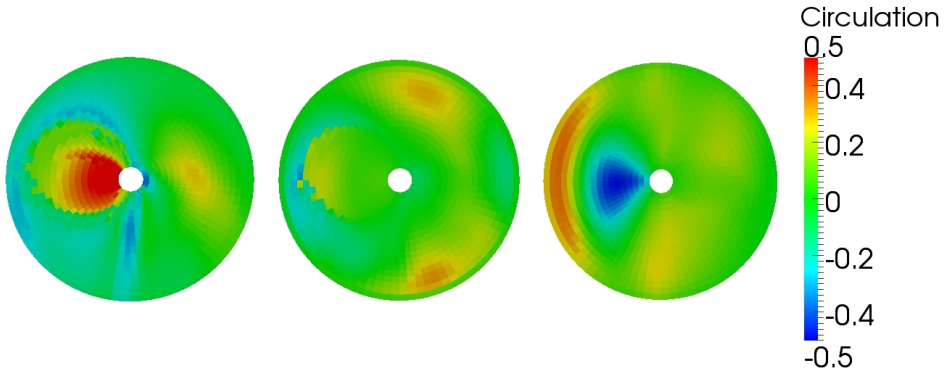

FIGURE 6.11: Optimal circulation distribution on rotor of a wing-rotor compound at $\mu = 0.8$ with fixed and optimized chord distributions. Left: $N = 1$ control with fixed chord. Middle: $N = 1$ with optimized chord. Right: Rubber rotor solution.

1 viscous optimum has nearly the same induced power as the inviscid optimum, indicating that the solution is based on minimizing induced power. Indeed, the plot of rotor twist and azimuthal input in Figure 6.12 shows that the $N = 1$ solutions are very similar. The viscous optimization achieves viscous power reductions while maintaining nearly the same induced power primarily through the use of slightly modifications to the blade and wing planforms and rotor twist on the inboard portion of the blade. The $N = 3$ viscous and inviscid cases feature similar rotor twist distributions but drastically different pitch inputs, particularly on the retreating side of the rotor between $\psi = 230°$ and $\psi = 330°$. The viscous solution has a different pitch input because of the high viscous power associated with the very large increase in pitch ($\approx 40°$) in this area present in the inviscid solution.

Table 6.1: Induced, viscous, and total power at $\mu = 0.8$ for inviscid and viscous optimal solutions of the compound rotor.

	N=1		N=2		N=3	
	Inviscid design	Viscous design	Inviscid design	Viscous design	Inviscid design	Viscous design
Induced power, C_{Pi}/C_L^2	2.42	2.43	2.21	2.44	2.12	2.51
Viscous power, C_{Pv}/C_L^2	4.25	3.80	4.87	3.80	4.98	3.42
Total power, C_{Ptot}/C_L^2	6.67	6.23	7.09	6.25	7.10	5.94

6.3.4 Effect of Varying Wing Span

All of the above cases use a wing with span equal to the radius of the rotor, similar to the Cheyenne helicopter. Figure 6.14 shows the minimum total, induced, and viscous powers for a wing-rotor compound at $\mu = 0.5$ with varying wing span. An increased wing span leads to a decrease in total power, which is expected given that a wing is a more efficient generator of lift than a rotor in forward flight. At wing spans greater than about 1.5 times the rotor radius, the viscous power increases with increasing wing span; however, the corresponding decrease in induced power is greater, resulting in the larger span wing having a lower total power. At some

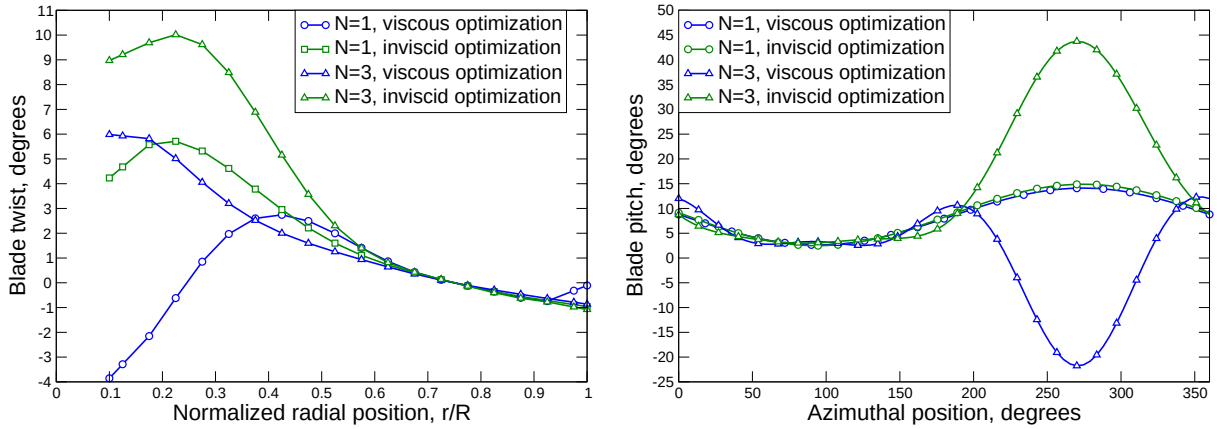

FIGURE 6.12: Optimal radial and azimuthal control inputs for wing-rotor compound using viscous and inviscid optimizations at $\mu = 0.8$. Left: Optimal radial rotor twist. Right: Optimal azimuthal pitch.

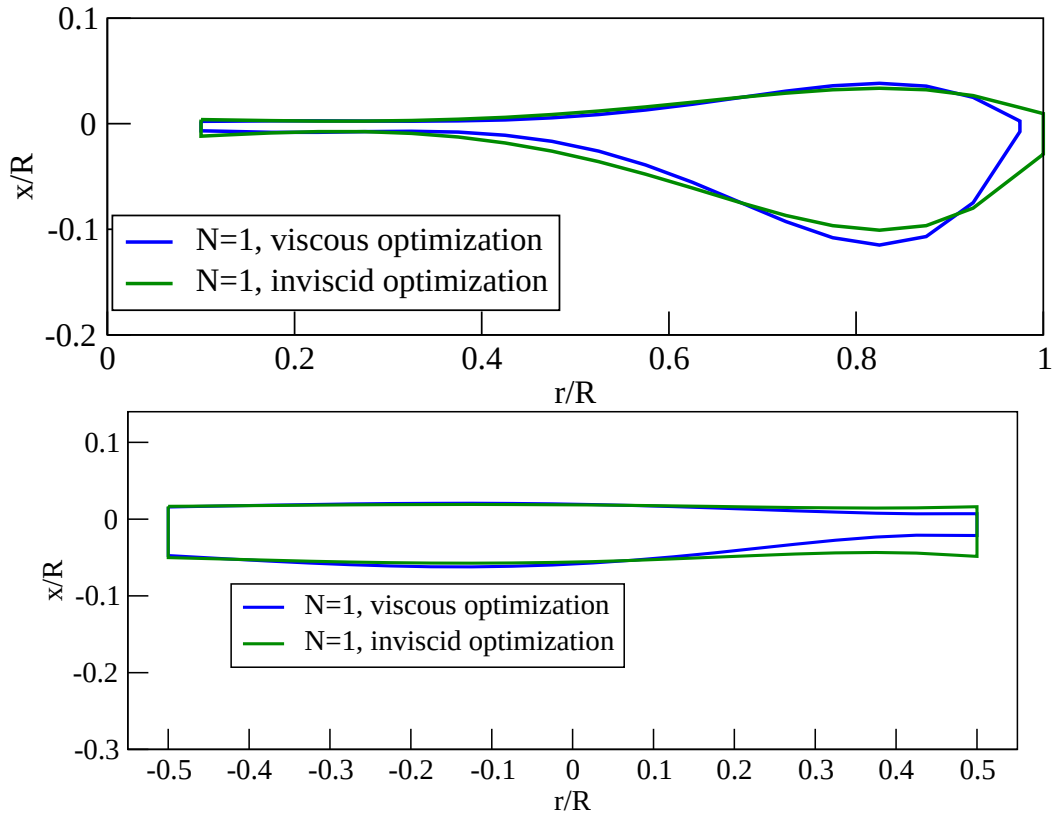

FIGURE 6.13: Top and bottom: Optimal inviscid and viscous blade and optimal wing planform, respectively, for compound helicopter at $\mu = 0.8$. Note the varying scales between the two plots.

given span (not shown in the plot), the viscous power increase will outweigh the reduction in induced power, and there will be an optimal span. However, given that the cases have only a nominal constraint on chord (a minimum value of 1% of rotor radius), the resulting aspect ratios are unrealistically high, and the true viscous drag of these wings with the chord required for structural considerations is not accounted for. A more in-depth analysis could place a more rigid constraint on wing chord to determine the optimal wing span in forward flight.

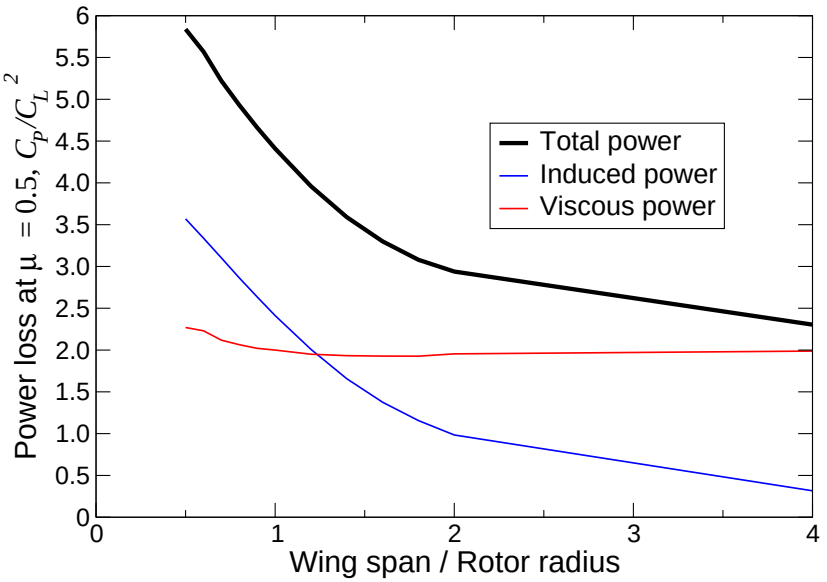

FIGURE 6.14: Total, induced, and viscous power at $\mu = 0.5$ for a compound helicopter with varying wing spans, using $N = 1$ control.

6.3.5 Single Point Optimization

The previous results showed the minimum power solution with every design variable optimized at each advance ratio. Similar to the coaxial case, it is interesting to see what kind of performance gains are available if constrained to use a single blade and wing planform and radial twist across all advance ratios, while changing only the azimuthal pitch inputs, as would likely be the case in the real design of a rotor and wing.

Figure 6.15 shows the minimum total power for a wing-rotor compound using the optimal blade and wing design from the $\mu = 0.5$ and $\mu = 0.8$ optimizations across a range of advance ratios. This single point optimization was performed for both $N = 1$ and $N = 3$ harmonic control. The minimum power values for the single point case are compared to the minimum total power for a rotor and wing designed specifically for each advance ratio. Also included is the minimum total power for a wing-rotor compound using the baseline rotor and wing planforms (each rectangular) and zero radial twist. For both $N = 1$ and $N = 3$ control, the $\mu = 0.5$ design achieves a total power that is very close to the minimum power rotor at low advance ratios, and performs progressively worse than the minimum power rotor as advance ratio increases. At all advance ratios, the $\mu = 0.5$ design performs significantly better than the baseline untwisted design. Also of note, with $N = 3$ harmonic control, the $\mu = 0.5$ design is able to maintain powers closer to the minimum power rotor at high advance ratios, indicating that higher harmonic control adds extra benefit when constrained to a single blade and wing design. The $\mu = 0.8$ controls show a similar pattern, with powers close to the minimum power rotor at advance ratios near $\mu = 0.8$ and with significantly higher powers that the minimum power rotor at low advance ratios. In fact, for both $N = 1$ and $N = 3$ control, the $\mu = 0.8$ design has flight conditions at low advance ratios where it performs worse than the baseline untwisted rotor and blade.

6.3.6 Use of an Off-centered Wing

The optimal solutions all have an asymmetric twist distribution on the wing, with larger fixed twists on the retreating side of the rotor. Additionally, the optimized chord is asymmetric, with increased wing area on the retreating side of the rotor. Both of these features allow the wing to generate increased lift in this area, creating a rolling moment to balance the rolling moment of the rotor. This suggests that

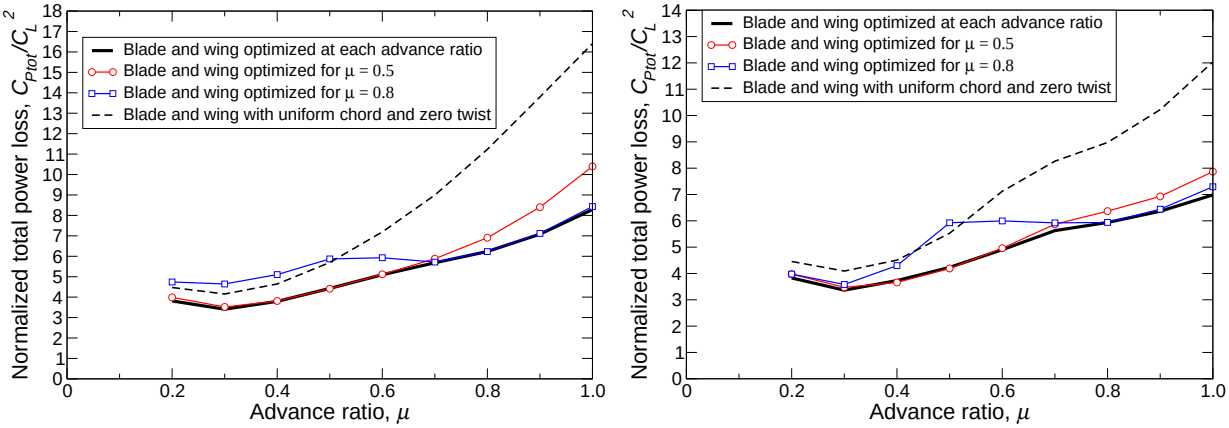

FIGURE 6.15: Minimum total power using $\mu = 0.5$ and $\mu = 0.8$ optimal blade design across a range of advance ratios. Left: with $N = 1$ control. Right: with $N = 3$ control.

perhaps an off-centered wing, with an increased span on the retreating side of the rotor such as in the configuration shown at right in Figure 6.16, may decrease power requirements relative to a centered wing.

Figure 6.17 shows the minimum total, induced, and viscous power for a wing-rotor compound using a wing shifted by varying amounts to the retreating side of the rotor at advance ratios of $\mu = 0.5$ and $\mu = 0.8$. In all cases, the wing has a span equal to the rotor's radius, and the rotor uses $N = 1$ harmonic control. The abscissa shows the fraction of the wing located on the retreating side of the rotor; a value of 0.5 indicates a centered wing, and a value of 1 indicates a wing located entirely on the retreating side. As the fraction of the wing located on the retreating side of the rotor increases, the required power decreases monotonically. For a wing shifted entirely to the retreating side of the rotor, there is a 23% reduction in total power compared to a centered wing at $\mu = 0.5$. At an advance ratio of $\mu = 0.8$, there is a similar reduction in total power of 20% with a wing shifted entirely to the retreating side of the rotor. In each case, this large reduction in total power is achieved primarily through reductions in induced power, although viscous power is also reduced slightly with an increasingly off-centered wing.

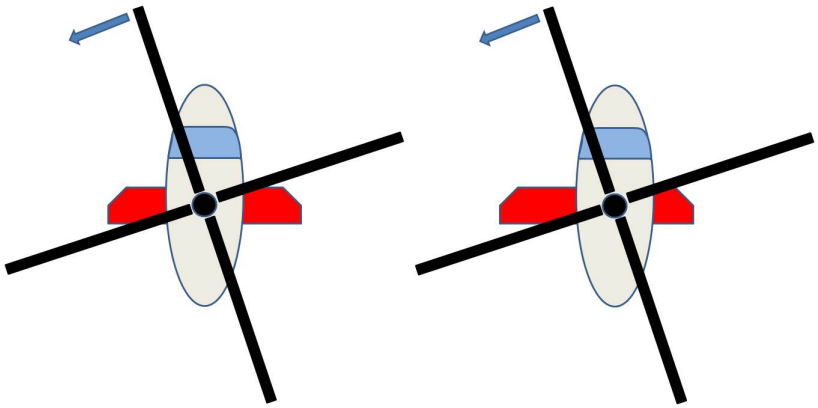

FIGURE 6.16: Graphic of a wing-rotor compound using an off-centered wing. Left: Centered wing. Right: Wing shifted to retreating side of the rotor. This figure is not to scale.

Note that the shifted wing only provides an advantage if wings of the same span are compared. Simply removing a section of wing from the advancing side, thereby decreasing the wing span, does not provide a power reduction, as the reduction in viscous power due to the removed wing is more than negated by the resulting increase in induced power. The off-centered wing analyzed would provide an advantage if total wing span was limited by weight considerations, and a wing of a given span were to be placed to maximize efficiency in forward flight. These results also suggest that the use of an extendable or folding wing on the retreating side of the rotor that could be used to increase span asymmetrically at high speeds would be effective in reducing power requirements.

6.4 Conclusions from Analysis of a Conventional Rotor with a Lifting Wing

Based on the analysis of the conventional rotor with a lifting wing (wing-rotor compound), we can draw the following specific conclusions:

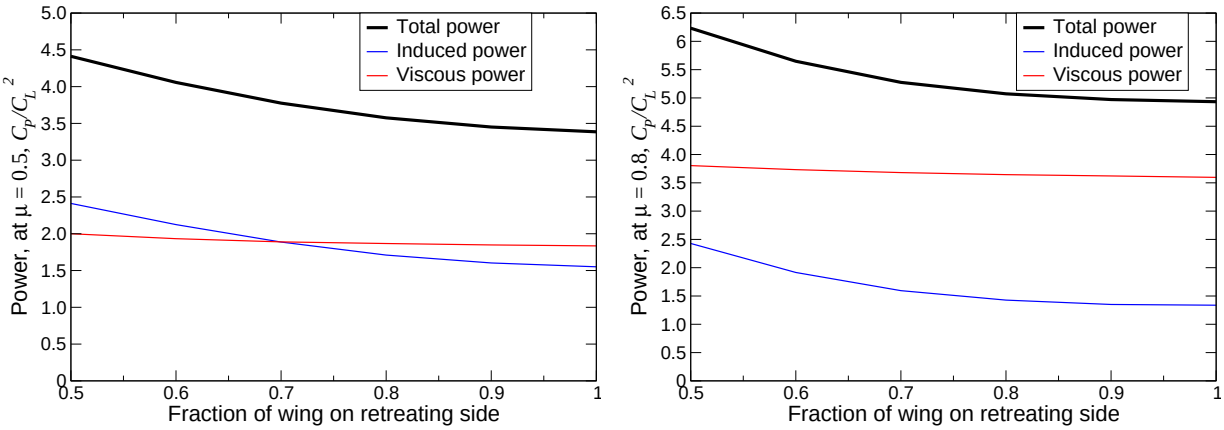

FIGURE 6.17: Total, induced, and viscous power for a compound helicopter using an off-centered wing and $N = 1$ harmonic control. Left: at an advance ratio of $\mu = 0.5$. Right: at an advance ratio of $\mu = 0.8$.

1. The quadratic programming method provides for an accurate approximation of optimal rotor design and minimum power requirements for the optimization of a fixed blade chord. The method is computationally fast, requiring only several minutes for each flight condition, and produces a solution that is very close to the more accurate NLP method.

2. Higher harmonic control is an effective method of decreasing total power at advance ratios above $\mu = 0.6$ for the uniform chord case, with $N = 2$ and $N = 3$ control providing a 14% and 21% reduction in total power, respectively, compared to the $N = 1$ case at an advance ratio of $\mu = 0.8$.

3. Optimizing the chord distribution of the rotor and wing provides even larger reductions in total power compared to the baseline uniform chord case. For $N = 1$ control, optimizing the chord distribution of both the wing and rotor provides a 40% reduction in total power compared to the uniform chord case at $\mu = 0.8$. This large reduction in power is achieved through reductions in both induced and viscous powers.

4. The power reductions available with the use of higher harmonic control are more

modest when using an optimized chord distribution (in addition to optimized radial twist and azimuth pitch inputs). At $\mu = 0.8$, $N = 3$ control provides a 5% improvement compared to $N = 1$ control.

5. The rubber rotor optimal fraction of lift provided by the wing increases with increasing advance ratio up to an advance ratio of $\mu = 0.8$, at which point it decreases. When constrained to a specific set of design variables, the wing fraction of lift is higher than the rubber rotor optimal, resulting in higher total power. Use of higher harmonic control and/or chord optimization serves to increase the amount of lift provided by the rotor, bringing it closer to the rubber rotor optimal lift fraction and decreasing the total power.

6. The optimal viscous solution is driven by induced losses, even for the variable chord case.

7. Given the high aspect ratio wings allowed in this analysis, increasing wing span decreases total power. This reduction in total power is achieved through a reduction in induced power, which makes up for the higher viscous powers that result from an increased span wing.

8. For a given wing span, as more of the span is shifted to the retreating side of the rotor, the total power is decreased. A wing located entirely on the retreating side of the rotor results in an approximately 20% reduction in total power versus a centered wing of the same span at advance ratios of $\mu = 0.5$ and $\mu = 0.8$.

7

Conclusions

7.1 Summary and Conclusions

This thesis presents two methods for determining the optimal design of conventional, compound, and coaxial rotors in forward flight using higher harmonic control. In the first method, known as the quadratic programming (QP) method, the sectional blade aerodynamics are modeled using a linear lift curve and a quadratic drag polar, and flow angles are assumed to be small. The result is a quadratic programming problem that yields a linear set of equations to solve for the unknown optimal design variables and control inputs. In this method, the chord distribution can not be included as a design variable to be optimized. The second method, known as the nonlinear programming (NLP) approach, makes use of a Newton iteration to solve the fully non-linear variational problem. This method accounts for nonlinear lift curves, non-quadratic drag polars, accurately models large flow angles, and is capable of including blade chord as a design variable.

The two methods are capable of analyzing nearly any arbitrary control scheme: in this thesis, we evaluate the use of conventional and higher harmonic blade root

control as a means of reducing the total power requirements. We evaluated these control schemes for three rotor configurations: a conventional single rotor, a coaxial counter-rotating configuration, and a conventional rotor using a lifting wing.

The QP method is computationally very fast, computing a given flight condition in several minutes on a single processor machine compared to several hours for the NLP method. The results from the QP method are accurate and in good agreement with the more complex NLP method for the compound and coaxial configurations. The QP method slightly underpredicts the viscous power in these configurations, but the minimum induced and total powers are very similar, and the optimal radial twist and azimuthal pitch inputs are also in good agreement between the two methods. For a conventional rotor, the two methods agree well at low advance ratios, but have significant discrepancies in the computed minimum power at higher advance ratios (greater than $\mu = 0.4$). This is a result of the conventional configuration requiring high angles of attack on the retreating side of the rotor to maintain roll trim. The way in which the two methods treat the sectional coefficient of lift at these high angles differs between the two methods; the QP approach assumes a linear lift curve while the NLP approach uses realistic lift curve data that accounts for stall. This difference in high angle of attack modeling results in significant differences in minimum power between the two methods. Despite this, the results are in better agreement for N=2 and N=3 harmonic control, where the optimal controls do not require such severely large angles of attack.

Results show that higher harmonic control provies significant power reductions in each of the three configurations. The reductions in power are largest at high advance ratios. In general, the benefit of higher harmonic control has rapidly diminishing returns above the N=3 level of control. At an advance ratio of $\mu = 0.8$, and using an optimized chord distribution and radial twist in all cases, use of N=3 harmonic control results in a 25% decrease in total power (compared to $N = 1$ control) within

the single rotor configuration, a 13% decrease in total power for the coaxial rotor configuration, and a 5% decrease in total power for the wing-rotor compound. If other constraints are implemented, for example use of more restrictive chord constraints or a lift offset constraint in a coaxial rotor system, the relative benefits of higher harmonic control increase. Additionally, higher harmonic control improves the performance of a given blade design at off-design advance ratios.

Optimizing the blade and/or wing planform also provides large reductions in power compared to the baseline, rectangular planform for each configuration. The aerodynamically optimal blade planform can differ signficantly from the baseline rotor, often making use of extremely small chord values at inboard stations as a means of reducing power. The resulting blade would be unlikely to meet structural requirements in the actual design of a rotor. The example problems in this thesis constrained the minimum chord value to be 1% of the rotor radius at all spanwise stations on the blade. More restrictive minimum chord constraints can be used as necessary to satisfy any structural constraints and produce a more practical blade design.

The methods developed can perform both inviscid (minimizing induced power) and viscous (minimizing the sum of induced and viscous power) optimizations. For nearly all configurations and flight speeds, the induced power is a significant driver in the viscous optimization problem. Thus, the circulation distributions, optimal radial twist, azimuthal pitch inputs, and planforms for the viscous and inviscid cases are very similar. The viscous optimized solution trades some amount of this induced power for reductions in viscous power, but generally maintains most of the features of the inviscid optimal solution.

For the coaxial and compound cases, performing a single point optimization yielded encouraging results. The radial twist and planform of the rotor and, in the case of the compound configuration, the wing, were optimized at a single ad-

vance ratio. The blade and wing were then held fixed and the root pitch inputs were optimized at each advance ratio to maintain trim and provide the required lift. As expected, the single point designs resulted in higher total power at off-design points than the case where all design variables were optimized at every flight condition. However, this increase in power tended to be small, and in almost all cases the single point optimal blade, designed at a single advance ratio, resulted in lower power than a rectangular, untwisted blade across all advance ratios. Additionally, higher harmonic control significantly reduces the power required at off-design points, making the off-design total power much closer to the minimum power achievable with all design variables optimized at all speeds. This is an encouraging result, as clearly a realistic design would require a single blade planform and radial twist to be used at all speeds. Additionally, this indicates that higher harmonic control is effective at improving performance for a given rotor or wing design at off-design points.

For the coaxial configuration, we require the net rolling and pitching moment of the rotor system to be equal to zero. Each individual rotor, however, will produced non-zero rolling and pitching moments. The ability to use this lift offset, which is the radial location of the center of lift on each rotor, is the primary advantage of the coaxial configuration. Using a high lift offset allows for the offloading of each rotor on the retreating side, where the geometric angle of attack changes rapidly as the blade enters and exits the reverse flow region. The present analysis shows that at high speeds, a lift offset as high as 0.5 is optimal. If the maximum lift offset is constrained, as may be necessary in the actual design of a rotor due to structural limitations on the hub, the use of higher harmonic control produces a much larger reduction in total power than in the case where lift offset is unconstrained. In other words, constraining the lift offset imposes a higher penalty for a rotor with N=1 control than with N=2 or N=3 control. This indicates that higher harmonic control may be of even further benefit in the design of a lift offset constrained rotor, as in

the X2 TD design, where a maximum value of 0.3 is used.

Within the wing-rotor compound, use of an off-centered wing also reduces significantly the required power at high speeds. For a given wing span, as more of the span is shifted to the retreating side of the rotor, the total power decreases monotonically. A wing located entirely on the retreating side of the rotor results in a 20% redicton in total power compared to a centered wing of the same span at advance ratios of $\mu = 0.5$ and $\mu = 0.8$.

Figure 7.1 shows the minimum total power for each of the three configurations, using N=3 harmonic control and with optimized chord, with all design variables optimized anew at each advance ratio. This is meant to represent a value very close to the minimum total power in each configuration when using higher harmonic blade root control. The coaxial rotor is the most efficient configuration at all advance ratios, while the wing-rotor compound produces very large reduction in power relative to the conventional rotor.

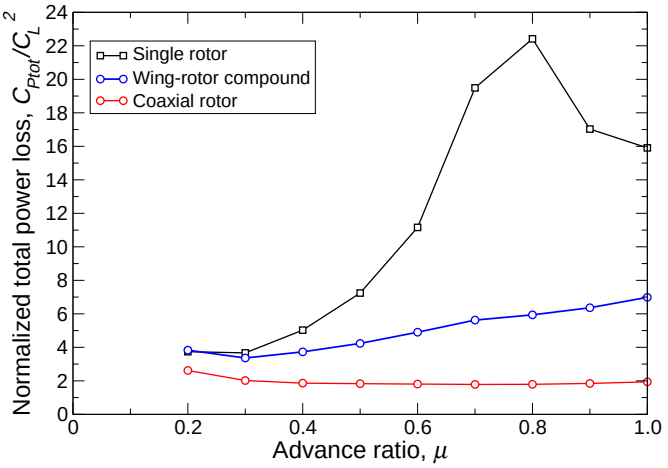

FIGURE 7.1: Comparison of minimum total power for conventional rotor, coaxial rotor, and wing rotor compound. All cases use N=3 harmonic control and an optimized chord distribution.

7.2 Future Work

The goal of the three cases examined in this thesis was to determine fundamental rotor design characteristics that improve high speed performance. As a result, the exploration of parameters was fairly limited in scope. However, the effect of other parameters on performance will be investigated, including rotor solidity, the use of blade sweep, and the use of anhedral tips. Additionally, further compound configurations, such as coaxial rotors used in addition to a wing, will be analyzed to determine potential performance benefits with and without higher harmonic control.

Another interesting area to investigate includes incorporating auxiliary propulsion into the model. Rather than constraining lift only, we will also constrain a thrust (representing an approximation of fuselage drag) and include a source of auxilliary propulsion (such as one or more propellers) into the model. With this additional constrained force, the shaft angle of attack can be varied in order to investigate the optimal thrust balance between the rotor system and the auxiliary propulsion system, and to determine how optimal rotor and propeller design are affected by shaft angle.

There are also several improvements that will be made to the model to improve its accuracy. C-81 tables will be implemented to more accurately reflect the change in coefficient of lift and drag with Mach number. A lifting surface, rather than lifting line model, will be used to account for effects due to lags in the development of circulation. A dynamic stall model (such as the ONERA model) will also be implemented, to include dynamic effects which may play a role in the fast actuation of the blades seen in many of the optimal solutions.

Finally, we will couple the model with a hover analysis and perform a multi-point optimization. The hovering flight regime typically has conflicting design requirements with high speed flight, and performing a formal optimization will lead to insight into

design features that provide the best aerodynamic performance across these two diverse flight conditions.

Appendix A

Mathematical Programming via Augmented Lagrangians

A.1 Motivation

In Section 3.3.2, we outlined a nonlinear approach for finding the circulation distribution, forces, moments, and power loss due to a given set of geometric design variables. To determine the design variables that result in the minimum power loss while satisfying constraints on lift and moments, we must solve a nonlinear constrained optimization problem. Section 3.4 describes a method of solving this problem using Newton Iteration. In this Appendix, we present a second method of solving the nonlinear constrained optimization problem using Mathematical Programming via Augmented Lagrangians. This method recasts the constrained optimization problems as a series of unconstrained minimization problems. Each unconstrained problem is solved using the Broyden–Fletcher–Goldfarb–Shanno (BFGS) variable metric method [8], with the Lagrange multipliers updated at each iteration. This process is also detailed in Reference [6], and much of the work in applying the optimization method to this particular problem is derived from Reference [15].

A.2 Defining cost function and equality constraints

First, we define the cost function to be minimized. Quadratic penalty functions are added to the equality constraints on lift and moments, which tends to move the computed solution closer to satisfying the constraints. Note that these constraints are nonlinear, as they depend on the circulation distribution, which is nonlinearly related to the vector of design variables. For the simplified case with a single lift constraint and a single moment constraint, the cost function with quadratic penalty functions is

$$\Pi = P + \lambda_F(F - F_R) + \frac{1}{2}W_1(F - F_R)^2 + \lambda_M(M - M_R) + \frac{1}{2}W_2(M - M_R)^2 \quad \text{(A.1)}$$

where W_1 and W_2 are positive penalty weights and P represents the total power loss, which in turn is equal to the sum of the induced and profile power losses. The factors of $\frac{1}{2}$ have been added for convenience.

The BFGS variable metric method requires the gradients of the Lagrangian cost with respect to the vector of control inputs to determine a search direction at each step. The gradient of the Lagrangian cost function will be a vector of size h, i.e., the size of the vector of design variables to be optimized. The gradient of the simplified cost function shown in Equation (A.1) is

$$\nabla_{\boldsymbol{\Theta}}\Pi = \nabla_{\boldsymbol{\Theta}}P + \lambda_F\nabla_{\boldsymbol{\Theta}}F + W_1(F - F_R)\nabla_{\boldsymbol{\Theta}}F + \lambda_M\nabla_{\boldsymbol{\Theta}}M + W_2(M - M_R)\nabla_{\boldsymbol{\Theta}}M \quad \text{(A.2)}$$

The gradients in Equation (A.2) are calculated using adjoint automatic differentiated code generated with the compiler Tapenade [18]. This technique of adjoint automatic differentiation will be discussed in further detail in Section A.6.

Note that this optimization problem could also be formulated without any Lagrange multipliers, instead making the weight functions arbitrarily large and ensuring that any deviation from the required values of force or moment will not be a mini-

mum of the cost function. However, this technique would not work efficiently for the gradient based search method used. The large weights associated with the penalty functions would result in the vector of design variables quickly navigating to a location in the space that satisfies the constraints. However, depending on the starting point of the optimization, this would likely not be a minimum in terms of power. The search algorithm would then have to navigate to a minimum while satisfying the constraints at every step. The curvature along the constraints will be small compared to the curvature perpindicular to the constraints, making it very difficult and time consuming to locate the minimum. For simplicity, we can imagine the minimization problem as being two dimensional, with variables on the x and y axes, and the z axis indicating the function's value. In this case, the large weights implemented in the cost function can be thought of as creating deep valleys with very steep walls in the space, at the bottom of which are locations that satisfy (or nearly satisfy) the constraints. The optimization routine would quickly navigate to the bottom of one of these valleys, and then be forced to take very small, incremental steps along the floor of the valley to locate the true minimum. The method of augmented Lagrangians allows for the use of less severe penalty functions, as the Lagrange multiplier is iteratively updated to gradually satisfy the constraints, and is therefore a much more efficient method of locating the minimum.

A.3 Unconstrained optimization using the BFGS method

Each successive unconstrained minimization of Equation (A.1) is solved using the BFGS method. The BFGS method is a quasi–Newton technique, meaning that an approximated Hessian matrix of second derivatives is successively updated at each iteration, using calculated first derivatives and the previous step in design variables. If the exact Hessian matrix were known, it would be possible to take an exact Newton–Raphson step at each iteration, avoiding the errors inherent in approximating the

Hessian. However, computing the exact Hessian matrix for this problem, either via automatic differentiation or a finite differencing method, is prohibitively expensive computationally. The BFGS method has the following basic algorithm, with k indicating the iteration number:

1. Begin the iteration at some initial guess of the vector of design variables.

2. Make an initial approximation of the Hessian matrix. The identity matrix is typically used for the initial guess.

3. Compute the gradient of the augmented cost function $\mathbf{g}_k$ at this initial set of controls.

4. Compute the search direction:

$$\mathbf{d}_k = -\mathbf{H}_k \mathbf{g}_k \tag{A.3}$$

5. Take a step in the search direction, defined by

$$\mathbf{\Theta}_{k+1} = \mathbf{\Theta}_k + c\mathbf{d}_k \tag{A.4}$$

   The step size c is determined using the Armijo step size rule, described in Section A.5.

6. Calculate the gradient at the new set of controls, $\mathbf{\Theta}_{k+1}$. This updated gradient is denoted $\mathbf{g}_{k+1}$.

7. Defining $\mathbf{\Delta g}_k = \mathbf{g}_{k+1} - \mathbf{g}_k$ and $\mathbf{\Delta\Theta} = \mathbf{\Theta}_{k+1} - \mathbf{\Theta}_k$, update the matrix $\mathbf{H}$ as follows:

$$\begin{aligned}\mathbf{H}_{k+1} = \mathbf{H}_k + \left\{1 + \frac{\mathbf{\Delta g}_k^T \mathbf{H}_k \mathbf{\Delta g}_k}{\mathbf{\Delta\Theta}_k{}^T \mathbf{\Delta g}_k}\right\} \frac{\mathbf{\Delta\Theta}_k \mathbf{\Delta\Theta}_k{}^T}{\mathbf{\Delta\Theta}_k{}^T \mathbf{\Delta g}_k} \\ - \frac{\mathbf{H}_k \mathbf{\Delta g}_k \mathbf{\Delta\Theta}_k{}^T}{\mathbf{\Delta\Theta}_k{}^T \mathbf{\Delta g}_k} - \frac{\mathbf{\Delta\Theta}_k \mathbf{\Delta g}_k{}^T \mathbf{H}_k}{\mathbf{\Delta\Theta}_k{}^T \mathbf{\Delta g}_k}\end{aligned} \tag{A.5}$$

8. Return to step 3 and iterate until the minimum is found.

After each unconstrained minimization problem is solved, the Lagrange multipliers are updated as follows:

$$\lambda_{F\,\text{new}} = \lambda_{F\,\text{old}} + W_1(F - F_R)$$
$$\lambda_{M\,\text{new}} = \lambda_{M\,\text{old}} + W_2(M - M_R) \tag{A.6}$$

The new unconstrained minimization problem including the updated multipliers is then solved. This process is repeated until the Kuhn-Tucker conditions are satisfied [23], indicating that a constrained minimum has been reached and the optimal design variable vector $\mathbf{\Theta}$ has been found.

A.4 Inequality Constraints

The previous simplified example included equality constraints on forces and moments. As described in Section 3.4.6, it is often usefl to apply a set of inequality constraints on the chord distribution.

While the equality constraints on forces and moments are scalar, the inequality constraint $\mathbf{C}$ is a vector quantity. As written here, this constraint is a minimum chord constraint. Note that by reversing the sign of the constraint, a maximum chord constraint can be implemented using the same approach. The entries of this vector for the constraint on minimum chord are given by

$$C_i = c_i - c_{\text{min}i} \geq 0 \tag{A.7}$$

where c_i is the value of the chord at the i^{th} station and $c_{\text{min}i}$ is the minimum allowable chord at this station. Leaving out the equality constraints for simplicity, the augmented cost function with this inequality constraint is then

$$\Pi = P + \boldsymbol{\lambda}_c{}^T\mathbf{C} + \frac{1}{2}W_3\sum_i^M \frac{(C_i - |C_i|)C_i}{2} \tag{A.8}$$

where W_3 is a weight coefficient. Note that if the inequality constraint at the i^{th} radial station is active, i.e., the chord is below the minimum value, the term $(C_i - |C_i|)C_i/2$ is equal to ${C_i}^2$. If the inequality constraint is not active, then this term is equal to zero.

The gradient of this cost function, which is required in the BFGS method described in Section A.3, is then:

$$\nabla_{\mathbf{\Theta}}\Pi = \nabla_{\mathbf{\Theta}}P + {\boldsymbol{\lambda}_c}^T \nabla_{\mathbf{\Theta}}\mathbf{C} + W_3 \sum_{i \in i_b}^{M} \frac{(C_i - |C_i|)\nabla_{\mathbf{\Theta}} C_i}{2} \tag{A.9}$$

where $\nabla_{\mathbf{\Theta}}\mathbf{C}$ is a matrix describing the change in chord at a given station due to a change in a given control variable. In other words, the elements of $\nabla_{\mathbf{\Theta}}\mathbf{C}$ are given by

$$\nabla_{\Theta} C_{ij} = \frac{\partial c_i}{\partial \Theta_j} \tag{A.10}$$

When using the value of the chord at discrete radial panels as elements in the design variable vector $\mathbf{\Theta}$, the matrix $\nabla_{\mathbf{\Theta}}\mathbf{C}$ is simply equal to the identity matrix, as any change in the i^{th} chord design variable will lead to the same change in chord at the i^{th} radial station and will not affect the chord at any other station. However, things are slightly more complex when representing the chord distribution using global shape functions. In this case, the matrix $\nabla_{\mathbf{\Theta}}\mathbf{C}$ is equal to $\mathbf{S}_{\text{cRadial}}$, the fully populated matrix that relates the control inputs (which in this case are coefficients to Chebyshev polynomials) to the value of the chord at each radial station. The i^{th} column of the $\nabla_{\mathbf{\Theta}}\mathbf{C}$ matrix is given by the vector $\nabla_{\mathbf{\Theta}}\mathbf{C}_i$.

Also note that $\nabla_{\mathbf{\Theta}}\Pi$ has an entry corresponding to every design variable, including angle inputs, and is therefore of length h. The vectors ${\boldsymbol{\lambda}_c}^T \nabla_{\mathbf{\Theta}}\mathbf{C}$ and $\nabla_{\mathbf{\Theta}}\mathbf{C}_i$ in Equation (A.9), however, only have entries for each *chord* design variable and are of length g, since no pitch angle design variable has an effect on the chord distribution.

These vectors must be padded with zeroes in the locations corresponding to pitch angle design variables when included in the overall cost function gradient given in Equation (A.2). Alternatively, similar constraints could be implemented to enforce maximum and minimum limits on the fixed twist or root pitch of the blade as well.

Using the method of Mathematical Programming wia Augmaented Lagrangians, the vector of Lagrange multipliers $\boldsymbol{\lambda}_c$ is updated after each unconstrained minimization using the following rules:

$$\text{for } \lambda_{i\text{old}} = 0, \;\; \lambda_{i\text{new}} = \begin{cases} W_3(C_i - |C_i|) & \text{if} < 0 \\ 0 & \text{otherwise} \end{cases} \tag{A.11}$$

$$\text{for } \lambda_{i\text{old}} < 0, \;\; \lambda_{i\text{new}} = \begin{cases} \lambda_{i\text{old}} + W_3 C_i & \text{if} < 0 \\ 0 & \text{otherwise} \end{cases} \tag{A.12}$$

Although the chord distribution may violate these inequality constraints throughout the optimization, a solution is not considered optimal until all inequality constraints are satisfied, per the Kuhn Tucker conditions.

As discussed in Section 3.4.6, it is also useful in some circumstances to constrain the thrust weighted solidity of the rotor, with the thrust weighted solidity defined in Equation (3.63). The constraint takes the form of the scalar inequality constraint shown below

$$\sigma_{\text{constraint}} = \sigma - \sigma_{\min} \geq 0 \tag{A.13}$$

where σ is the solidity of the rotor (based on whichever definition of solidity is used) and $\sigma_{\min}$ is the minimum required solidity. This constraint is then implemented in the same manner as the inequality constraint on chord. The gradient of the solidity, which relates the change in each chord variable to the resulting change in solidity, is calculated using an automatically differentiated subroutine. For more information on automatic differentiation, see Section A.6.

A.5 Step Size Control

At each step in the BFGS algorithm, a new search direction $\mathbf{d}_k$ is determined. The design variables vector must then take some step along this line, such that $\mathbf{\Theta}_{k+1} = \mathbf{\Theta}_k + c\mathbf{d}_k$. We wish to find some minimum, or near-minimum, along this search direction in the most computationally efficient manner. The Armijo step size rule, as documented in Reference [6], is an inexpensive method to determine c without performing an exact line search. First, we set $c = \bar{c}\gamma^m$, where γ is a positive number less than one. $\bar{c}$ must then satisfy the following condition:

$$\Pi(\mathbf{\Theta}_k) - \Pi(\mathbf{\Theta}_k + \bar{c}\mathbf{d}_k) < -\sigma\bar{c}\nabla\Pi(\mathbf{\Theta})^T\mathbf{d}_k$$
$$\bar{c} > 0 \tag{A.14}$$

The variable m is then the smallest nonnegative integer which satisfies the following inequality

$$\Pi(\mathbf{\Theta}_k) - \Pi(\mathbf{\Theta}_k + \bar{c}\gamma^m\mathbf{d}_k) \geq -\sigma\bar{c}\gamma^m\nabla\Pi(\mathbf{\Theta})^T\mathbf{d}_k \tag{A.15}$$

The parameters σ and γ can be varied based on the nature of the problem one is attempting to solve. Using the Armijo rule for step size control ensures that the step taken results in an improvement in the cost function, moving the search routine closer to the minimum with each successive iteration.

A.6 Calculating Gradients Using the Adjoint Method

Any gradient based optimization technique, including BFGS, requires either the gradient of the cost function or some approximation of this gradient. The gradient of a simplifed cost function is shown in Equation (A.2). This gradient is a vector $\nabla_{\mathbf{\Theta}}\Pi$ of size h that gives the direction of steepest increase for the cost function, with an entry corresponding to each design variable. Calculating this total gradient requires calculating multiple separate gradients: $\nabla_{\mathbf{\Theta}}P$, or the direction of the vector of design variables that leads to the steepest increase in power, $\nabla_{\mathbf{\Theta}}F$, the direction of

the vector of design variables that leads to the steepest increase of each element of force, and so on. The total cost function gradient is then a weighted sum of these gradients.

Calculating the individual gradients can be done in a variety of ways. If power loss, for example, was given by some analytical expression, it would be possible to differentiate this expression symbolically with respect to the design variables and obtain a closed form equation for the gradient of the power. However, power is directly dependent on the circulation distribution, which is in turn dependent on the lift curve slope, pitch angle, and chord value at each panel in the vortex lattice grid, making it difficult to find the gradient symbolically.

Another potential method is to approximate the gradients numerically. For example, for the gradient of power, $\nabla_{\mathbf{\Theta}} P$, each component of the gradient vector can be approximated using finite centered differences to determine the change in power output based on a small variation in one element of the design variable vector:

$$\frac{\partial P}{\partial \Theta_i} \approx \frac{P(\Theta + \epsilon\Theta_i) - P(\Theta - \epsilon\Theta_i)}{2\epsilon} \tag{A.16}$$

In the above notation, $P(\mathbf{\Theta})$ is the power resulting from the set of controls $\mathbf{\Theta}$, while $P(\mathbf{\Theta} + \epsilon\Theta_i)$ is the power resulting from the same set of controls $\mathbf{\Theta}$ with some small value ϵ added to the i^{th} entry of $\mathbf{\Theta}$. Approximating the entire gradient vector requires repeating this calculation for each entry of the design variable vector, which is computationally expensive. Additionally, truncation and roundoff error is introduced because of the requirement to use a small but finite ϵ.

A third option to calculate the gradients, and the one used in the code, is through adjoint automatic differentiation. The basic method behind automatic differentiation is to apply the chain rule repeatedly to each simple operation in a complicated algorithm, generating a code that can calculate any arbitrary derivative to working precision. Applying the chain rule to each computation in an algorithm results in

a product of matrices, with each matrix corresponding to a step in the algorithm. Evaluation of the derivative in the typical "forward" mode, working from the starting value of the modified variable to the final value, then requires performing repeated matrix-matrix multiplications. "Reverse" automatic differentiation is able to compute the gradient of a given variable very efficiently by starting with the final value of the modified variable and working through the operations in the reverse order. For a scalar output, this turns the series of matrix-matrix operations into a series of vector-matrix operations, resulting in a process that is computationally less expensive than forward differentiation when dealing with cases where the number of output variables is less than the number of input variables. When dealing with a scalar output, as is the case here, the reverse mode is particularly advantageous, and is referred to as the adjoint method [12].

The code to calculate the gradients was created using the adjoint compiler Tapenade [18]. The algorithm outlined in Section 3.3.2 for calculating the circulation distribution and resultant power, forces and moments was automatically differentiated in "reverse" mode, with the vector of design variables designated as the independent input variables and the power, forces and moments (all scalars) designated as dependent outputs. Because the original circulation calculation is an iterative technique, the adjoint differentiated code also uses an iterative technique, and also includes a damping factor. As a result, the number of iterations and level of damping can be changed to obtain varying levels of accuracy in the gradients.

A.7 Conclusion

A comparison of the method presented in this Appendix and the Newton iteration presented in Section 3.4 is made in Section 3.5. Mathematical Programming via Augmented Lagrangians is slower than the Newton iteration and requires more weighting terms to be defined by the user. However, it is still an effective way of solving the

optimization problem, and has been presented here for completeness.

Bibliography

[1] Allen, C. B. (2004), "An Unsteady Multiblock Multigrid Scheme for Lifting Forward Flight Rotor Simulation," *International Journal for Numerical Methods in Fluids*, 45, 973–984.

[2] Anderson, J. D. (2001), *Fundamentals of Aerodynamics*, vol. 2, McGraw-Hill New York.

[3] Anderson, J. D., Corda, S., and Van Wie, D. (1980), "Numerical Lifting Line Theory Applied to Drooped Leading-Edge Wings Below and Above Stall," *Journal of Aircraft*, 17, 898–904.

[4] Arcidiacono, P. J. (1961), "Theoretical Performance of Helicopters Having Second and Higher Harmonic Feathering Control," *Journal of the American Helicopter Society*, 6, 8–19.

[5] Bagai, A. (2008), "Aerodynamic Design of the X2 Technology Demonstrator Main Rotor Blade," in *American Helicopter Society 64th Annual Forum Proceedings*, Montreal, Canada.

[6] Bertsekas, D. P. (1996), *Constrained Optimization and Lagrange Multiplier Methods*, Athena Scientific.

[7] Betz, A. (1919), "Schraubenpropeller mit geringstem Energieverlust. Mit einem Zusatz von l. Prandtl," *Nachrichten von der Gesellschaft der Wissenschaften zu Göttingen, Mathematisch-Physikalische Klasse*, 1919, 193–217.

[8] Broyden, C. G. (1970), "The Convergence of a Class of Double-Rank Minimization Algorithms," *IMA Journal of Applied Mathematics*, 6, 76–90.

[9] Caradonna, F. X. and Tung, C. (1981), "Experimental and Analytical Studies of a Model Helicopter Rotor in Hover," *Vertica*, 5, 149–161.

[10] Cheng, R., Theodore, T. R., and Celi, R. (2000), "Effects of Higher Harmonic Control on Rotor Performance," in *American Helicopter Society 56th Annual Forum*, Virginia Beach, Virginia.

[11] Croft, J. (2010), "Sikorsky X2 Hits 250 kt goal." http://www.flightglobal.com/news/articles/sikorsky-x2-hits-250kt-goal-347379/.

[12] Giering, R. and Kaminski, T. (1998), "Recipes for Adjoint Code Construction," *ACM Transactions on Mathematical Software*, 24, 437–474.

[13] Goldstein, S. (1929), "On the Vortex Theory of Screw Propellers," *Proceedings of the Royal Society of London. Series A*, 123, 440–465.

[14] Hall, K. and Hall, S. (2010), "A Variational Method for Computing the Optimal Aerodynamic Performance of Conventional and Compound Helicopters," *Journal of the American Helicopter Society*, 55, 42006 – 1.

[15] Hall, K. C. (1983), "Optimal Mistuning for Enhanced Aeroelastic Stability of Transonic Fans," Master's thesis, Massachusetts Institute of Technology.

[16] Hall, K. C. and Giovanetti, E. B. (2013), "Minimum Power Requirements and Optimal Rotor Design for Conventional and Compound Helicopters Using Higher Harmonic Control," in *American Helicopter Society's 69th Annual Forum*, Phoenix, Arizona.

[17] Hall, S. R., Yang, K. Y., and Hall, K. C. (1994), "Helicopter Rotor Lift Distributions for Minimum-Induced Power Loss," *Journal of Aircraft*, 31, 837 – 845.

[18] Hascoet, L. and Pascual, V. (2004), *Tapenade 2.1 User's Guide*, Project Tropics, INRIA Sophia-Antipolis.

[19] Jacklin, S. A., Nguyen, K., Blass, A., and Richter, P. (1994), "Full-Scale Wind Tunnel Test of a Helicopter Individual Blade Control System," in *American Helicopter Society 50th Annual Forum*, Washington, D.C.

[20] Jacklin, S. A., Blass, A., Swanson, S. M., and Teves, D. (1995), "Second Test of a Helicopter Individual Blade Control System in the NASA Ames 40- by 80-foot Wind Tunnel," in *Proceedings of the American Helicopter Society 2nd International Aeromechanics Specialists' Conference*, Bridgeport, Connecticut.

[21] Johnson, W. (2008), "Influence of Lift Offset on Rotorcraft Performance," in *American Helicopter Society Specialist's Conference on Aeromechanics*, San Francisco, California.

[22] Johnson, W., Moodie, A. M., and Yeo, H. (2012), "Design and Performance of Lift-Offset Rotorcraft for Short-Haul Missions," Tech. rep., DTIC Document.

[23] Kuhn, H. and Tucker, A. (1951), "Nonlinear Programming," in *Proceedings of 2nd Berkeley Symposium*.

[24] Landis, T. and Jenkins, D. (2000), *Lockheed AH-56A Cheyenne - Warbird Tech Vol. 27*, Specialty Press.

[25] Moffitt, R. and Bissell, J. (1982), "Theory and Application of Optimum Airloads to Rotors in Hover and Forward Flight," in *American Helicopter Society 38th Annual Forum Proceedings*, Anaheim, CA.

[26] Moffitt, R. and Rivera, S. (1993), "An Implicit Multi-Point Lifting Line Optimizer for Twist and Chord," in *American Helicopter Society International Technical Specialists' Meeting on Rotorcraft Multidisciplinary Design Optimization*, Atlanta, GA.

[27] Ormiston, R. (2004), "Induced Power of the Helicopter Rotor," in *American Helicoper Society 60th Annual Forum and Technology Display*, Baltimore, MD.

[28] Ormiston, R. (2005), "Further Investigations of Helicopter Rotor Induced Power," in *American Helicopter Society 61st Annual Forum Proceedings*, Grapevine, TX.

[29] Ormiston, R. (2009), "An Analytical Formulation for Lifting Rotor Induced Power," in *AHS International 65th Annual Forum and Technology Display*, Grapevine, TX.

[30] Ormiston, R. (2013), "On the Definitions of Rotor and Rotorcraft Power and Performance," in *AHS International 69th Annual Forum and Technology Display*, Phoenix, AZ.

[31] Ormiston, R. A. (2010), "Applications of the Induced Power Model and Performance of Conventional and Advanced Rotorcraft," in *American Helicopter Society Aeromechanics Specialists' Conference*, San Francisco, CA.

[32] Paur, J. (2013), "X3 Helicopter Sets Speed Record at Nearly 300 MPH." Internet article: http://www.wired.com/autopia/2013/06/eurocopter-x3-speed-record/.

[33] Payne, P. (1958), "Higher Harmonic Rotor Control: the Possibilities of Third and Higher Harmonic Feathering for Delaying the Stall Limit in Helicopters," *Aircraft Engineering and Aerospace Technology*, 30, 222–226.

[34] Quick, D. (2010a), "Eurocopter's X3 hybrid helicopter demonstrator reaches 180 knot milestone." Internet article: http://www.gizmag.com/eurocopter-x3-hybrid-helicopter-demonstrator/17253/.

[35] Quick, D. (2010b), "Sikorsky's X2 demonstrator sets unofficial world record speed of 250 knots." Internet article: http://www.gizmag.com/sikorsky-x2-demonstrator-250-knot-milestone/16424/.

[36] Rand, O., Khromov, V., and Peyran, R. J. (2004), "Minimum-Induced Power loss of a Helicopter Rotor via Circulation Optimization," *Journal of Aircraft*, 41, 104–109.

[37] Russell, C. and Johnson, W. (2013), "Exploration of Configuration Options for a Large Civil Compound Helicopter," in *American Helicopter Society 69th Annual Forum*, Phoenix, Arizona.

[38] Shaw, J., Albion, N., Hanker, E. J., and Teal, R. S. (1989), "Higher Harmonic Control: Wind Tunnel Demonstration of Fully Effective Vibratory Hub Force Suppression," *Journal of the American Helicopter Society*, 34, 14–25.

[39] Sheldahl, R. and Klimas, P. (1981), "Aerodynamic Characteristics of Seven Symmetrical Airfoil Sections Through 180-degree Angle of Attack for Use in Aerodynamic Analysis of Vertical Axis Wind Turbines," Tech. rep., Sandia National Labs., Albuquerque, NM (USA).

[40] Stewart, W. (1952), "Second Harmonic Control on the Helicopter Rotor," *Aeronautical Research Council R & M*, 2997.

[41] Wachspress, D. A., Quackenbush, T. R., and Solomon, C. L. (2005), "On Minimum Induced Power of the Helicopter Rotor," in *American Helicopter Society's 61st Annual Forum*, Grapevine, Texas.

[42] Yang, K. Y. (1993), "Helicopter Rotor Lift Distributions for Minimum Induced Power Loss," Master's thesis, Massachusetts Institute of Technology.